A mathematical study on coupled multiple timescale systems, synchronization of populations of endocrine neurons

Elif Köksal Ersöz

To cite this version:

Elif Köksal Ersöz. A mathematical study on coupled multiple timescale systems, synchronization of populations of endocrine neurons. Modeling and Simulation. Université Pierre et Marie Curie - Paris VI, 2016. English. NNT : 2016PA066516 . tel-01522725

HAL Id: tel-01522725
https://theses.hal.science/tel-01522725

Submitted on 15 May 2017

A mathematical study on coupled multiple timescale systems, synchronization of populations of endocrine neurons

THÈSE DE DOCTORAT

présentée par

Elif KÖKSAL ERSÖZ

pour obtenir le grade de

DOCTEUR DE L'UNIVERSITÉ PIERRE ET MARIE CURIE

Spécialité

Mathématiques Appliquées

réalisée

À Centre de Recherche de Inria de Paris - Équipe projet MYCENAE

sous la direction de Frédérique CLÉMENT et Jean-Pierre FRANÇOISE

A mathematical study on coupled multiple timescale systems, synchronization of populations of endocrine neurons

Abstract

This dissertation investigates synchronization properties of slow-fast oscillators inspired from neuroendocrinology and neuronal dynamics, focusing on the effects of canard phenomena and dynamic bifurcations on the collective behavior.

We start from a 4-dimensional system which accounts for the qualitative and quantitative dynamical features of the secretion pattern of the neurohormone GnRH (gonadotropin releasing hormone) along a whole ovarian cycle. This model involves 2 FitzHugh-Nagumo oscillators with different timescales. Unidirectional coupling from the slow oscillator (representing the mean-field activity of a population of regulating neurons) to the fast oscillator (representing the mean-field activity of a population of the secreting neurons) gives a three timescale structure. The behavior of the fast oscillator is characterized by an alternation between a relaxation cycle and a quasi-stationary state which introduces canard-mediated transitions in the model; these transitions have a strong impact on the secretion pattern of the 4-dimensional system. We make a first step forward in multiscale modeling (in space) of the GnRH system, namely, we extend the original system to 6 dimensions by considering two distinct subpopulations of secreting neurons receiving the same signal from the regulating neurons. This step allows us to enrich further the GnRH secretion pattern while keeping a compact dynamic framework and preserving the sequence of neurosecretory events captured by the 4-dimensional model, both qualitatively and quantitatively.

An initial analysis of the extended 6-dimensional GnRH model is presented in Chapter 2, where we prove using a 5D minimal model the existence of canard trajectories in coupled systems with folded singularities. Coupling causes separation of trajectories corresponding to each secretor by driving them to different sides of the maximal canard (associated with either a folded-node or a folded-saddle singularity). We explore the impact of the relationship between canard structures and coupling on the collective secretion pattern of the 6-dimensional model. We identify two different sources of canard-mediated (de)synchronization in the secretory events, which depend on the type of underlying folded singularity.

In Chapter 3, we attempt to model complex behaviors of the GnRH secretion not captured by the 4-dimensional model, namely, a surge with 2 bumps and partial desynchronization before the surge, by using the 6-dimensional model previously constructed. Regulatory-dependent asymmetric coupling functions and heterogeneity in the secretor subpopulations are essential for obtaining such a 2-bump surge. During the pulsatile regime, we find that the slowly varying regulatory signal causes a dynamic bifurcation, which is responsible for loss of synchrony in asymmetrically coupled non-identical secretors. We introduce analytic and numerical tools to shape and quantify the additional features embedded within the whole secretion pattern.

In order to get further understanding on the role of canards in (de)synchronization phenomena, in Chapter 4, we extend the theory of weakly coupled (planar) oscillators to the case of canard cycles. We find solutions of adjoint equations of singularly perturbed oscillators by using numerical continuation techniques. We identify the role of the maximal canard as a pivotal in the transition between different modes of synchronization. We find $2nT$-periodic synchronous solutions arising in coupled identical cycles near the maximal canard depending on the coupling strength and on the main canard parameter.

The dynamic bifurcations and slow-fast transitions studied in this dissertation have applications to spiking/bursting systems in neuroscience, and ideas for the extension of our work to these dynamics are highlighted in the Conclusion chapter.

Keywords canards, synchronization, slow-fast systems, multiple timescales, folded singularity, GnRH secretion, weakly coupled oscillators, dynamic bifurcation

Étude mathématique de systèmes multi-échelles en temps couplés, synchronisation de populations de neurones endocrines

Résumé

Dans cette thèse, nous étudions les propriétés de synchronisation d'oscillateurs lents-rapides inspirés de la neuroendocrinologie et des neurosciences, en se concentrant sur les effets des phénomènes de type canard et bifurcations dynamiques sur le comportement collectif.

Nous partons d'un système de dimension 4 qui représente les caractéristiques dynamiques qualitatives et quantitatives du profil de sécrétion de la neurohormone GnRH (gonadotropin releasing hormone) au cours d'un cycle ovarien. Ce modèle est constitué de deux oscillateurs de FitzHugh-Nagumo avec pour chacun des échelles de temps différentes. Le couplage unidirectionnel de l'oscillateur lent (représentant l'activité moyenne d'une population de neurones régulateurs) vers l'oscillateur rapide (représentant l'activité moyenne d'une population de neurones sécréteurs) donne une structure à trois échelles de temps. Le comportement de l'oscillateur rapide est characterisé par une alternance entre un régime de type cycle de relaxation et un régime de quasi-stationnaire qui induit des transitions de type canard dans le modèle ; ces transitions ont un fort impact sur le modèle de sécrétion du système de dimension 4. Nous proposons un premier pas supplémentaire dans la modélisation multi-échelles (en espace) du système GnRH, c'est-à-dire que nous étendons le système original à 6 dimensions en considérant deux sous-populations distinctes de neurones sécréteurs recevant le même signal des neurones de régulation. Cette étape nous permet de enrichir les motifs possibles de sécrétion de GnRH tout en gardant un cadre dynamique compact et en préservant la séquence des événements neuro-sécréteurs capturés par le modèle de dimension 4, à la fois qualitativement et quantitativement.

Une première analyse du modèle GnRH étendu à 6 dimensions est présentée dans le Chapitre 2, où nous montrons à l'aide d'un système minimal de dimension 5 l'existence de trajectoires de type canard dans des systèmes lents-rapides couplés présentant des points pseudo-stationnaires. Le couplage provoque la séparation des trajectoires correspondant à chaque sécréteur qui se retrouvent de chaque côté du canard maximal (associé soit à un point pseudo-stationnaire de type noeud soit à un pseudo-col). Nous explorons les rapports entre les canards en présence et le couplage, ainsi que leur impact sur les motifs de sécrétion collective du modèle de dimension 6. Nous identifions deux sources différentes de (dé)synchronisation due aux canards dans les événements sécrétoires, qui dépendent du type de point pseudo-stationnaire sous-jacent.

Dans le Chapitre 3, nous proposons une modélisation possible des comportements complexes de sécrétion de GnRH qui ne sont pas capturés par le modèle de dimension 4, à savoir, une décharge avec 2 “bosses” et une désynchronisation partielle avant la décharge, en utilisant le modèle de dimension 6 précédemment construit. Pour obtenir une décharge avec deux bosses, il est essentiel d'utiliser des fonctions de couplage asymétriques dépendant du régulateur ainsi que d'introduire de l'hétérogénéité dans les sous-populations de sécréteurs. Pendant le régime pulsatile, il apparaît que le signal régulateur varie lentement et, ce faisant, provoque une bifurcation dynamique qui est responsable de la perte de synchronie dans le cas de sécréteurs non identiques et asymétriquement couplés. Nous introduisons des outils analytiques et numériques pour façonner et quantifier ces caractéristiques supplémentaires et les intégrer dans le profil complet de sécrétion.

Afin d'obtenir une meilleure compréhension du rôle des canards dans les phénomènes de (dé)synchronisation, nous proposons, au Chapitre 4, une extension de la théorie de oscillateurs (du plan) faiblement couplés au cas des cycles de canard. À l'aide de techniques de continuation numérique, nous calculons des solutions aux problèmes adjoints associés à des oscillateurs singulièrement perturbés. Nous identifions le rôle pivot que joue le canard maximal dans la transition entre les différents modes de synchronisation. Nous trouvons des solutions synchrones $2nT$-périodiques pour des systèmes identiques couplés à proximité du canard maximal et nous étudions l'impact de la force de couplage et du principal paramètre qui organise l'explosion de canards (pour chaque oscillateur seul) sur l'existence de telles familles de solutions synchrones.

Les bifurcations dynamiques et transitions lentes-rapides étudiées dans cette thèse se retrouvent plus généralement en neuroscience, dans les systèmes produisant des dynamiques de type “spiking” et/ou “bursting”. Un certain nombre de pistes concernant l'extension de notre travail à ces dynamiques sont mises en évidence dans le chapitre de conclusion.

Mots-clés canards, synchronisation, systèmes lents-rapides, systèmes multi-échelles de temps, points pseudo-stationnaires, sécrétion de GnRH, oscillateurs faiblement couplés, bifurcations dynamiques

Aydum'a

Acknowledgments

First and foremost, I would like to thank my supervisors Fédérique Clément and Jean-Pierre Françoise for giving me this opportunity to work with their impressing model during three years.

I thank Fédérique Clément for sharing her extraordinary modeling view point which gives a great freedom and motivation to go beyond the classical approaches. I own a lot to her endless patience to my mistakes and her encouragement to face with challenging problems. Her support and constructive criticism have been particularly appreciated throughout.

I thank Jean-Pierre Françoise for his curiosity and delightful contribution which lightened this study. I thank Alexandre Vidal for his innovative ideas and tolerance during our “camel surge” journey.

I would like to express my sincere gratitude to Mathieu Desroches and Martin Krupa for following me closely in the years of my Ph.D studies, and for inspiring me to do my best every day during the *chasse au canard*. It has been a great honor for me to work with Martin Krupa who has been our modest guru over three years valorizing this study and expanding it to the most exciting directions.

I appreciate a lot Mathieu's personal patience and genuine humanity initiated the global dissipation essential to clear scientific and personal doubts, giving me self-confidence and optimism, especially when I needed them the most. Without his support, I would neither be able to complete this study nor continue in research.

I want to thank my reading committee members Prof. Antoni Guillamon and Prof. Jonathan Rubin for the time spent to carefully read my dissertation and for their stimulating comments. Also, I would like to extend my gratitude to the other members of my defense committee for their availability to attend my Ph.D. defense and for their keen interest in my work. I am honored to have you all in my Ph.D. thesis commission.

My salutations to the ex-members of MYCENAE Albert Granados, Soledad Fernandez-Garcia and her husband, Jaume, the new member of MYCENAE Frédérique Robin, as well as Marie Postel, our secretaries Martine Verneuille and Martine Girardot, all members of SMIS.

Perhaps most importantly, I thank my husband Aydoğan, my strongest supporter throughout this endeavor by shining my life everyday. I also appreciate the support and encouragement received from our respective parents, my brother Alican, Armağan and as well as from friends.

Contents

Chapter 1

Introduction

This dissertation investigates the dynamics of coupled slow-fast systems in which canard structures and slowly varying variables determine the global outputs with applications in neuroendocrinology and neuroscience. Motivation for neuroendocrinology comes from the oscillations of the Gonadotropin Releasing Hormone (GnRH), a hormone secreted from hypothalamus to pituitary portal blood and has an overwhelming role in reproductive biology. Motivation for neuroscience aspects of this work comes from the characteristics of the oscillations, which are classified as type-II neurons, one being the appearance of the oscillations through a singular Hopf bifurcation.

1.1 A model for the dynamics of the gonadotropin releasing hormone secretion

The reproductive axis, usually called the gonadotrope axis, involves the hypothalamus, within the central nervous system, the pituitary gland, and the gonads (ovaries in females and testes in males). GnRH is secreted by hypothalamic endocrine neurons into the pituitary portal blood in a pulsatile manner. This pulsatility has a fundamental role in the secretion of luteinizing hormone (LH) and follicle stimulating hormone (FSH) by the pituitary gland. In females the pulsatile pattern is altered once over ovarian cycle, when a massive release of GnRH, so-called *surge*, occurs. The steroid signals emanating from the ovaries are conveyed by regulatory interneurons onto the GnRH neural network; they control both the alternation between the pulsatile and surge pattern and the frequency and amplitude of the GnRH pulses.

A mathematical model accounting for the secretion pattern of GnRH along a whole ovarian cycle proposed in [1]. This model consists of 2 coupled FitzHugh-Nagumo (FHN) oscillators with different timescales, corresponding respectively to a population of regulatory interneurons and a population of secreting neurons. The populations are defined on the macroscopic level where their activities are represented by a mean-field approximation. The 4-dimensional (4D) model reads:

$$
\begin{aligned}
\varepsilon\delta\dot{x} &= -y + f(x), \\
\delta\dot{y} &= a_0 x + a_1 y + a_2 + cX, \\
\delta\dot{X} &= -Y + g(X), \\
\dot{Y} &= X + b_1 Y + b_2
\end{aligned}
\tag{1.1.1}
$$

where

$$
\begin{aligned}
&f(x) = \lambda_3 x^3 + \lambda_1 x, \\
&g(X) = \mu_3 X^3 + \mu_1 X, \\
&\lambda_3, \mu_3 < 0, \quad \lambda_1, \mu_1 > 0, \\
&a_i, c > 0, \quad 0 < \varepsilon \ll 1, \quad 0 < \delta \ll 1.
\end{aligned}
$$

The slow system (X, Y) represents the population of regulating neurons (regulator), the fast system (x, y) represents the secreting population (secretor), and the solution component $y(t)$, which corresponds to GnRH secretion along time, can be referred as the output of the system (1.1.1). The unidirectional coupling between the systems via the term cX leads to a three-timescale model, which is able to capture the periodic back and forth transition from the pulsatile regime (corresponding to a relaxation limit cycle in the secretor) to the surge (corresponding to a quasi-stationary equilibrium in the secretor), as well as the increase in the pulse frequency all along the pulsatile regime.

Figure 1.1 shows the dynamics organized according the 4 phases in the (X, Y) relaxation cycle. The slow motions along the left and right branches of the $Y = g(X)$ curve correspond to the pulsatile regime (phase-1) and surge regime (phase-3), respectively. The rightward (phase-2) and leftward (phase-4) fast motions organize transitions between pulsatile and surge regimes whose durations depend on the length of the slow motions of the (X, Y) relaxation cycle. The frequency of the relaxation limit cycle in the (x, y) plane is regulated via the X variable and ensured to be increasing along the pulsatile regime. Besides, the variable X controls the ascending and descending motion during the surge and determines the surge amplitude by changing the position of a quasi-stationary point located along the left branch of the $y = f(x)$ curve.

From the point of view of dynamical classification, (1.1.1) is a phantom burster. The bursting mechanism is organized by the alternation between the existence of a (quasi-static) singular point and a limit cycle of the forced oscillator (secretor) led by a forcing oscillator (regulator) [2]. System (1.1.1) was analyzed in [3, 4] where authors provided constraints on the parameters ensuring the sequential behavior of the secretor and a detailed description of parameter tuning method with respect to biological specification (e.g. the ratio between the amplitude of the surge and the amplitude of the pulses, the frequency of the pulses and its evolution along the pulsatile regime). The global and local features of the model have been studied in the context of the slow-fast dynamics and mixed-mode oscillations (MMOs) that arise due to a *generalized canard phenomena* in [5] (Figure 1.2).

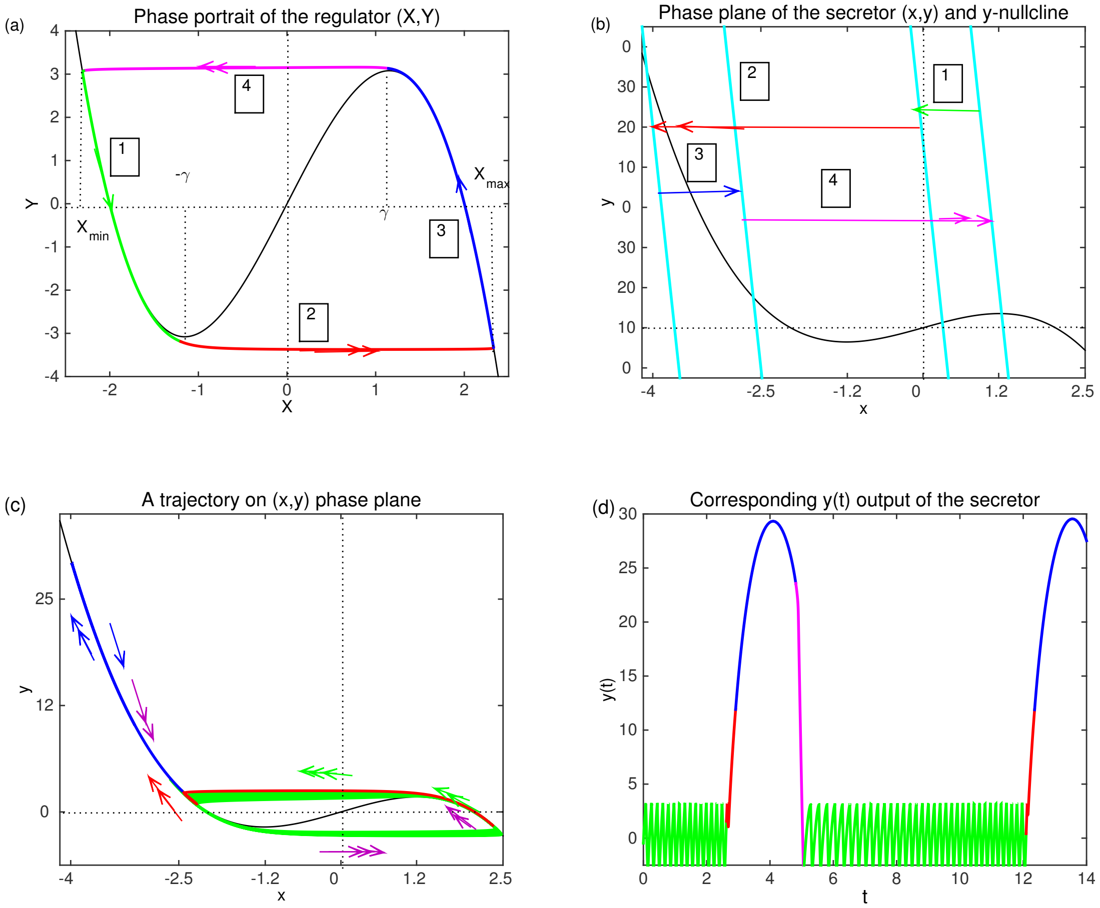

Figure 1.1: (a) Attracting relaxation cycle in the (X, Y) phase plane. Each number represents a different dynamic phase of the periodic behavior of the secretor. 2-headed arrows indicate an $O(\delta)$ speed, 1-headed arrows indicted an $O(1)$ speed. (b) Position of the nullclines on the (x, y) plane with respect to the dynamic phases in the (X, Y) relaxation cycle. Green arrow: pulsatile phase. Red arrow: transition from pulsatility to surge. Blue arrow: surge phase. Pink arrow: transition from surge to pulsatility (c) Projection of a typical trajectory onto (x,y) plane. Colors represent phases and 3-headed arrows indicate an $O(\varepsilon\delta)$ speed (d) Traces in time of the output variable $y(t)$ colored according the dynamic phases.

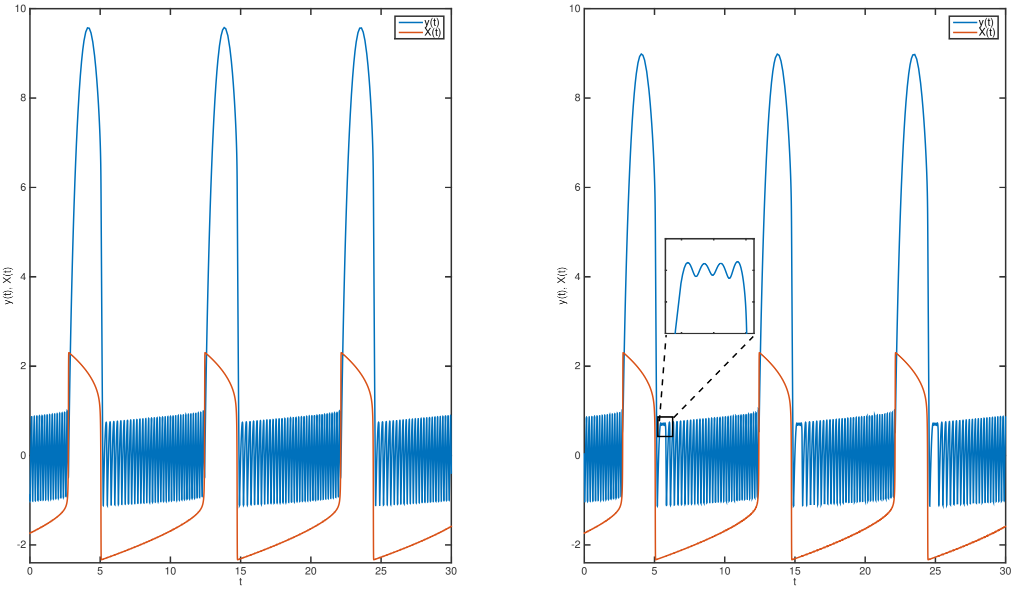

Figure 1.2: Left panel: Traces in time of the regulator signal X(t) (red) and output variable $y(t)$. Right panel: Traces in time of the regulator signal X(t) (red) and output variable $y(t)$ involving a “pause” with small amplitude oscillations (inner panel).

1.2 Slow-fast dynamical systems and canard phenomena

Canard solutions were discovered in van der Pol (VDP) relaxation oscillator under constant forcing [6]. The term *canard* refers to a class of solutions in slow-fast systems that follows the unstable branch of the critical manifold during a considerable time interval. In the $\mathbb{R}^2$ vector field of VDP, the *canard phenomenon* explains the transition from small limit cycles to large relaxation cycles, upon variations of a system parameter in the order of the timescale separation parameter [7]. The sharp transition is called a *canard explosion* [8]. Canard solutions in planar systems have been studied by nonstandard techniques [6, 9], asymptotic expansion techniques [10] and geometric singular perturbation theory [11, 12].

Combinations of advanced theoretical tools, such as blow-up methods [13], and numerical methods [14] generalized the canard phenomena in $\mathbb{R}^2$ to higher dimensions ($\mathbb{R}^n$, $n \geq 3$). The generalized canard phenomenon has introduced a new understanding of complex oscillatory systems such as MMOs [15], bursting dynamics [16, 17] with applications to neuroscience [18, 19, 20, 21, 22, 23], chemistry [24, 25, 26, 27], and calcium signaling [28, 17]. Here we recall the canard phenomenon in slow-fast dynamical systems.

A slow-fast vector field takes the form

$$\begin{aligned} \varepsilon\frac{dx}{d\tau} &= f(x, y, \lambda, \varepsilon), \\ \frac{dy}{d\tau} &= g(x, y, \lambda, \varepsilon) \end{aligned} \tag{1.2.1}$$

where $(x, y) \in \mathbb{R}^m \times \mathbb{R}^n$ are state-space variables, $\lambda \in \mathbb{R}^p$ are system parameters and ε is a small parameter $0 < \varepsilon \ll 1$ representing the ratio of time scales. $f : \mathbb{R}^m \times \mathbb{R}^n \times \mathbb{R}^p \times \mathbb{R} \to \mathbb{R}^m$ and $g : \mathbb{R}^m \times \mathbb{R}^n \times \mathbb{R}^p \times \mathbb{R} \to \mathbb{R}^n$ are smooth C^∞ functions. System (1.2.1) can be rescaled to

$$\begin{aligned} \frac{dx}{dt} &= f(x, y, \lambda, \varepsilon), \\ \frac{dy}{dt} &= \varepsilon g(x, y, \lambda, \varepsilon) \end{aligned} \tag{1.2.2}$$

by switching from slow time scale τ to fast time scale $t = \tau/\varepsilon$. Solutions of slow-fast systems generally consist of slow and fast epochs, i.e. long periods of slow change interspersed by short periods of fast change. As $\varepsilon \to 0$, trajectories of (1.2.2) approach the solutions of *fast subsystem* or *layer equations*

$$\begin{aligned} x' &= f(x, y, \lambda, 0), \\ y' &= 0. \end{aligned} \tag{1.2.3}$$

During slow epochs, trajectories of (1.2.1) converge to solutions of *slow subsystem* or *reduced system*

$$\begin{aligned} 0 &= f(x, y, \lambda, 0), \\ \dot{y} &= g(x, y, \lambda, 0) \end{aligned} \tag{1.2.4}$$

which is a differential-algebraic equation. The algebraic equation in (1.2.4) defines the *critical manifold*

$$C := \{(x, y) \in \mathbb{R}^m \times \mathbb{R}^n | f(x, y, \lambda, 0) = 0\} \tag{1.2.5}$$

which is the phase space of the reduced problem (1.2.4) and set of equilibrium points of the layer problem (1.2.3). One major goal of geometric singular perturbation theory is to use these lower dimensional subsystems, (1.2.3) and (1.2.4), to understand the dynamics of the full system (1.2.1) for $0 < \varepsilon \ll 1$.

Basic classification of singularly perturbed systems is given by the properties of the layer problem (1.2.3). A compact sub-manifold $C_h \subset C$ is *normally hyperbolic* if all $(x, y) \in C_h$ are hyperbolic equilibria of the layer problem, that is, the Jacobian $(D_y f)(x, y, 0)$ has no eigenvalues with zero real part. In that case, Fenichel theory [29] guarantees the existence of a perturbed locally invariant manifold C_ε called (Fenichel) slow manifold the original system $0 < \varepsilon \ll 1$. Fenichel slow manifolds are typically non-unique but they are exponentially close to each other (away from their boundary). They inherit the regularity of the vector filed, they are $O(\varepsilon)$-close to the unperturbed manifold C_h (for the Hausdorff distance) and the flow on them converges to the slow flow as $\varepsilon \to 0$. If the unperturbed manifold C_h belongs to an attracting (resp. a repelling) sheet of C – the real part of the eigenvalues of the Jacobian $(D_y f)(x, y, 0)$ being strictly negative (resp. strictly positive) — then the corresponding slow manifolds are called *attracting (resp. repelling) slow manifolds.* If C_h is normally hyperbolic and neither attracting nor repelling, it is of saddle type, and so are the corresponding slow manifolds.

A bifurcation of the fast subsystem is typically called *dynamic bifurcation* from the viewpoint of the full system [30]. Such a bifurcation in the fast subsystem may or may not induce a delayed transition in the full system accompanied with canard segments; if it does, then one uses the term *delayed bifurcation.* It can be a bifurcation of equilibria, in which case the bifurcation point corresponds to a change of attractivity of the critical manifold. It can also be a bifurcation of limit cycles and have an influence on the fast oscillatory dynamics of the full systems (as is the case for bursters).

Hyperbolicity of the layer problem is lost via a saddle-node bifurcation at the folds p_* $(f'(p_*, \lambda, 0) = 0)$ of C_ε. Canards are a special class of solutions of singularly perturbed systems where normal hyperbolicity is lost. A canard solution flows from an attracting slow manifold C_h^a to a repelling slow manifold C_h^r by passing close to a bifurcation point p_* of the critical manifold, a so-called *canard point.* A widely used tool to analyze the geometry of the fold regions and corresponding canard solutions is the *desingularized reduced system* (DRS). The critical manifold given in (1.2.5) approximates (to zeroth order in ε) the region of the phase space where the slow dynamics take place. The flow of the reduced system (1.2.4) can be analyzed by differentiating the equation of C with respect to time, giving

$$\begin{aligned} x' &= \pm(D_x f)^{-1}(D_y f)g, \\ y' &= g \end{aligned}$$

which is singular along the folds of C_ε. It can be *desingularized* by scaling time by $\pm\det(D_x f)$ keeping the direction of the flows

$$\begin{aligned} x' &= adj(D_x f)(D_y f)g, \\ y' &= \pm\det(D_x f)g. \end{aligned} \tag{1.2.6}$$

Canard solutions can appear due to the existence of the equilibria of the DRS (1.2.6), such that $\det(D_x f) = 0$, and they are referred as *folded singularities* (See Section 1.2.2).

In the next subsection we will explain the general process of desingularization in the VDP system and focus on the canard solutions in the VDP system.

1.2.1 Canards in the van der Pol system

The van der Pol equation with constant forcing $\lambda \in \mathbb{R}$ is given by

$$\begin{aligned} \varepsilon\dot{x} &= y - \frac{1}{3}x^3 + x, \\ \dot{y} &= \lambda - x. \end{aligned} \tag{1.2.7}$$

By setting $\varepsilon = 0$ in (1.2.7), we obtain the reduced system

$$\begin{aligned} 0 &= y - \frac{1}{3}x^3 + x, \\ \dot{y} &= \lambda - x. \end{aligned}$$

with an algebraic equation that defines the critical manifold of (1.2.7) as the cubic curve

$$C = \{(x, y) \in \mathbb{R}^2 | y = \frac{1}{3}x^3 - x =: c(x)\} \tag{1.2.8}$$

The curve C is normally hyperbolic away from the extrema $p_\pm = (\pm 1, \pm\frac{2}{3})$, which are the folds of C. The fold points divide the critical manifold into 3 branches,

$$C = C^{a,-} \cup \{p_-\} \cup C^r \cup \{p_+\} \cup C^{a,+}\},$$

where $C^{a,-} := C \cap \{x < -1\}$, $C^{a,+} := C \cap \{x > 1\}$ and $C^r := C \cap \{-1 < x < 1\}$. From the sign of $\frac{\partial}{\partial x} f(x, y, \lambda, 0)$, we conclude that $C^{a,-}$ and $C^{a,+}$ are the attracting branches, and C^r is the repelling branch. The normal hyperbolicity is lost at the fold points $p_\pm$ since $\frac{\partial}{\partial x} f(x, y, \lambda, 0) = -x^2 + 1$ is zero at $p_\pm$.

To obtain the slow flow of (1.2.7), we differentiate the equation of the critical manifold (1.2.8) with respect to time

$$\dot{y} = \dot{x}(x^2 - 1)$$

and combine with the equation for $\dot{y}$, which gives

$$\dot{x} = \frac{\lambda - x}{x^2 - 1}.$$

which is the equation for the slow flow. The slow flow is well defined on the attracting and repelling branches of C but not at the fold points $x = \pm 1$ (as long as $\lambda \neq \pm 1$) where the normal hyperbolicity is lost. We can desingularize the slow flow by rescaling time with the factor $(x^2 - 1)$ and obtain the equation for the *desingularized reduced flow* as $\dot{x} = \lambda - x$. The equilibrium $x = \lambda$ is stable for all values of λ. However the true slow flow is obtained via the time rescaling, which reverses the direction of the flow when $(x^2 - 1) < 0$, along the repelling branch of C. Therefore, the equilibrium of the DRS is unstable for the slow flow when $|\lambda| < 1$. The fold points C are jump points for $\lambda \neq \pm 1$ and canard points for $\lambda = \pm 1$ (only one of the two each time, the one that is also an equilibrium).

At $\lambda = \lambda_H = \pm 1$, the VDP system (1.2.7) undergoes a supercritical Hopf bifurcation and when $|\lambda| < 1$, the only equilibrium point lying on C^r is surrounded by an attracting limit cycle which is a relaxation cycle for most values of λ and for $0 < \varepsilon \ll 1$. The relaxation cycles are periodic solutions formed by the alternation between slow segments (well approximated by the slow flow) and fast segments (well approximated by the layer problem).

On the other hand at $\lambda_H = 1$, the desingularized reduced flow continuously goes from the attracting side of C to the repelling side. Near the Hopf bifurcation value λ_H, small stable cycles exist and they are very similar to those found in a normal form system. However, as λ decreases, at a distance of $O(\varepsilon)$ from λ_H, the canard explosion occurs. The periodic orbits grow rapidly and a family of limit cycle solutions, namely *canards without head* (also called *headless canards*), appears. The maximal headless canard, so-called *maximal canard*, exists at a unique parameter value $\lambda_c = \lambda_H - (1/8)\varepsilon - (3/32)\varepsilon^2 + O(\varepsilon^3)$ and it has the longest period among the canard families. The maximal canard is the solution which contains the longest repelling segment, that is, it stays close to the repelling branch of C all the way up to the other fold point at $x = -1$ as $\varepsilon \to 0$, before jumping to the right attracting branch of C. For the values $\lambda < \lambda_c$, the canard cycles jump from the repelling branch to the left attracting branch of C before jumping back to the right attracting branch. These canard cycles are referred as *canards with a head.* Finally the relaxation cycles appears for the λ values $O(\varepsilon)$ away from λ_H. The canard explosion of (1.2.7) and canard cycles are visualized in Figure 1.3 and Figure 1.4, respectively.

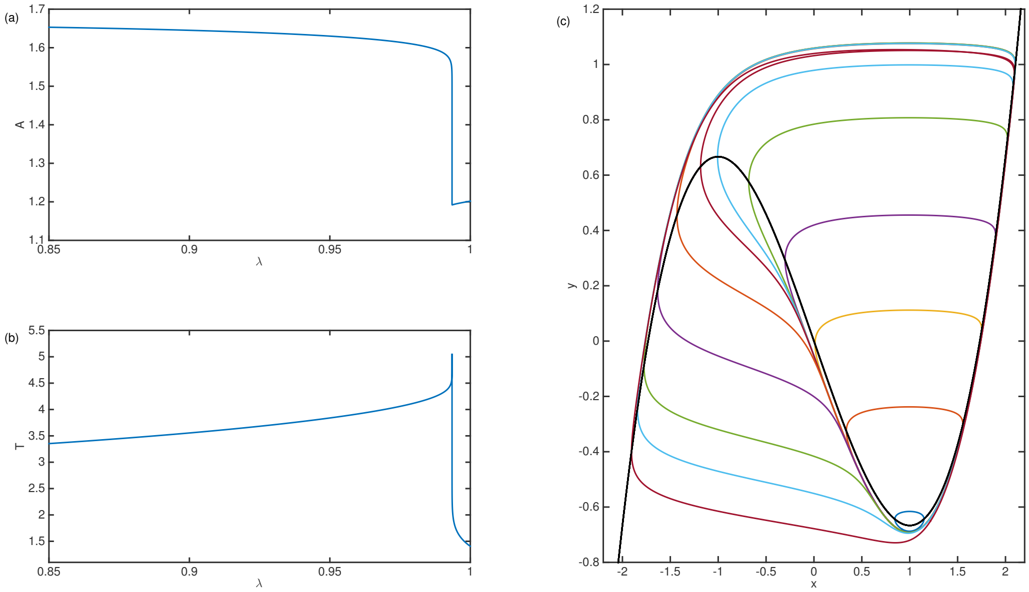

Figure 1.3: (a) Amplitude of the x-component versus λ and (b) period versus λ from the Hopf bifurcation at the lower fold $x = 1$ to relaxation regime for $\varepsilon = 0.05$. (c) Phase portrait of the VDP with selected limit cycles along the canard transition.

1.2.2 Folded singularities

The canard explosion occurs within an exponentially small parameter interval. In higher dimensional slow-fast systems ($\mathbb{R}^n, n \geq 3$), canard solutions persists for $O(1)$ ranges of a parameter. Properties of the equilibria of the DRS (1.2.6) located on the fold set of C, for instance being a saddle, a node or a focus, determine the type of the folded singularities and related canard solutions.

If the equilibrium of DRS is a saddle, then the corresponding fold point is a *folded*

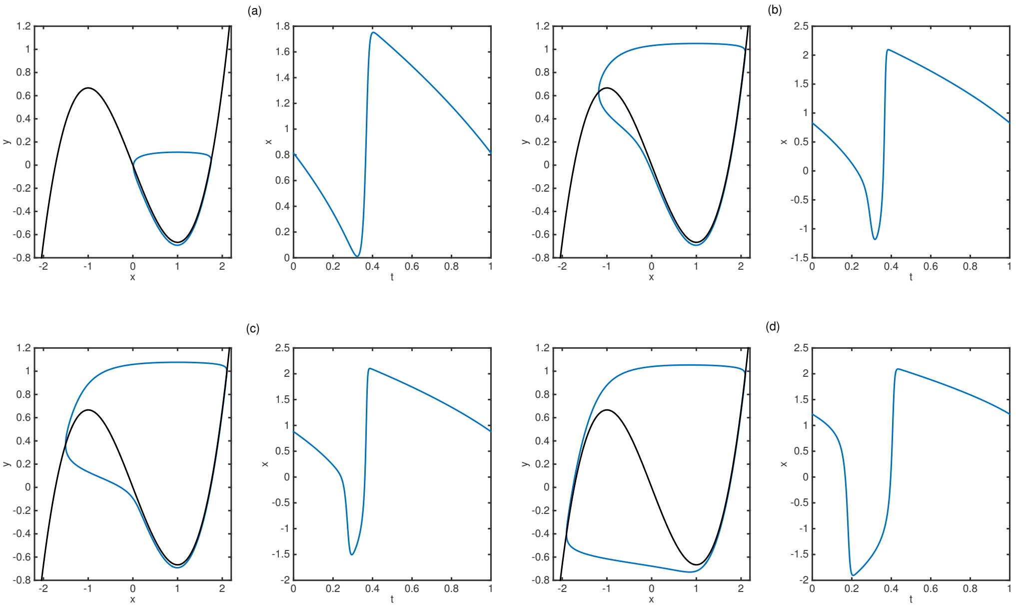

Figure 1.4: Four cycles of the canard explosion at the lower fold in VDP (blue): headless canard in panel (a), maximal canard in panel (b), canard with head in panel (c) and relaxation oscillation in panel (d). In each panel, the left plot corresponds to a phase plane representation of the cycle together with the fast cubic nullcline C, the right panel shows the time trace of the the x variable during the cycle.

saddle. The eigendirections of the folded saddle (as a saddle equilibrium of the DRS) define in the slow flow two special directions that connect attracting and repelling sheets of the critical manifold. Their nonlinear equivalents, namely the stable and unstable manifolds of the folded saddle, provide two special solutions of the slow flow that travel from the attracting sheet to the repelling sheet of C, and from the repelling sheet to the attracting sheet of C, respectively. These two solutions of the slow flow are singular canards, the former being a "true" canard and the latter a "false" (also called "faux") canard (this name is given since it connects the repelling side to the attracting side instead of the opposite as a normal canard). By perturbation, one can prove that these persist for small ε and give a unique canard and a unique false canard in the original system near a folded saddle. They both correspond to the only transverse intersection of attracting and repelling slow manifolds and they are both maximal in the sense that their repelling segment is the longest possible.

Folded-saddle singularities can be related to spiking properties of type-II neurons where the transition from sub-threshold to spiking solutions occurs via a Hopf bifurcation [31]. As showed for the VDP system (1.2.7), a canard explosion is responsible for this transition from sub-threshold (canards without head) to spiking solutions (canards with head and relaxation oscillations). Similar roles of folded-saddle singularities have been identified in HH neurons [20]. In Chapter 2, a pulse adding mechanism related to folded-saddle singularity in (1.1.1) is showed. We also relate folded-saddle singularities with desynchronization of mutually interacting systems. In Chapter 4, we focus on the spiking properties of coupled VDP oscillators.

If the equilibrium of DRS is a node, then the corresponding fold point is a *folded node*. In this case, attracting and repelling slow manifolds intersect transversally $k \geq 1$ times near the folded node. In addition to the strong canards (related to the strong stable manifold of the folded node), *secondary canards* appear in the system. The strong canards cross one of the transversal intersection points and the secondary canards cross from the others. A trajectory entering to the region of the folded node can make k number of turns and produces small amplitude oscillations (SAOs) and then leaves the region. In the presence of a global return mechanism, that takes the trajectory back to the region of the SAOs, SAOs are combined with large amplitude oscillations (LAOs) and consequently MMOs appear in the system.

Key theoretical results on how MMOs arise in slow-fast systems with SAOs have been detailed in [15] and example structures have been showed in a reduced HH model and Belousov-Zhabotinsky reaction. In [5], the authors have showed SAOs due to a folded-node singularity and the global return mechanism in (1.1.1). These mechanisms are responsible for the presence of a plateau (which we term the “pause”) with small oscillations in the (x, y) subsystem of (1.1.1). As shown in Chapter 2, exponentially small variations of a regular parameter in (1.1.1) lead to canard explosions near the folded-node singularity that change the number of SAOs and pulses, simultaneously. Similar canard explosions near the folded-nodes (subject to the coupling) lead to a synchronization or to a desynchronization depending on the characteristics of the interacting systems [32] (See Chapter 2).

1.2.3 Numerical continuation in slow-fast systems

Extreme sensitivity to parameters and repelling slow manifolds limits the usage of classical integration techniques in slow-fast systems to follow families of solution segments near slow manifolds. On the other hand, boundary value problem (BVP) solvers implemented in continuation packages like AUTO can deal with these difficulties [14], in particular in computing the limit cycles of Liénard systems (e.g. VDP and FHN equations). A BVP solver and numerical continuation allow us to find and then follow one-parameter families of orbit segments.

Essential objects determining the behavior of canard solutions are the slow manifolds. Computation of slow manifolds can be formulated as two-point BVP problems and it is very straightforward in minimal systems (a system with a quadratic critical manifold and a constantly changing bifurcation parameter), which approximate the dynamics in the neighborhood of folds [15]. In Chapter 2, we propose a 5-dimensional (5D) minimal model (2 subsystems with quadratic critical manifolds subject to the same constantly changing bifurcation parameter) to approximate the dynamics in the neighborhood of coupled folded singularities. Using this model, we compute slow manifolds for coupled systems and show the presence of canard solutions in coupled systems of higher dimensions, such as $\mathbb{R}^n$ and $n \geq 6$.

Numerical continuation methods are widely used to compute bifurcation diagrams. In Chapters 3 and 4 we use numerical continuation techniques to show bifurcation structures in the synchronized solutions of the coupled secretors. In Chapter 4, we also propose a strategy based on numerical continuation to compute a family of limit cycles, specifically canard orbits, and at the same time a family of periodic non-trivial solutions to the associated adjoint problem.

1.3 Synchronization and weakly coupled oscillators theory

Collective dynamics of coupled slow-fast oscillators have a great importance in the context of neuroscience when microscopic (individual neurons) and macroscopic (networks) levels can be represented as relaxation oscillators [33]. System dynamics arise through the interaction between the intrinsic properties of the individual oscillators (multiple timescales, canard structure), the properties of connections (inhibitory, excitatory) and the network topology. Synchronization of multiple timescale systems may involve synchrony of fast timescale dynamics, such as spikes, and/or slow timescale dynamics, such as bursts. The case of bursting activity, that is the alternation between slow quasi steady-state activity and fast oscillatory dynamics, introduces the question of the main mechanisms underlying transitions to synchronization and robustness of synchronization [34, 35, 36, 37, 38]. In this context, the effect of canard solutions has been considered in several aspects such as formation of clusters, synchrony, phase dynamics and amplitude [39, 40, 41, 27, 42].

Theoretical and numerical tools have been developed to achieve a better understanding of synchronization in slow-fast systems in the context of neuroscience, such as fast threshold modulation theory [43], singular perturbation methods [44, 45, 46, 47], and phase response curves (PRC) [33, 48, 49, 50, 51, 52, 53, 54, 55, 56, 57]. The *(infinitesimal) phase response curve* or *(i)PRC* encodes how a small perturbation affects the phase of an oscillator when applied along the associated stable limit cycle solution. The derivation of the PRC relies on the linearization of the system along the unperturbed (i.e. uncoupled) cycle and is closely related to the adjoint variational equation. Solutions to the adjoint problem and PRCs give insights on the synchronization properties of coupled oscillating systems [33, 49] when the coupling strength is small enough. Such studies are gathered under the name “weakly coupled oscillator theory” [48]. This theory has been linked with earlier studies from Malkin [58, 59] by Izhikevich and Hoppensteadt in [48].

The weakly coupled oscillators theory has been extended to relaxation cycles in [60, 34] by taking the singular limit approximation, considering the attracting branches of the critical manifold in place of the slow segments of relaxation cycles, and instantaneous jumps in place of fast segments, but the consequence of using this setup is that the canard regime has not been dealt with. In Chapter 4, we link earlier studies on weakly coupled oscillators to the canard cycles both numerically and analytically.

Other interests in synchronization of systems motivated by neuronal dynamics have been the effects of intrinsic properties, slowly varying terms on the phase dynamics [53, 57, 61, 55] and derivation of analytic expressions for PRCs [62, 63, 64]. In Chapters 2 and 3, we study effects of canard solutions and dynamic bifurcations on the collective dynamics of coupled bursting systems.

1.3.1 Phase response curve and adjoints

PRCs describe the phase shifts along a stable limit cycle of a dynamical system in response to a stimulus. Weakly coupled oscillator theory [65, 66, 48] is used to predict the phase-locking properties of coupled oscillating system with a “small enough” coupling strength. This theory, which reduces the dynamics of oscillators to a phase variable, implies that coupling has small effects that can accumulate over time and lead to phase-locking behaviors. IPRCs correspond to PRCs in the limit of infinitesimal stimulus. One way to compute iPRCs is by means of non-trivial solutions to the adjoint variational equation associated to the stable limit cycle under consideration; there are numerous other approaches, see e.g. [33, 49].

Consider a dynamical system in $\mathbb{R}^n$

$$\frac{dX}{dt} = F(X) \tag{1.3.1}$$

that possesses a T-periodic asymptotically stable limit cycle γ. A phase variable $\phi \in [0, T)$ is defined along the limit cycle γ parameterized by time and it is typically normalized to 1 or to 2π. It can be associated with points on the cycle by writing $\phi = \Theta(x)$ for $x \in \gamma$. Then, perturbing a point x on the limit cycle with corresponding phase $\phi = \Theta(x)$ (which we can also write as $x = X(\phi)$) by a small quantity $y \in \mathbb{R}^n$ leads to a delay or an advance of the phase. The new phase ϕ' is given by

$$\phi' = \phi + \nabla_X \Theta(x).y + O(||y||^2)$$

and the difference between the old and new phases for small perturbations are expressed as

$$\phi' - \phi = \nabla_X \Theta(x).y.$$

The vector function Z defined by $Z(\phi) = \nabla_X \Theta(X(\phi)))$ is the gradient of the phase map describing how infinitesimal perturbations on any system variable along the limit cycle changes its phase. The function Z (which depends on ϕ or equivalently on $t \in [0, T]$) is the solution of the adjoint variational equation

$$\frac{dZ(t)}{dt} + A(t)^T Z(t) = 0 \tag{1.3.2}$$

which satisfies the normalization condition

$$Z(t)\frac{dX_0(t)}{dt} = 1, \tag{1.3.3}$$

where

$$A(t) = D_X F(X)|_\gamma$$

is the linearization of system (1.3.1) around the limit cycle γ. The adjoint equation should be integrated backwards in time to eliminate all the transient components except the periodic one, which gives the solution. An algorithm to compute solutions to adjoint equations, based on backward integration, is embedded in software packages such as XPPAUT [67] or MATLAB.

1.3.2 Interaction function

The behavior of the adjoint solutions (or equivalently, of the iPRCs) provides predictions on the collective behavior in the weak coupling regime via the *interaction function* which is the convolution of the adjoint solutions and coupling function [66, 58, 59, 49, 48]. In identical systems the interaction function of the i-th oscillator reads:

$$H_i(\phi_j - \phi_i) = \frac{1}{T}\int_0^T Z(t)U_i(\gamma(t), \gamma(t + \phi_j - \phi_i))dt. \tag{1.3.4}$$

where $\phi_j - \phi_i$ $(i = (1, 2), j = 3 - i)$ is the phase difference between the two oscillators and U is the coupling function. The dynamics of the phase difference, $\phi = \phi_j - \phi_i$, is described by the following equation

$$\frac{d\phi}{dt} = \alpha[H_2(-\phi) - H_1(\phi)] = \alpha G(\phi). \tag{1.3.5}$$

where α is the coupling strength. Equation (1.3.5) has a stable solution at ϕ^* if $G'(\phi^*) < 0$, meaning that the two oscillators will synchronize with a phase difference ϕ^*. The solution $\phi^* = 0$ corresponds to in-phase synchronization, $\phi^* = \pi$ (or equivalently $\phi^* = 0.5$ if the phase is rescaled to [0,1]) to anti-phase synchronization, and any other value of ϕ^* corresponds to out-of-phase synchronization of coupled oscillators.

1.4 Contributions and outline of the dissertation

This dissertation investigates synchronization properties of slow-fast oscillators inspired from neuronal dynamics, focusing on the effects of canard phenomena and dynamic bifurcations on the collective behavior. The starting point is the 4D system in (1.1.1), which accounts for the secretion pattern of the GnRH.

The 4D model provides a mean-field approximation to the dynamics of GnRH secreting neurons. In the first two chapters of this dissertation, we introduce heterogeneity in the initial model by considering 2 distinct subpopulations of secretory neurons. This can be considered as the first step of a multiscale top-down approach, going from a macroscopic scale to a more mesoscopic approach. We extend (1.1.1) to 6-dimension (6D) by adding one more secretor modeled as a FHN oscillator receiving the same regulatory signal. The general form of the new system with the coupling terms $I^{(1),(2)}$ reads:

$$\begin{aligned}
\varepsilon\delta\dot{x_1} &= -y_1 + f(x_1), \\
\delta\dot{y_1} &= a_0^{(1)}x_1 + a_1^{(1)}y_1 + a_2^{(1)} + c^{(1)}X + I^{(1)}(x_1, x_2, y_1, y_2, X, Y), \\
\varepsilon\delta\dot{x_2} &= -y_2 + f(x_2), \\
\delta\dot{y_2} &= a_0^{(2)}x_2 + a_1^{(2)}y_2 + a_2^{(2)} + c^{(2)}X + I^{(2)}(x_1, x_2, y_1, y_2, X, Y), \\
\delta\dot{X} &= -Y + G(X), \\
\dot{Y} &= b_0X + b_1Y + b_2.
\end{aligned} \tag{1.4.1}$$

In the second chapter, we consider a parameter set ensuring the periodic alternation between the pulsatile and surge regime without aiming at any biological interpretation. We first study effects of local variations near the folded singularities of an uncoupled one secretor and one regulator configuration (the original 4D model) on the secretion pattern. We show that exponentially small variations of a regular parameter can lead to change in the number of pulses and SAOs via canard explosions. We prove that existing folded singularities in the original model persist under coupling using numerical continuation techniques. We then focus on the effects of the slow-fast transitions in the presence of a linear coupling between the secretors in (1.4.1). In particular, we explore the impact of the relationship between the canard structures and the coupling on patterns of synchronization and desynchronization of the collective dynamics of the resulting 6D system. We identified two sources of (de)synchronization induced by canards belonging to different types of folded singularities. We show that small and local differences can apply $O(1)$ differences in the global output.

In the third chapter, we consider (1.4.1) with a parameter set satisfying the quantitative behavior of the GnRH secretion. We cope with long duration of the pulsatile regime, progressive increase in pulse frequency and ratio between pulse and surge amplitudes. We aim at modeling complex behaviors of the GnRH secretion not captured by the 4D model; a surge with two bumps, so-called a *camel surge*, and partial desynchronization before the surge. We model the camel surge by introducing a regulator-dependent asymmetric coupling function between the secretors. We reveal the impact of slowly varying system variables on the pulsatile dynamics which leads to dynamic bifurcation and causes desynchronization. We combine numerical and analytic tools to assess quantitative information on camel surge and partial desynchronization. We reproduce two experimental instances of camel surges with or without partial desynchronization present in the GnRH literature.

In the fourth chapter, with the motivation of canard-mediated variations in the collective behavior of (1.4.1) studied in the second chapter, we focus on the relation between canards and coupling in the simplest systems with canard cycles, that is mutually coupled VDP systems which evolve on the same time scales. We extend previous results on PRCs and weakly coupled slow-fast oscillators to the case of canard cycles by bridging the gap between the Hopf oscillators and slow-fast cycles. We use numerical continuation techniques to solve the adjoint equations. We also propose an implicit formula for computing the adjoint solutions of the linearized limit cycles of Liénard type systems. We show that synchronization properties of canard cycles are different than those of classical relaxation cycles. In particular, we show that maximal canards separate two distinct synchronization regimes: the Hopf regime and the relaxation regime. Phase plane analysis of slow-fast oscillators undergoing a canard explosion provides an explanation for this change of synchronization properties across the maximal canard. We detail effects of homogeneous coupling strengths and question the limit of PRCs in canard cycles.

Chapter 2

Canard-mediated (de)synchronization in coupled phantom bursters

Elif Köksal Ersöz [1], Mathieu Desroches [2], Martin Krupa [2] and Frédérique Clément [1]

Published in SIAM J. Applied Dynamical Systems, 15 (1), pp. 580-608, 2016 (see [32])

Abstract

In this work, we study canard-mediated transitions in mutually coupled phantom bursters. We extend a multiple-timescale model which provides a sequence of dynamic events, i.e. transition from a frequency modulated relaxation cycle to a quasi-steady state and resumption of the relaxation regime through small amplitude oscillations. Folded singularities and associated canard solutions have a particular impact on the dynamics of the original system, which consists of two feedforward coupled FitzHugh-Nagumo oscillators, where the slow subsystem (regulator) controls the periodic behavior of the fast subsystem (secretor). We first investigate the variability in the dynamics depending on the canard mechanism that occurs near the folded singularities of the 4D secretor-regulator configuration. Then, we introduce a second secretor and focus on the slow-fast transitions in the presence of a linear coupling between the secretors. In particular, we explore the impact of the relationship between the canard structures and the coupling on patterns of synchronization and desynchronization of the collective dynamics of the resulting 6D system. We identify two different sources of desynchronization induced by canards, near a folded-saddle singularity and a folded-node singularity, respectively.

---

[1] INRIA Paris Research Centre, MYCENAE Project-Team, 2 Rue Simone Iff, CS 42112, 75589 Paris cedex 12, France.

[2] INRIA Paris Research Centre, MYCENAE Project-Team, 2 Rue Simone Iff, CS 42112, 75589 Paris cedex 12, France. Current address: MathNeuro Team, Inria Sophia Antipolis Méditerranée Research Centre, 2004 route des Lucioles - BP93 06902 Sophia Antipolis cedex, France.

AMS subject classification

34C15, 34C26, 34D06, 34E17, 70K70, 92B05, 92B25

Key words

canards, synchronization, slow-fast systems, multiple timescales, folded singularity

2.1 Introduction

Physiological rhythms, such as the activity patterns of neurons or the release of hormones, evolve on multiple timescales and can be modeled by using singularly perturbed, so-called *slow-fast*, dynamical systems [33, 68]. Complex behaviors of such systems result from the multiple timescales and they are often organized by underlying canard phenomena [6]. In this work, we study canard-induced slow-fast transitions due to the presence of so-called *folded singularities* in coupled phantom bursters such as those that were initially introduced to represent the secretion dynamics of the Gonadotropin Releasing Hormone (GnRH) [1]. In particular, we study the relation between the canard structures and the coupling, and we intend to investigate their effects on the collective dynamics of the resulting coupled system.

The term *canard* refers to a class of limit cycles first described in the van der Pol equation which stay close to an unstable slow manifold. Canards occur in singularly perturbed dynamical systems in regions of the phase space where normal hyperbolicity (i.e., loosely speaking, hyperbolicity in the fast direction) of the *critical manifold* (fast nullsurface) is lost. Such events happen due to a bifurcation of the fast dynamics, that is, the subsystem obtained when "freezing" the slow variables, hence considered as parameters. In this context, a solution is called canard if it follows an attracting slow manifold, passes close to a bifurcation point of the fast subsystem — a so-called *canard point*, also referred to as *folded singularity* in systems with at least two slow variables— and then follows a repelling slow manifold —also referred to as *canard segment*. In planar systems, canard cycles exist in a very narrow range of control parameters — an interval that is exponentially small in the timescale separation parameter ε — and these sharp transitions upon parameter variation through the canard regime are called *canard explosions*. In higher-dimensional systems, the canard phenomenon can be more "robust", that is, canards can exist for $O(1)$ parameter intervals. In particular, this is the case in three-dimensional systems with one fast variable and two slow variables, where canard-induced *mixed-mode oscillations* (MMOs) can occur. MMOs are trajectories which consist of noticeable large and small amplitude oscillations, reappearing recurrently (periodically or not), and that can be observed in models used in various application areas. There is a recent interest in MMOs in the context of the generalized canard phenomenon in slow-fast systems, since the underlying dynamics are due to the existence of a canard structure [15]. This argument has contributed to explain the complex rhythms in neuron dynamics, e.g. excitability threshold in Hodgkin-Huxley formalism [22], firing mechanism in dopaminergic neurons [19] and subthreshold oscillations in stellate cells [21].

Collective dynamics of coupled slow-fast oscillators have a great importance in the context of physiology when microscopic and macroscopic levels can be represented as relaxation oscillators [33]. System dynamics arise through the interaction between the intrinsic properties of the individual oscillators (multiple timescales, canard structure), the properties of connections (inhibitory, excitatory) and the network topology. Synchronization of multiple timescale systems may involve synchrony of fast timescale dynamics, such as spikes, and/or slow timescale dynamics, such as bursts. The case of bursting activity, that is the alternation between slow quasi steady-state activity and fast oscillatory dynamics, introduces the question of the main mechanisms underlying transitions to synchronization and robustness of synchronization [34]. In this context, the effect of canard solutions has been considered in several aspects such as formation of clusters, synchrony and phase dynamics [40, 60].

Since the intrinsic properties of relaxation oscillators differ from those of harmonic oscillators, dedicated tools have been required to understand the synchronization properties of such systems. Yet some concepts can still be transferred without loss of generality, for instance two mutually coupled slow-fast oscillators are called *synchronous* if their respective pulses are generated at the same time (*in-phase*) or with a constant phase shift (*anti-phase* for a π-phase shift and *out-of-phase* for any other phase value). Somers and Kopell [43] have presented a theory on anti-phase synchronization of coupled relaxation oscillators, namely *fast threshold modulation*. In this work, the interaction has been provided by a heaviside coupling function that acts to modify the position of the fast nullcline. Possibility of canard solutions in such a coupling scheme has been showed numerically in [14]. Izhikevich [60] has extended phase models to relaxation oscillators and applied to *weakly coupled* oscillators under the assumption that the coupling strength is less than the timescale parameters of each individual oscillator. In his paper the canard regime is not considered since the phase equations are singular at the canard point. More recently, the importance of the underlying canard structure together with the weak coupling in the formation of clusters and synchronization in a network of slow-fast systems has been investigated by Ermentrout and Wechselberger. In [40], they pointed out the effect of MMOs on the *phase-resetting curves* (PRC).

In the present work, we focus on the effect of canards on collective dynamics of an extended version of a neuroendocrine model which accounts for the alternating pulse and surge pattern of GnRH secretion introduced in [1]. The model is formed by two FitzHugh-Nagumo oscillators that evolve on different timescales, with a feedforward coupling from the slow one (regulating system) to the fast one (secreting system). The resulting 4D model involves three different timescales. So far, global and local features of the model have been studied in the context of slow-fast dynamics and MMOs where folded singularities and associated canard trajectories have a particular importance [5]. For instance, so-called *secondary canards* due to a folded node have been shown in [5] to be responsible for the presence of a plateau (which we term the “pause”) with small oscillations in the model output, after the surge and before the pulsatility resumption. Here, we extend the model to 6D by adding one more secretor and focus on the slow-fast transitions in the presence of coupling. We explore the influence of the relationship between canard structures and coupling on patterns of synchronization and desynchronization. We choose a simple linear coupling as a first attempt to investigate a modulation of the secreting activity of two populations that can influence each other without aiming at any biophysical interpretation. Such a phenomenological approach to determine the mathematical mechanism underlying neural dynamics has been recently adopted in [69]. We propose two different sources of desynchronization, induced by canards near a folded node (*folded-node singularity*) and canards near a folded saddle (*folded-saddle singularity*), respectively. Our work differs from [60] by two key aspects: there is no global phase reduction available for our model since we mostly focus on the fold regions, and the isochrons are very complicated due to the presence of canards.

This chapter is organized as follows: In Section 2.2 we revisit the 4D GnRH secretion model and show the variability induced by canard mechanisms in the dynamics, adding to [5] the link between the presence of a folded-saddle singularity at the lower fold of the critical manifold, and the canard-induced variability before the surge. In Section 2.3 we present the extended 6D model, justify the existence of canard structures in coupled systems using a minimal model, and show the influence of the canard solutions on the collective dynamics of the coupled system. Finally, we conclude in Section 2.4.

2.2 4D model

The model (1.1.1) (and rewritten in (2.2.1) to remind it to the reader) proposed and studied in [1, 3, 4] captures the complex dynamics of the populations interacting within the GnRH neural network. This model, which can be classified as a phantom burster, consists of 2 coupled FitzHugh-Nagumo oscillators with different timescales. The slow system (X, Y) stands as the regulating population, so-called *regulator*, whereas the fast system (x, y) represents the secreting population, so-called *secretor*, and the solution component $y(t)$, which corresponds to the GnRH secretion along time, can be referred as the output of the system. The coupling between both systems leads to a three-timescale model which is able to capture not only the periodic transition between the pulsatile and surge patterns of the GnRH secretion but also other biological features such as the changes in the frequency during the pulse regime. The model reads

$$\begin{aligned}
\varepsilon\delta\dot{x} &= -y + f(x), \\
\delta\dot{y} &= a_0 x + a_1 y + a_2 + cX, \\
\delta\dot{X} &= -Y + g(X), \\
\dot{Y} &= X + b_1 Y + b_2,
\end{aligned} \tag{2.2.1}$$

where

$$\begin{aligned}
&f(x) = \lambda_3 x^3 + \lambda_1 x, \\
&g(X) = \mu_3 X^3 + \mu_1 X, \\
&\lambda_3, \mu_3 < 0, \quad \lambda_1, \mu_1 > 0, \\
&a_i, c > 0, \quad 0 < \varepsilon \ll 1, \quad 0 < \delta \ll 1.
\end{aligned}$$

This model has been previously analyzed in [3] and [5] where conditions on the parameters were obtained in order to guarantee the sequential behavior of the secretor. The critical points of the X-nullcline ($Y = g(X)$) are denoted by $(\pm\gamma, g(\pm\gamma))$, where $\gamma > 0$ and $g'(\pm\gamma) = 0$. These points split the X-nullcline into 3 parts: left, right ($g' < 0$) and middle branch ($g' > 0$). The regulator, (X, Y), has a relaxation limit cycle whose slow parts follow the branches of the cubic function $g(X)$ if some specific conditions are respected by (b_1, b_2) ensuring that the stationary point on the middle branch is an unstable focus (see Fig. 2.1 (a)). We also denote the minimum and maximum values of X on this cycle by X_{min} and X_{max}, respectively.

The regulator dynamics influence the secretor system via the coupling term cX. The x-nullcline ($y = f(x)$) is a cubic function with 2 fold points $(x_{f\pm}, f(x_{f\pm}))$ where $f'(x_{f\pm}) = 0$. These fold points divide the x-nullcline into 3 branches, i.e. left, right ($f' < 0$) and middle ($f' > 0$), as in the (X, Y) system. The y-nullcline driven by X ($a_0x + a_1y + a_2 + cX = 0$) moves in the secretor phase plane and consequently the number and position of the singular points (of the (x, y) fast system parametrized by X) with respect to the folds of the x-nullcline change. In our framework, the repertoire of phase plane configurations in system (x, y) is limited due to a restriction of the parameter space by appropriate constraints detailed in [3, 5], and the dynamics can be organized according to the 4 phases in the (X, Y) relaxation cycle (Fig. 2.1):

- **Phase-1:** ***pulsatile regime***; during the slow increase in X from $X = X_{min}$ to $X \simeq -\gamma$, the y-nullcline intersects the x-nullcline in such a way that the (x, y)-system possesses an unstable equilibrium surrounded by a stable relaxation cycle. The motion of (X, Y) with $O(1)$-speed drives the y-nullcline to the left. The velocity in the neighborhood of the relaxation cycle is on the order of $O(1/\delta)$ along the branches of the cubic $y = f(x)$ and $O(1/\varepsilon\delta)$ during the jumps from one branch to another. Depending on the parameter values, hence on the exact location of the y-nullcine for $X \approx X_{min}$, the pulsatile regime can be preceded by a "pause" with small amplitude oscillations.

- **Phase-2:** ***transition from the pulsatile regime to surge***; during the rightwards jump in X from $X \simeq -\gamma$ to $X = X_{max}$, the y-nullcline moves to the left branch of $y = f(x)$. The stable limit cycle of the (x, y)-system disappears via a Hopf bifurcation in the fast system in the neighborhood of the local minimum of $y = f(x)$. Depending on the parameters, the y-nullcline may either intersect the left branch of $y = f(x)$ or lie on the left of the cubic $y = f(x)$ at $X = X_{max}$. The two systems (X, Y) and (x, y) change with $O(1/\delta)$-speed.

- **Phase-3:** ***surge***; during the slow decrease in X from $X = X_{max}$ to $X \simeq \gamma$, (x, y) moves along the left branch of $y = f(x)$ with an $O(1/\delta)$-speed, which corresponds to both the ascending and descending parts of the surge. The maximal amplitude reached during the surge is defined by the subtle interplay between the location of the current (x, y) point and the ordinate of the leftmost intersection point between the x and y nullclines, that is the highest at the very beginning of the surge, when X jumps to its maximal value X_{max}, before decreasing slowly. As long as the the current (x, y) point is below the quasi-stationary point (whose existence is guaranteed by constraints 3 and 4 in Table 2.1), it tracks it and keeps on climbing the left branch (ascending part of the surge). Thereafter, it goes down the branch (descending part of the surge).

- **Phase-4:** ***transition from the surge to pulsatile regime***; during the leftwards jump in X from $X \simeq \gamma$ to X_{min}, the y-nullcline moves to the vicinity of the local maximum of $y = f(x)$ with $O(1/\delta)$-speed and the relaxation cycle appears again. The output signal $y(t)$ decreases since (x, y) is attracted by the limit cycle.

In the regions near the fold points of the (x, y) fast nullcline, interesting dynamics may occur due to the presence of underlying canard solutions, and this happens both when X is slower than y (upper fold point) and when X has the same speed as y (lower fold point). The possibility of a Hopf bifurcation near the upper fold of the x-nullcline, $(x_{f+}, f(x_{f+}))$, in the early stages of Phase-1 and the existence of canard solutions have been the main focus of [5]. Although canard explosions near the lower fold $(x_{f-}, f(x_{f-}))$ during Phase-2 has been mentioned, a detailed study was not provided. In the following subsections, we examine the geometry of the fold regions, corresponding canard solutions and their effects on the output variable $y(t)$. Before going further, we recall a widely used method to analyze the canard phenomenon, the so-called *desingularized reduced system.*

Desingularized reduced system Let us consider a general slow-fast system with one fast variable x and two slow variables (y, z)

$$\begin{aligned} \varepsilon\dot{x} &= f(x, y, z, \varepsilon), \\ \dot{y} &= g(x, y, z, \varepsilon), \\ \dot{z} &= h(x, y, z, \varepsilon). \end{aligned} \tag{2.2.2}$$

The critical manifold $C^0 = \{(x, y, z); f(x, y, z, 0) = 0\}$ is defined as the nullcline for the fast variable (and for $\varepsilon = 0$). It approximates (to zeroth order in ε) the region of the phase space where the slow dynamics take place. The reduced system is obtained by setting $\varepsilon = 0$ in (2.2.2), which gives a differential-algebraic system whose flow can be analyzed by differentiating the equation of C^0 with respect to time, giving (after projection onto the (x, z)-plane)

$$\begin{aligned} -f_x(x, y, z, 0)\dot{x} &= f_y(x, y, z, 0)g(x, y, z, 0) + f_z(x, y, z, 0)h(x, y, z, 0), \\ \dot{z} &= h(x, y, z, 0), \end{aligned}$$

where $z = z(x, y)$ on the critical manifold. The resulting system is singular along the folds of C^0 with respect to the x-variable (that is, when $f_x = 0$). Desingularizing the reduced system by means of the time rescaling $t = -f_x(x, y, 0)\tau$ allows one to understand the slow flow up to the fold curve(s) of C^0. This is where canard solutions can appear due to the existence of equilibria of the desingularized reduced systems. Such points are not equilibria of the reduced systems and they are referred to as *folded singularities*. Note that rescaling factor $t = -f_x(x, y, 0)\tau$ changes the orientation of the vector field when $f_x(x, y, z) < 0$.

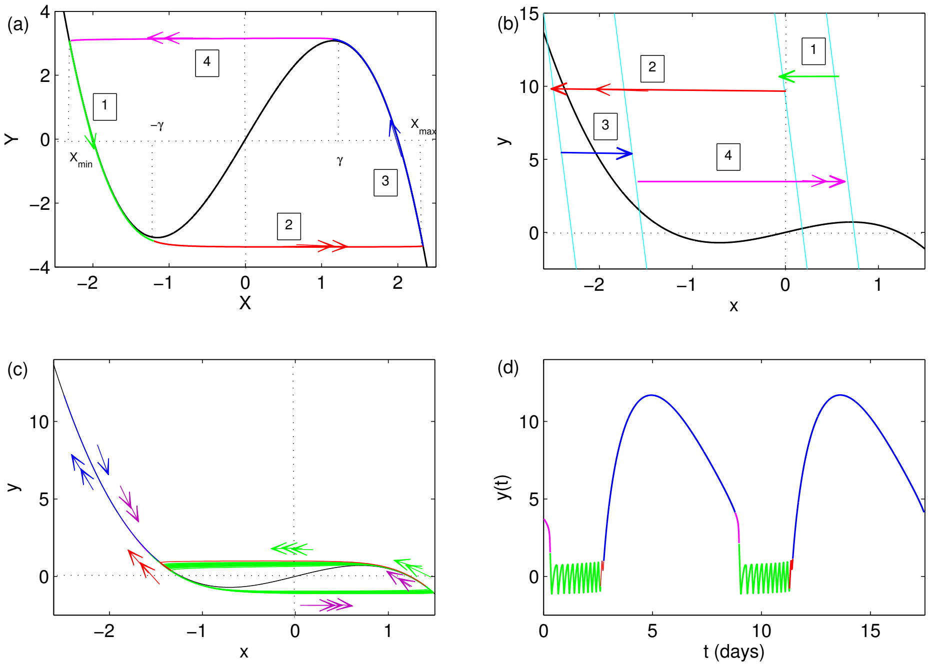

Figure 2.1: 4 phase dependent dynamic behavior obtained with the parameter set given in Table 2.2. (a) Attracting relaxation cycle in the (X, Y) phase plane. Each number represents a different phase of the periodic behavior. 2-headed arrows indicate an $O(1/\delta)$ speed, 1-headed arrows indicate an $O(1)$ speed. (b) Position of the nullclines on the (x, y) phase plane with respect to the 4 phases in the (X, Y) limit cycle. Green arrow: direction of y-nullcline during the pulsatile phase. Red arrow: transition from pulsatility to surge. Blue arrow: surge phase. Pink arrow: transition from surge to pulsatility. (c) Projection of a trajectory onto (x, y) plane. Colors represent the phases and 3-headed arrows represent $O(1/\varepsilon\delta)$-speed motion. (d) Traces in time of the output variable $y(t)$ colored with respect to the phases. Note that, for the sake of numerical continuation feasibility, the respective durations of the slow phases are not realistic from a biological viewpoint; the relative duration of the surge is exaggerated, while the total number of pulses in Phase-1 is drastically reduced. This change in the quantitative features of the model is made without loss of generality in the study of the transition phases that are rather the focus of this work.

The general process of desingularization can be used to understand the dynamics in the neighborhood of the fold regions. In the following subsections, we will reduce (2.2.1) to analyze the dynamics in Phase-1 and Phase-2 where canard solutions introduce variations in the output signal $y(t)$.

2.2.1 Variability after the surge

The location of the y-nullcline at the very beginning of Phase-1 and the existence of singularities on the critical manifold play a role in the variability after the surge. If the

y-nullcline passes (from right to left) through the right fold point of the cubic $y = f(x)$, then a delayed transition is expected before pulsatility resumption. This *pause* is underlain by a supercritical Hopf bifurcation at the upper fold and characterized by the existence of small amplitude oscillations (SAOs). The slow-fast dynamics during this passage, therefore the canard phenomenon, can be studied via the desingularized reduced system [5].

In Phase-1 the dynamics can be reduced to a three dimensional system. Along the left branch of $Y = g(X)$ curve, in the region ($X_{min} < X < -\gamma$), the current (X, Y) point remains in $O(\delta)$ neighborhood of the $Y = g(X)$ cubic. Hence, it is convenient to assume that $Y = h_\delta(X)$, where $(X, \delta) \mapsto h_\delta(X)$ is an analytic function on $]-\infty, -\gamma[\times\mathbb{R}_+^*$ and $h_0(X) = g(X)$.

$$\begin{aligned} Y &= h_\delta(X) = g(X) + O(\delta), \\ \dot{Y} &= \dot{X}h'_\delta(X) = \dot{X}(g'(X) + O(\delta)). \end{aligned} \tag{2.2.3}$$

By replacing (2.2.3) in (2.2.1), one obtains a three dimensional system with three different timescales, that represents approximately the dynamics during the pulsatile phase:

$$\begin{aligned} \varepsilon\delta\dot{x} &= -y + f(x), \\ \delta\dot{y} &= a_0 x + a_1 y + a_2 + cX, \\ \dot{X} &= \frac{X + b_1(g(X) + O(\delta)) + b_2}{g'(X) + O(\delta)}. \end{aligned} \tag{2.2.4}$$

The folded singularity at the upper fold point $(x_{f+}, f(x_{f+}), X_{f+})$ on the critical manifold surface $C^0 = \{y = f(x)\}$ can be analyzed via the desingularized reduced system:

$$\begin{aligned} \dot{x} &= -(a_0 x + a_1 f(x) + a_2 + cX), \\ \dot{X} &= -\delta f'(x)\left(\frac{X + b_1(g(X) + O(\delta)) + b_2}{g'(X) + O(\delta)}\right), \end{aligned} \tag{2.2.5}$$

which is singular along the fold set of C^0. The equilibrium of (2.2.5) reads

$$\begin{aligned} f'(x_{f+}) &= 0 \\ X_{f+} &= -\frac{1}{c}\left(a_0 x_{f+} + a_1 f(x_{f+}) + a_2\right), \end{aligned}$$

where $x_{f+} = \sqrt{\frac{-\lambda_1}{3\lambda_3}}$. The Jacobian matrix at the equilibrium point of interest reads

$$J = \begin{bmatrix} -a_0 & -c \\ -6\delta\lambda^3 x_{f+}\left(\frac{X_{f+}+b_1(g(X_{f+})+O(\delta))+b_2}{g'(X_{f+})+O(\delta)}\right) & 0 \end{bmatrix}.$$

The eigenvalues of the matrix are given by

$$\xi_{\pm} = \frac{1}{2}\left(-a_0 \pm \sqrt{a_0^2 + 24c\lambda_3 x_{f+}\delta\frac{X_{f+} + b_1(g(X_{f+}) + O(\delta)) + b_2}{g'(X_{f+}) + O(\delta)}}\right).$$

In [5] it has been shown that for $\delta \ll 1$ the equilibrium point of (2.2.5) is a node, so that the corresponding folded singularity of (2.2.4) is a folded node. Near a folded node, trajectories are expected to make SAOs while passing from an attracting slow manifold to a repelling slow manifold; therefore, these solutions are canards. The number of SAOs is related to the number of intersection points between the repelling and attracting slow manifolds near the fold point. These canard solutions are called *kth secondary canards* where k refers to the number of slow manifold intersections. In conjunction with a global return mechanism, this leads to canard-mediated MMOs. As a result, the passage of the y-nullcline through the folded node generates MMO-type periodic solutions; i.e. solutions combining large-amplitude and small-amplitude oscillations in the secretor output with a post-surge pause (Fig. 2.2).

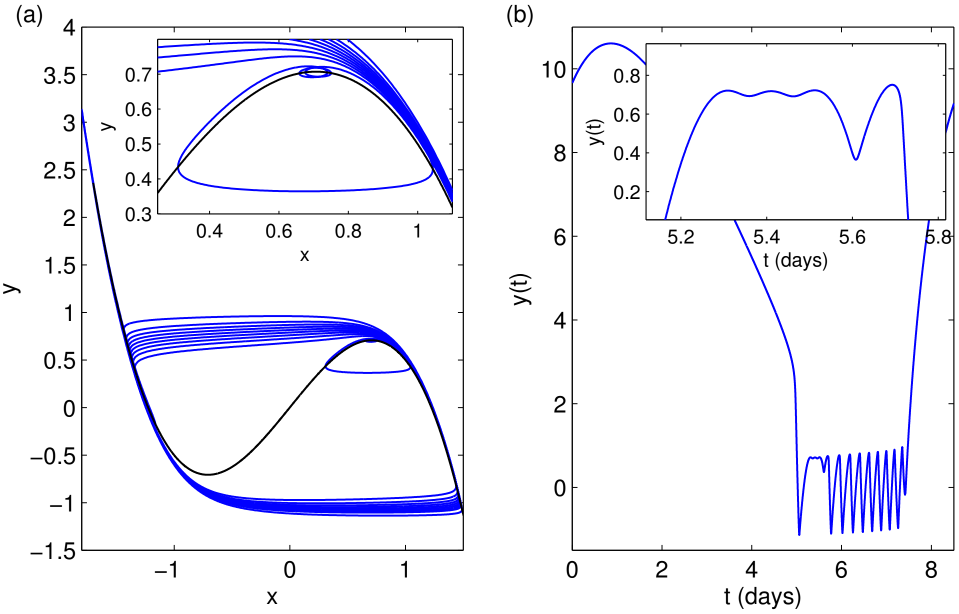

Figure 2.2: Canard solutions near the upper fold and variability after surge. (a) Projection of a MMO-type trajectory with canard cycles near the upper fold onto the (x, y) plane. (b) Corresponding small oscillations superimposed on the post-surge pause.

2.2.2 Variability before the surge

In this section, we extend the work presented in [5] by analyzing the possibility for canard-induced variability before the surge. The position of the y-nullcline during Phase-2 and the presence of singularities on the lower fold may also introduce canard transitions that impact the pre-surge pattern of the output variable. While X moves from $-\gamma$ to X_{max}, point (x, y) may move down along the left branch of $y = f(x)$ towards the lower fold point $(x_{f^-}, f(x_{f^-}))$. Subsequently, point (x, y) might either turn back on the left branch and go to the surge, if the x- and y-nullclines' intersection point lies already on the left branch of $f(x)$, or pass through the fold and make another pulse before moving up to the left branch of the cubic, if the intersection point changes its stability after the passage of (x, y) through the lower fold (Fig. 2.3). Having a canard explosion between these two cases is possible due to the existence of a folded singularity. In order to use the desingularization tool for investigating this folded singularity, we need to obtain a system of equations describing only the corresponding dynamics in Phase-2. During Phase-2 transition, (X, Y) evolves according to the X's timescale and variable Y remains almost constant, such that $Y = g(-\gamma) + O(\delta)$, with an error in $O(\delta)$ which goes to 0 as $\delta \to 0$. The corresponding dynamics can be reduced to the system:

$$\begin{aligned}\varepsilon\dot{x} &= -y + f(x),\\ \dot{y} &= a_0x + a_1y + a_2 + cX,\\ \dot{X} &= -(g(-\gamma) + O(\delta)) + g(X).\end{aligned}$$

The folded singularity at the lower fold point $(x_{f^-}, y_{f^-}, X_{f^-})$ of C^0 surface can also be analyzed via the desingularized reduced system defined locally by

$$\begin{aligned}\dot{x} &= -(a_0x + a_1f(x) + a_2 + cX),\\ \dot{X} &= -f'(x)(-(g(-\gamma) + O(\delta)) + g(X)).\end{aligned}$$

Once again the system is singular since $f'(x_{f^-}) = 0$ for $x_{f^-} = -\sqrt{\frac{-\lambda_1}{3\lambda_3}}$. The singularity at the lower fold can be analyzed by using the equilibrium point of desingularized reduced system; which is:

$$\begin{aligned}x_{f^-} &= -\sqrt{\frac{-\lambda_1}{3\lambda_3}}\\ X_{f^-} &= -\frac{a_0x_{f^-} + a_1f(x_{f^-}) + a_2}{c}.\end{aligned}$$

The Jacobian at the equilibrium point reads

$$J = \begin{bmatrix} -a_0 & -c \\ -6\lambda_3x_{f^-}(-(g(-\gamma) + O(\delta)) + g(X_{f^-})) & 0 \end{bmatrix}.$$

Eigenvalues of the Jacobian matrix are

$$\xi_{\pm} = \frac{1}{2}\left(-a_0 \pm \sqrt{a_0^2 + 24c\lambda_3x_{f^-}(-(g(-\gamma) + O(\delta)) + g(X_{f^-}))}\right).$$

In our setting $c > 0, \lambda_3 < 0$ and $x_{f^-} < 0$, hence $c\lambda_3x_{f^-} > 0$. Therefore the equilibrium point is a saddle and the singularity at the lower fold is a folded saddle where a unique *maximal canard* solution —a solution which remains on the repelling slow manifold—

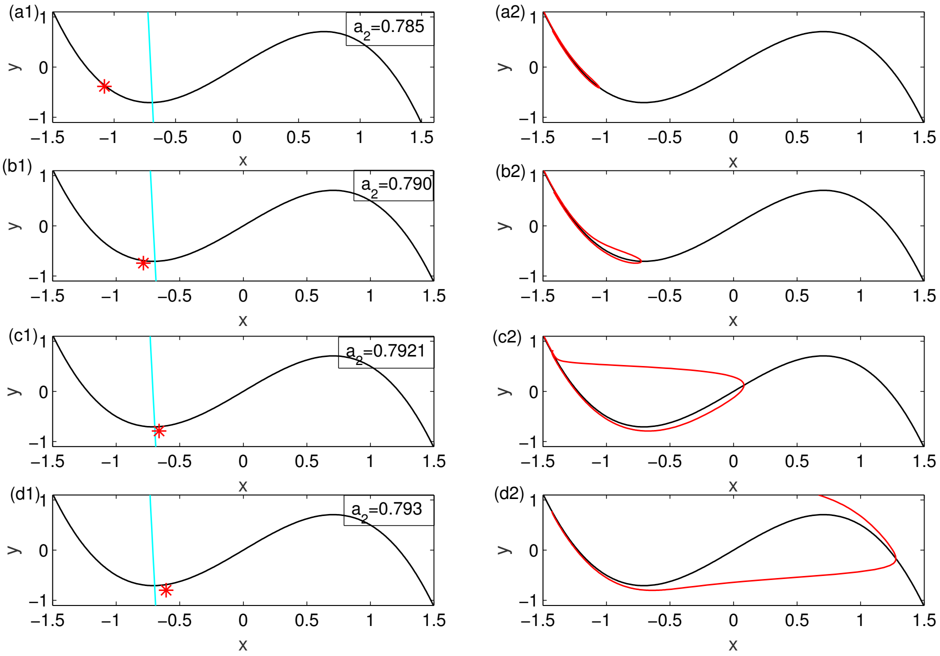

Figure 2.3: Location of point (x, y) (red asterisk), y-nullcline (cyan), x-nullcline (black) and the corresponding trajectory (red line) for different values of a_2 in Phase-2. Depending on the relative locations of the singular point and current (x, y), different types of pre-surge behavior may occur. (a1-b2) Passage of the y-nullcline through the lower knee before (x, y) drives the trajectory to move along the left branch. (c1-d2) Passage of the y-nullcline through the lower knee after (x, y) results in either a canard explosion or jump to the right branch.

exists [70]. Near a folded-saddle singularity, the attracting and repelling slow manifolds intersect only once, therefore, a rotating mechanism like in the folded node case is not possible.

In a two-dimensional (2D) slow-fast system with a cubic critical manifold, canard cycles are divided into two families; *canards without head* and *canard with head* [6]. Canards without head start close to one attracting branch, pass through the fold, continue close to the repelling branch and then jump back to the same attracting branch where they started from. They correspond to curves surrounding a convex region in the phase plane. On the other hand, canards with head escape to the other attracting branch after following the repelling branch and they surround a non-convex region in the phase plane [31]. The maximal canard follows the entire repelling branch from the lower fold point to the upper one. Transition from one family of solutions to other one, via the maximal canard, occurs in an exponentially small parameter variation.

The location of the y-nullcline in (2.2.1) near the folded saddle controls the pre-surge behavior of the solution in several manners. In particular, it determines from which region the surge is triggered (departure region), it affects the departure velocity

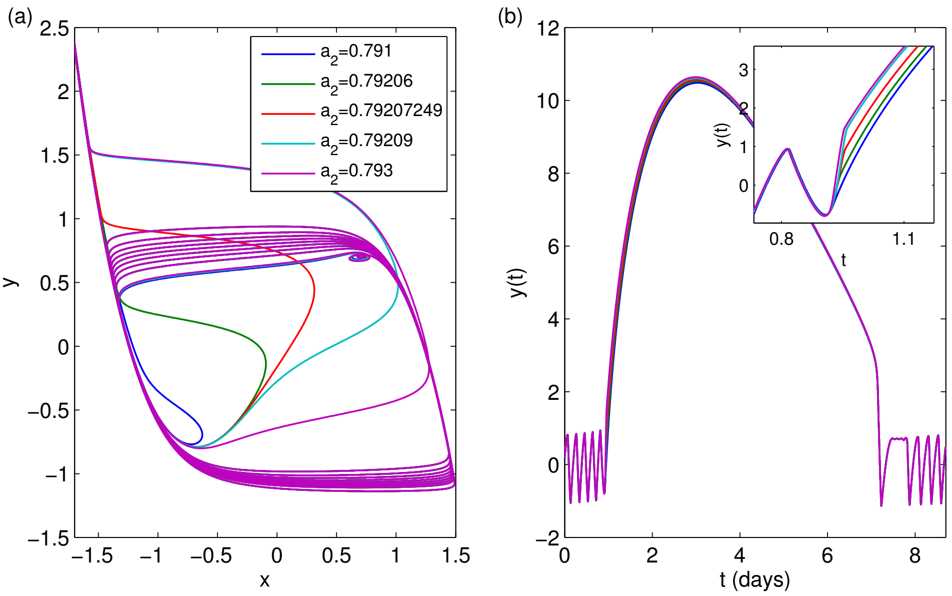

Figure 2.4: Canard solutions near the lower fold and variability before surge. (a) Projection of a bunch of canard solutions near the lower fold onto the (x, y) plane. (b) Corresponding trajectories and effect on the surge timing. If a solution encloses the convex region (blue and green curves for instance), the departure to surge is slow and delayed compared to the non-convex solutions (cyan and purple curves). The maximal canard (red curve) can be considered as a boundary between the slow and fast surge transitions.

and time of surge triggering (surge timing). Figure 2.4 shows canard solutions in (2.2.1) near the lower fold at the beginning of the surge regime and their effects on the outputs. Convex solution segments reach the attracting branch earlier than non-convex solution segments and start to follow the dynamic stable point with an $O(1/\delta)$ speed. On the contrary, non-convex solutions remains in the $O(1/\varepsilon\delta)$ regime in a wider band of the phase plane, thus, they reach an amplitude greater than the pulse quicker than the convex solutions. As a result, a faster change in the $y(t)$ signal is generated by the canards with head, consequently, the surge transition from the non-convex region occurs earlier than the surge transition from the convex region. Finally, the maximal canard as being a boundary between canards without head and canards with head, is also a boundary between slow and fast surge transitions.

As mentioned above, the sequence of dynamic events from Phase-1 to Phase-4 in (2.2.1) is constrained by a reduction of the parameter space. These constraints (summarized in Table 2.1 and presented in [3, 5]) restrict the repertoire of phase plane configurations and tune the order in the sequence of dynamic events by coordinating the slow motion in (X, Y) with the current dynamics of (x, y). They also guarantee the existence of a unique, stable (p, s)-type limit cycle of (2.2.1) consisting of s SAOs, p pulses and one surge. Condition-1 ensures the occurrence of a Hopf bifurcation and rotating canard solutions, thus s SAOs, as explained in Section 2.2.1. Condition-

Table 2.1: List of the conditions needed to obtain a (p, s)-type limit cycle with one surge.

1. The y-nullcline should pass through the upper fold of $f(x)$ to generate s number of SAOs.
2. The relaxation cycle in (x, y) which appears after the passage of y-nullcline through the upper fold should persist all along the descending motion of X to generate p number of pulses.
3. From the beginning of the surge phase, the subsystem (x, y) should admit an attracting node and a saddle on the left branch of $f(x)$.
4. Until the end of the surge phase, the attracting node and saddle on the left branch of $f(x)$ should persist.
5. The return map around the (p, s)-type limit cycle should be contracting.

2 ensures the presence of the relaxation cycle in (x, y) during the pulsatile regime. Condition-3 together with Condition-4 guarantee that sufficient contraction is present during the surge, ascending and descending motions, respectively. Finally, Condition-5 gives the uniqueness and stability of the (p, s)-type limit cycle. Requirements on the parameters can be found in [5].

2.2.3 Effect of canard-induced transitions on the global behavior

For a parameter set which satisfies the conditions in Table 2.1, there exists a unique, stable (p, s)-type limit cycle of (2.2.1) consisting of s number of SAOs, p number of pulses and one surge. Exponentially small variations of a regular parameter can lead to a change in the number of pulses and SAOs via canard explosions [5]. We can identify two types of changes in the periodic limit cycle due to the canard phenomena described in Subsections 2.2.1 and 2.2.2. The first canard-mediated change, *post-surge transition*, occurs near the upper fold and yields a conversion between SAOs and pulses $((p, s) \to (p \pm 1, s \mp 1))$. The second canard-mediated change, *pre-surge transition*, arises near the lower fold and causes an addition or subtraction of a pulse $((p, s) \to (p \pm 1, s))$. These variations also influence the timing of the pulsatility resumption and surge triggering.

In order to display the effects of the canard mediated transitions on the secretion pattern, we consider the parameter set in Table 2.2, which guarantees a 4-phased periodic behavior and fulfills the singularity conditions to obtain a folded node on the upper fold and a folded saddle on the lower fold of the x-nullcline. This parameter set satisfies the qualitative sequence in GnRH secretory events of the experimental pattern of GnRH secretion, but not the quantitative features, such as, the respective durations of the surge and pulse regime (hence of the total number of pulses) and the ratio between the surge and pulse amplitudes [3]. Choosing a_2 as a control parameter allows us to generate canard-mediated transitions on the $(p, s)-$orbit. Figure 2.5 shows a chain of canard-induced transitions occurring in an $O(1)$ range of a_2. The first

Table 2.2: Nominal parameter values used for the simulations. a_2 is considered as a control parameter for fold dynamics. Note that even if the qualitative sequence of secretory events is preserved, the quantitative features, and mostly the respective durations of the surge and pulse regime (hence of the total number of pulses) have moved away from the biological specifications by considering the parameter set here. The choice of the set comes from the constraints imposed by the numerical continuation of the system [5].

ε	0.1	δ	0.05
a_0	1	a_1	0.02
c	0.69	a_2	0.985
b_1	0	b_2	-0.8
λ_3	-1	λ_1	1.5
μ_3	-1	μ_1	4

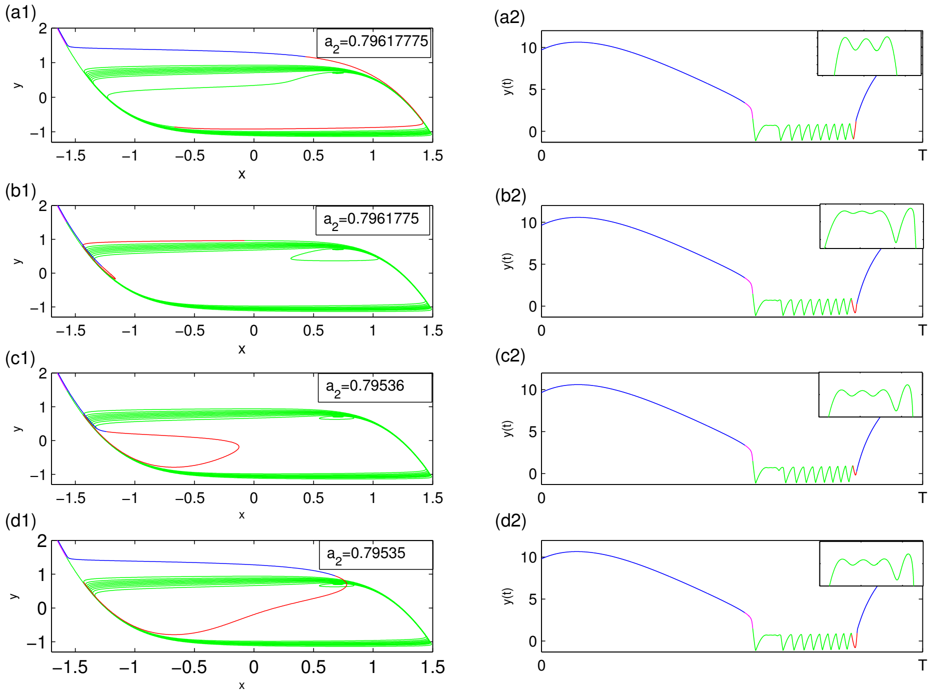

Figure 2.5: Canard-mediated transitions in an $O(1)$ range of a_2. Trajectories are colored with respect to the color code used for the phases in Figure 2.1. (a1-b2) $(p, s) \rightarrow (p-1, s+1)$ post-surge transition. (c1-d2) $(p, s) \rightarrow (p+1, s)$ pre-surge transition. The compete transition from Panel (a1) to Panel (d2) adds one more small oscillation to the pause ($(p, s) \rightarrow (p, s+1)$). Each peak rising during the pause is counted as a SAO.

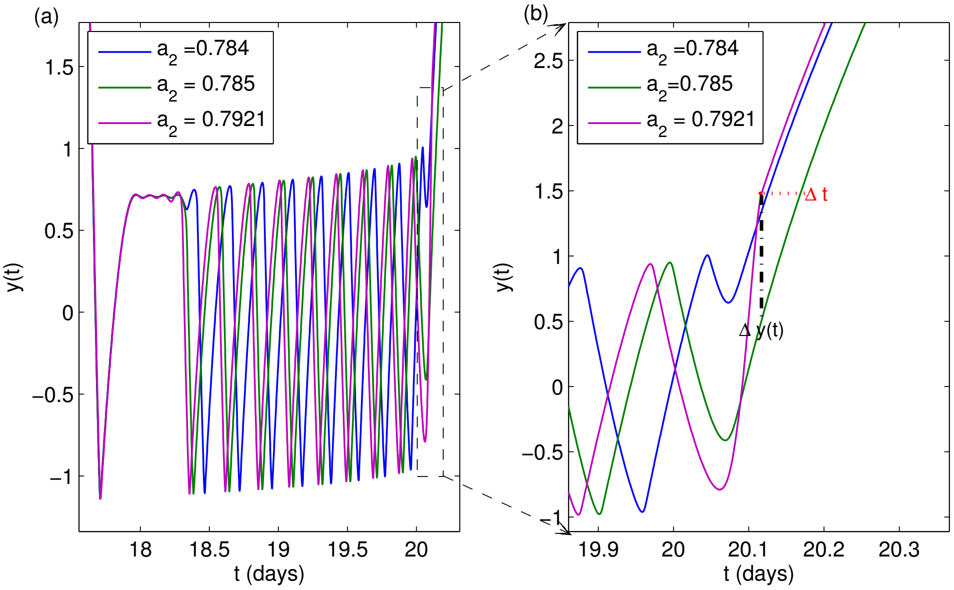

Figure 2.6: Introduction and compensation of surge delay. a_2 acts as a control parameter and determines the number of small oscillations on the upper fold which is a folded node. An increase in a_2 causes the loss of one small oscillation in the post-surge pause, which advances the resumption of the relaxation cycle but delays the subsequent departure to the surge (from the blue trajectory to the green trajectory). The pre-surge transition (from the green trajectory to the magenta) compensate for the delay in the surge triggering. In Panel (b), the red dashed segment labeled Δt represents the time delay between the green and blue line, while the black dashed segment labeled $\Delta y(t)$ illustrates the difference in amplitude in y at the time of the surge triggering for the magenta trajectory.

transition adds one SAO to the pause via a $(p, s) \to (p-1, s+1)$ type of post-surge transition, which corresponds to a loss of one pulse after the pause. The next transition, which is a $(p, s) \to (p+1, s)$ type of pre-surge transition, adds a pulse before the surge. The complete organization can be described as $(p, s) \to (p, s+1)$ variation in the limit cycle.

This canard-mediated organization affects the time profile of the secretor output. The post-surge transition has a global effect on the secretion pattern in such a way that it may advance/delay the resumption of pulses and triggering of the surge. On the other hand, the pre-surge transition has a local effect and only affects the surge timing. Figure 2.6 shows a chain of two canard-mediated transitions in an $O(1)$ range of a_2 alternating pulse and surge timings. The first change, which is a $(p, s) \to (p+1, s-1)$ post-surge transition, advances the resumption of the relaxation oscillation after the pause but delays the surge triggering. The second canard-mediated change is a pre-surge transition and compensates for the delay in the surge introduced by the post-surge transition.

In [5] the authors have illustrated a similar $(p, s) \to (p, s+1)$ transition arising within an exponentially small a_2-range where post and pre-surge changes occur simultaneously. The sensitivity of canard solutions to the changes in parameter values and their impacts on the secretion pattern of the 4D system have motivated us to examine the canard-induced transitions in the case of interacting fast subsystems. In the next section, we present an extended 6D model where an additional secretor system, subject to the forcing of the regulating system, is coupled symmetrically with the other secretor system. We explore how the canard-mediated transitions impact the respective behavior of the secretor systems.

2.3 6D model

$$\begin{aligned}
\varepsilon\delta\dot{x_1} &= -y_1 + f(x_1), \\
\delta\dot{y_1} &= a_0 x_1 + a_1 y_1 + a_2^{(1)} + cX + \alpha_1(x_1 - x_2), \\
\varepsilon\delta\dot{x_2} &= -y_2 + f(x_2), \\
\delta\dot{y_2} &= a_0 x_2 + a_1 y_2 + a_2^{(2)} + cX + \alpha_2(x_2 - x_1), \\
\delta\dot{X} &= -Y + g(X), \\
\dot{Y} &= X + b_1 Y + b_2.
\end{aligned} \tag{2.3.1}$$

The extended model (2.3.1) consists of 2 linearly coupled secretors, S_1 (x_1, y_1) and S_2 (x_2, y_2), subject to the same regulator (X, Y). The resulting system of equations is still a three-timescale model. In this chapter, we always assume that $\varepsilon \ll \delta$. The secretors interact via fast to slow connections, that is to say, the coupling term is a function of the fast variables (x_1, x_2) and acts on the slow variables (y_1, y_2) with the coupling strength $\alpha_i > 0$. The coupling can be considered as a perturbation of the global control signal $X(t)$ received by a secretor with respect to the basic uncoupled situation. The perturbation of slow equations in coupled relaxation cycles is opposed to the general approach where slow-fast systems are coupled via fast to fast connections [33, 50, 34, 71, 43, 72]. We have chosen for simplicity to use a linear coupling in the slow equations. However, the transversality argument we present below applies to any kind of weak coupling.

The existence of canard solutions in coupled systems with folded singularities is not immediate, and proving it analytically is certainly very hard. In Section 2.3.1, we consider a 5D reduction of (2.3.1) near the fold points to examine the existence of canard solutions by taking advantage of a transversality argument that is classical in canard theory: slow manifolds intersect transversally along maximal canard solutions, hence these transversal intersections and associated maximal canards persist for small values of a perturbation parameter, in our case α. Our aim is to emphasize that the coupling can act as a perturbation which separates trajectories with same initial conditions by driving them to different sides of maximal canards. This observation is key to desynchronization as the variables of mutually coupled sub-systems of a nearly synchronous solution are almost equal. In Section 2.3.2, we will come back to model (2.3.1) to explore the effect of coupling on the canard-mediated transitions and consequences on development of the collective dynamics of the two-secretor network.

2.3.1 5D model

The folded singularities of the 4D model have been analyzed in [5]. So far, we have made a general review of this analysis and detailed the dynamical consequences. In this section, we will focus on minimal models of dimension 5 approximating the 6D model near the fold points and investigate the presence of canard solutions in these minimal models. To do so, we consider a minimal 5D model where we replace the periodic forcing of the original model by a constant drift of speed $\mu > \varepsilon$. We simplify the cubic nonlinearity of critical manifolds ($y = \lambda_3 x^3 + \lambda_1 x$) into a quadratic nonlinearity ($y = x^2$) since we want to focus on the dynamics near only one of the fold points. This minimal 5D model takes the following form:

$$\begin{aligned} \varepsilon\dot{x} &= -y + x^2 + \ \dots\ , \\ \dot{y} &= x - z + \alpha(x-u) + \ \dots\ , \\ \varepsilon\dot{u} &= -v + u^2 + \ \dots\ , \\ \dot{v} &= u - z + \alpha(u-x) + \ \dots\ , \\ \dot{z} &= \mu + \ \dots\ , \end{aligned} \tag{2.3.2}$$

where the dots denote higher-order terms in the variables and in ε. In particular, the higher-order terms in the fast equations of the 5D model (2.3.2) include quadratic coupling terms of the form $O(\alpha x u, \alpha u^2)$, which vanish in the limit $\alpha = 0$. System (2.3.2) has 3 slow variables and 2 fast variables. The (x, y) and (u, v) subsystems interact via their fast variables fed to the slow equations with a weak linear coupling term of strength $\alpha > 0$. For $\alpha = 0$, (2.3.2) consists of two identical copies of the minimal folded node system that receives the same input from the common forcing variable z. The critical manifold of system (2.3.2) in this uncoupled limit is the set

$$C^0 = \left\{ (x, y, u, v, z) \in \mathbb{R}^5 |\ y = x^2,\ v = u^2 \right\},$$

and its geometry persists in the small coupling regime. Similarly, the overall fold set of this 5D slow-fast system for $\alpha = 0$ is defined as a product of the fold sets of each individual folded singular system:

$$F = \left\{ (x, y, u, v, z) \in \mathbb{R}^5 |\ xu = 0 \right\}.$$

Note that this fold set is non-degenerate, and that its structure persists for small coupling. In a small neighborhood of F, one can rescale (2.3.2) so that the rescaled system is not singularly perturbed anymore but instead becomes regularly perturbed. To do so, one introduces the following rescaled variables and time:

$$\begin{aligned} x &= \sqrt{\varepsilon}\bar{x} \\ y &= \varepsilon\bar{y} \\ u &= \sqrt{\varepsilon}\bar{u} \\ v &= \varepsilon\bar{v} \\ z &= \sqrt{\varepsilon}\bar{z} \\ t &= \sqrt{\varepsilon}\tau \end{aligned}$$

After dropping the bars, the rescaled system which describes the dynamics in the neighborhood of the folded singularity reads

$$\begin{aligned} x' &= -y + x^2 + \ \dots\ , \\ y' &= x - z + \alpha(x-u) + \ \dots\ , \\ u' &= -v + u^2 + \ \dots\ , \\ v' &= u - z + \alpha(u-x) + \ \dots\ , \\ z' &= \mu + \ \dots\ . \end{aligned} \tag{2.3.3}$$

The rescaled system (2.3.3) is now regularly perturbed in ε. For $\varepsilon = 0$, transversality holds, hence it persists for small positive ε. This way of analyzing slow-fast dynamical systems near a nondegenerate quadratic fold was introduced by Benoît [73]; see also [70]. Moreover, α also appears as a regular perturbation parameter in (2.3.3). Therefore the same persistence argument applies and we can conclude that transversality holds for small enough $\varepsilon > 0$ and $\alpha > 0$. Below, we give more details on the transversality of slow manifolds in the unperturbed system.

The presence of canard solutions in the 5D model for small $\alpha \neq 0$ can be deduced from the 3D (x, y, z)-subsystem (or equivalently (u, v, z)) of (2.3.3) for $\alpha = 0$ using the transversality argument. This 3D minimal system, (x, y, z), possesses a folded-saddle singularity at the origin for $\mu < 0$ and a folded-node singularity for $0 < \mu < 0.125$; therefore, it has two-dimensional attracting and repelling slow manifolds. Transversal intersections of these slow manifolds in the cross-section $\Sigma_\mathrm{f} = \{z = 0\}$, along maximal (e.g. weak, strong and secondary) canards, has been shown in [70], [74] for folded node and folded saddle.

In (2.3.2), the slow manifolds are three-dimensional and their intersections with the cross-section Σ_f are two-dimensional. This cross-section has actually a product structure

$$\Sigma_\mathrm{f} = \Big\{(x, y, u, v, z) \in \mathbb{R}^5 |\ z = 0\Big\} \ = \ \Big\{(x, y) \in \mathbb{R}^2\Big\} \times \Big\{(u, v) \in \mathbb{R}^2\Big\}.$$

For $\alpha = 0$, due to the decoupling, the intersections of the slow manifolds with Σ_f also have a Cartesian product structure. In other words, they can be seen as a Cartesian product of two one-dimensional manifolds. Since transversality is proven in each factor of this product space (by applying classical theory for folded node and folded saddle) for the 3D system, we have transversality in Σ_f. Transversality being a persistent property, the intersections that exist in each factor, and exist globally in Σ_f for $\alpha = 0$, will persist for small $\alpha > 0$. Consequently, this argument is also valid in (2.3.2) for small $\varepsilon > 0$.

In the folded saddle case, the transversal intersections in the coupled 5D system correspond to three different dynamical scenarios when the system passes near the fold of the critical manifold. In the first scenario, both subsystems (x, y, z) and (u, v, z) follow the strong maximal canard. In the second scenario, only one of the two subsystems follow the canard, and none in the third scenario. In the next paragraph, we describe in detail the numerical strategy used to compute the boundary between these different regimes, using the computation of slow manifolds and canard orbits in the 3D subsystems and 5D (un)coupled system. Note that the boundaries in question correspond to the situation where one subsystem follows a maximal canard while the other does not. These two boundaries intersect when both subsystems follow maximal canards, and any trajectory in between corresponds to the third scenario. Our numerical approach to compute these boundaries relies on the numerical continuation of parametrized families of boundary-value problems (BVP) [15]. The software package AUTO, whose algorithms combine numerical continuation with a BVP solver, allows us to find relevant separating orbits (maximal canards) by following one-parameter families of orbit segments with suitable boundary conditions at both ends.

Computation of slow manifolds for coupled systems Computation of the attracting (S_ε^a) and repelling (S_ε^r) slow manifolds requires computing parametrized families of orbit segments which lie along the slow manifolds. The problem can be defined as a boundary value problem where each such orbit segment is chosen so as to have one end point on the critical manifold and the other in a cross-section transverse to the flow near the fold. We consider two-point BVPs of the scaled from

$$\begin{aligned} \dot{\mathbf{s}} &= Tg(\mathbf{s}, \lambda), \\ \mathbf{s}(0) &\in L, \\ \mathbf{s}(1) &\in \Sigma, \end{aligned}$$

where T rescales time so that the solution is computed on the fixed time interval $[0, 1]$, while the actual integration time comes as a parameter that is solved for during the continuation procedure. The smooth function $g : \mathbb{R}^n \times \mathbb{R}^p \to \mathbb{R}^n$ represents the system equations with system variables $\mathbf{s}$. $\lambda \in \mathbb{R}^p$ is the continuation parameter set, and L and Σ are submanifolds of $\mathbb{R}^n$. In a well posed case, the number of boundary conditions should be equal to $n + p$ plus an extra free parameter which is chosen to be T in general. L is chosen to be on the attracting sheet of the critical manifold away from the fold curve to compute S_ε^a and to be on the repelling sheet for S_ε^r, respectively L^a and L^r. Σ is common for both manifolds.

Thanks to the decoupled structure of the model (2.3.3), we start by computing slow manifolds of the 3D minimal folded singularity system in the folded saddle case; we fix $\mu = -0.025$. Detailed description of the process can be found in [15]. Basically, the boundary conditions are imposed as

$$\begin{aligned} \Sigma_f &:= \{(x, y, z) \in \mathbb{R}^3 | z = 0\}, \\ L^a &:= \{y = x^2 \cap \{x = x_a\}\}, \\ L^r &:= \{y = x^2 \cap \{x = x_r\}\}. \end{aligned}$$

Due to the $(x, y, z, t) \to (-x, y, -z, -t)$ symmetry of the minimal system, the repelling slow manifold can be acquired by rotating the attracting one by π about the y-axis. The only intersection point of two-dimensional slow manifolds S_ε^a and S_ε^r on Σ_f satisfies $x_{\Sigma_f} = 0$ and it corresponds to the maximal canard solution near the folded saddle, that is, the strong maximal canard (Fig. 2.7). Using the computed canard solution for the 3D system, we easily obtain a canard solution of the 5D system for $\alpha = 0$ by appending two columns to the computed solution and taking $u = x$ and $v = y$. This orbit segment is a good starting solution for the next step, which consists in computing an approximate canard solution for the 5D system with small $\alpha \neq 0$. This second step can be made by imposing that both subsystems hit section Σ_f at points with the fast coordinate being 0, while allowing the initial z-coordinate to be free. In this way, we obtain a maximal canard solution of the 5D system for a small $\alpha > 0$, which gives the first scenario (canard-canard configuration) mentioned above.

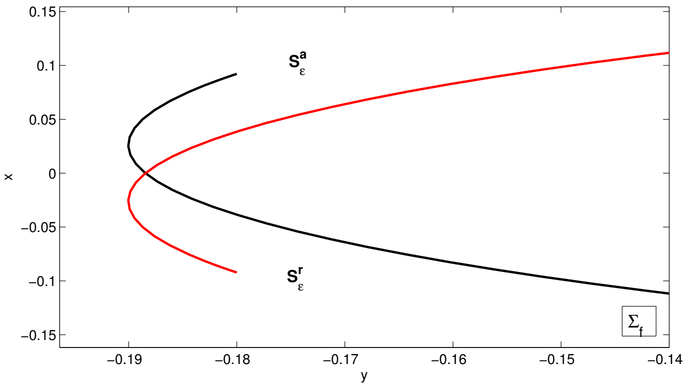

Figure 2.7: Invariant slow manifolds of 3D minimal system with $\mu = -0.025$ obtained for the initial values on the line segments $x_a = -0.2, x_r = 0.2$. Attracting slow manifold S^a_ε (black) and repelling slow manifold S^r_ε (red) intersect transversally on the plane $\Sigma_f := z = 0$ orthogonal to the fold curve at $x_{\Sigma_f} = 0$ which corresponds to the maximal canard solution near the folded saddle.

In the second configuration for $\alpha \neq 0$, one of the subsystems is forced to be on the canard orbit while the other is free. Thus, we start with a canard-canard solution obtained for the small $\alpha > 0$, that is, at the intersection between the boundaries that we wish to compute. Then, freeing the initial condition for one of the subsytems takes it away from the canard orbit while the other one is forced to follow it. This yields the computation of one boundary. For instance, having (x, y) on the canard but not (u, v) requires continuation in $u(0)$ by imposing the starting point on the critical manifold and the end point on $\Sigma_f := \{(x, y, u, v, z) \in \mathbb{R}^5 | z = 0, x = 0\}$ which frees $u(1)$. To find a family of such solutions, one can continue in $z(0)$ in the same setting. Figure 2.8 shows a boundary of different dynamical scenarios. If the system starts on a trajectory which crosses Σ_f on the curves, (x, y) stays on a canard orbit while (u, v) follows a non-canard solution. The intersection point of (u, v) slow manifolds represents the maximal canard solution of (u, v) where both systems undergo canards. Any trajectory that crosses Σ_f outside of these curves corresponds to the solutions where none of the systems follows the canard orbits.

As visualized in Figures 2.8, transversal intersections exist in coupled systems with a folded-saddle singularity. This proves that the 5D minimal model (2.3.2) admits as many canards as the individual folded-node systems as function of μ for $0 < \alpha \ll 1$. That number might change when α is not "small enough" anymore, where more complex and more interesting dynamics can arise. Even though the analysis considers identical systems where fast variables are fed back to slow variables, transversality would persist in non-identical systems of folded singularities coupled in other config-

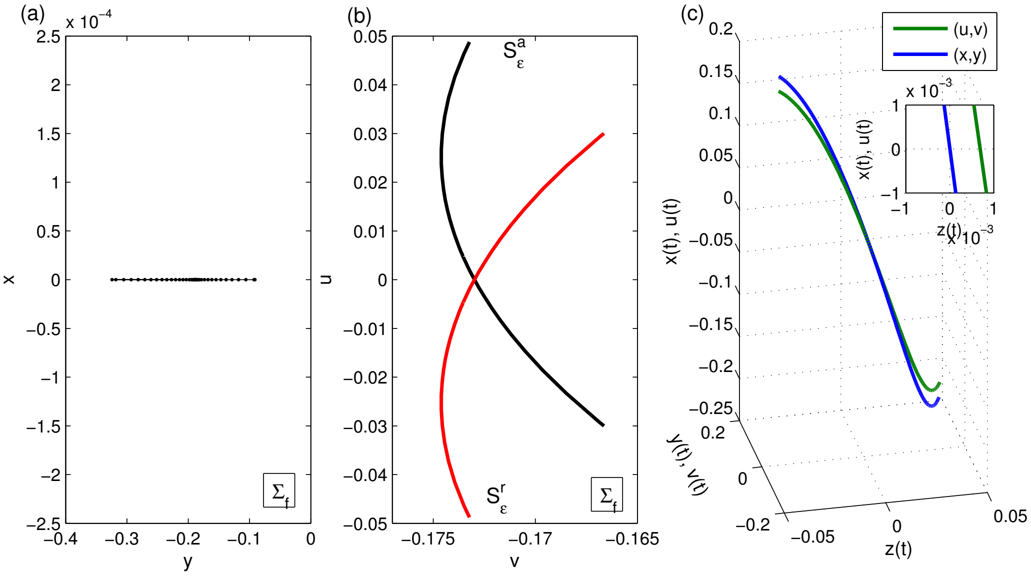

Figure 2.8: Continuation on the configuration where (x, y) subsystem is on the canard and (u, v) is free to move. Panels (a) and (b) are projections of intersection points on the Σ_f plane. (x, y) subsystem intersects $x_{\Sigma_f} = 0$ for the whole set of solutions whereas (u, v) generates non-canard solutions except for the transversal intersection on $u_{\Sigma_f} = 0$. Panel (c) shows an example orbit segment where (x, y) goes though the maximal canard by crossing $(x, z) = (0, 0)$ line while (u, v) does not. Equivalent results can be obtained for the case where (u, v) subsystem is on the canard and (x, y) is free to move.

urations. Hence, our justification and well-posedness of our computation would be valid.

2.3.2 Back to 6D model

The 5D model offers a caricature of the 6D model near each fold. Indeed, in these two regions of phase space, (2.3.1) behaves like two minimal canard oscillators forced by the same external input. Therefore, studying (2.3.2) allows us to explain the existence of canard solutions in (2.3.1) as well as the strong sensitivity to initial conditions, due to the presence of canards, which can lead to desynchronization in coupled identical oscillators. Furthermore, without loss of generality, we can deduce that canard solutions persist also in coupled slightly nonidentical systems and lead to the collective behavior.

As it has been presented for the 4D system, the folded singularities, together with the position of the y-nullcline, generate canard-mediated transitions in the secretors. The interaction via the linear connection from fast to slow variables in (2.3.1) perturbs the y_i-equations, and thus directly affects the evolution of the dynamics near the fold regions. Ensuing canard-mediated transitions might have global or local impacts on the output signal $y_i(t)$ depending on near which fold point they occur. Pre-surge transitions near the lower fold point may have only a local effect on the surge timing (Fig. 2.9). On the other hand, post-surge transitions near the upper fold point may have a relatively global effect; they change both the phase difference in the pulsatile regime and surge timing (Fig. 2.10). Since the periodic behavior of a secretor can be divided into 4 phases, we examine the effects of canard transitions on the evolution of collective dynamics based on these dynamical phases, in particular, during the pulsatile regime (Phase-1) and transition from pulsatility to surge (Phase-2).

In this subsection, we will present examples of recurrent synchronization and desynchronization controlled by canards occurring in (2.3.1). We restrict ourselves to the parameter set in Table 2.2 and vary $a_2^{(i)}$ to distinguish the secretors. First, we will show how the lower fold canards are responsible for desynchronization even in the case of identical secretors. Then, we will continue with coupled nonidentical oscillators where both the upper and lower fold transitions, controlled by the gradual increase in the coupling strengths, result in the decrease or increase in the difference between the oscillators. We believe that the discrepancy between the quantitative features, mostly the respective durations of the surge and pulse regime, and the biological specifications does not alter the generality of the study.

a Coupled identical secretors

Weakly coupled identical non-chaotic oscillators are expected to reach synchronized state in finite time even if they start from different initial conditions [75]. However, canard explosions are very sensitive to slight differences in initial conditions, and divergence of states may give rise to desynchronization by driving solutions to different canard sectors.

To illustrate the effect of folded-saddle canards on the output dynamics, we consider two identical secretors, S_1 and S_2, with $a_2^{(1)} = a_2^{(2)} = 0.7953531$ for which two different

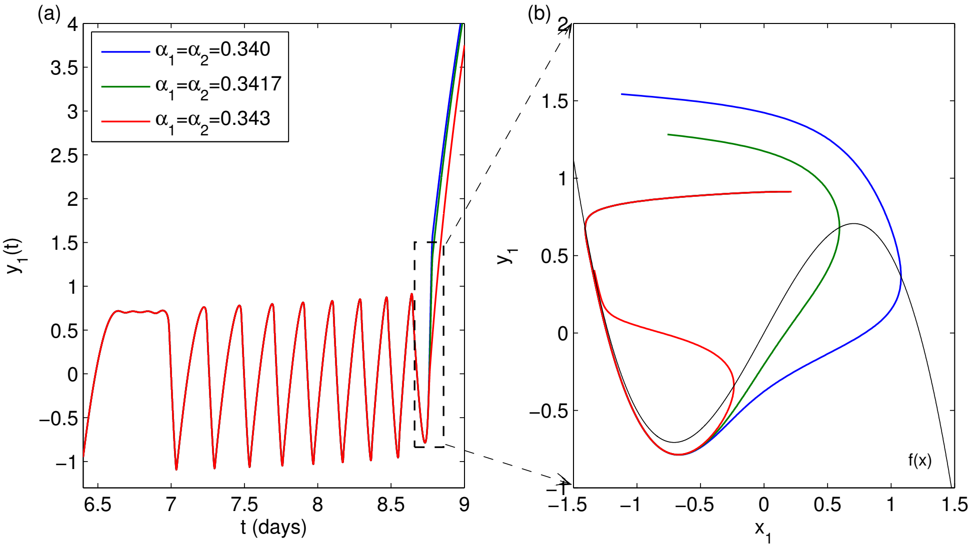

Figure 2.9: A zoom on the possible effect of the canard transition near the lower fold of one of the coupled nonidentical secretors. (a) Time trace of the S_1's output. (b) Pre-surge orbit segment projected onto (x_1, y_1)-plane. Canard transitions near the lower fold have a local effect on the output, specifically, on the pre-surge dynamics. Canards with head are earlier in surge transition than headless canards, thus, a passage from the non-convex region to the convex region introduces a pre-surge delay. Depending on the region from where the other secretor goes to surge, canards may generate or compensate for a great pre-surge ripple in the $(y_1(t) - y_2(t))$ difference.

types of passage through the lower fold appear sequentially before going to the surge; the first is a canard without head and the second is a canard with head. Figure 2.11 illustrates how canard solutions during the pre-surge phase affect the output dynamics by separating nearby orbits. S_1 and S_2 follow opposite sequences, undergo a different type of canard passage at each surge occurrence, so that surge triggering occurs at different moments along the repetition of the sequence. This separation and the resulting pre-surge ripples in the output difference $(y_1(t) - y_2(t))$ persist when the coupling is introduced. Folded-saddle canard solutions continue to preserve the pre-surge desynchronization for an interval of values of the coupling strength $0 < \alpha_1 = \alpha_2 < \alpha_0$ (Fig. 2.12). Strong enough coupling eventually drives the secretors to the same rotation sector and leads to the pre-surge synchronization (or complete synchronization).

b Coupled nonidentical secretors

The linear interaction between slightly nonidentical oscillators via the fast to slow connections controls the behavior near the fold regions depending on the coupling strength. The coupling develops the collective behavior via the canard-mediated transitions near the fold regions. These transitions lead to a decrease or an increase in the difference in the output signals depending on the characteristics of the subsystems. As it will be illustrated by an example, the effect of gradually increasing the coupling strength

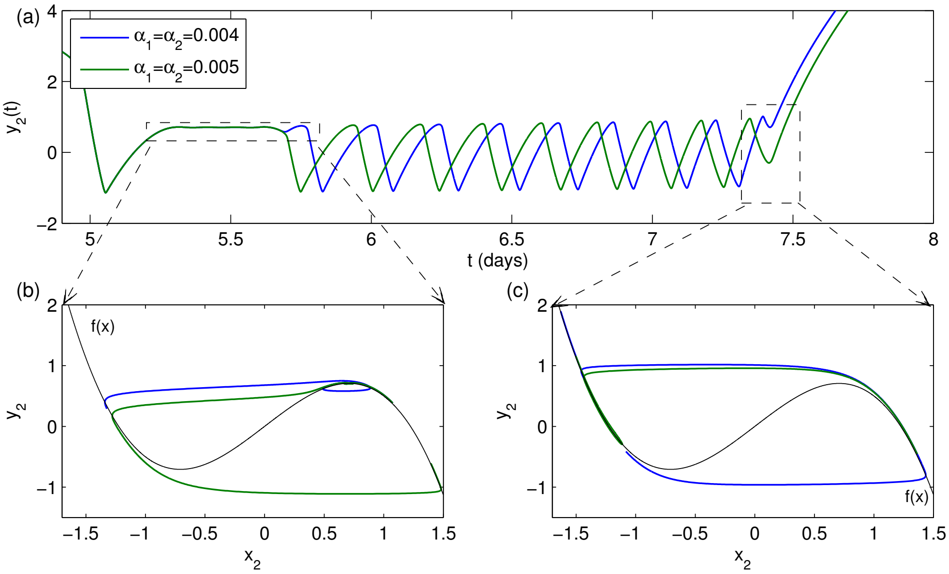

Figure 2.10: A zoom on the possible effects of the canard transition occurring near the upper fold in one of the coupled nonidentical secretors. (a) Time trace of the S_2's output. (b) Post-surge orbit segment projected onto (x_2, y_2)-plane. (c) Pre-surge orbit segment projected onto (x_2, y_2)-plane. Canard transitions near the upper fold have a global effect on the output. For instance, the loss of one SAO from the upper fold changes the timing of the pulsatile regime, affects the phase of the relaxation cycle, changes the number of pulses, and ultimately impacts the surge timing.

on the canard-mediated transitions continues until a threshold value for which the secretors get fully synchronized.

We consider two nonidentical secretors, with a value of parameter $a_2^{(i)}$ of order 1, so that they differ in the number of SAOs (post-surge dynamics), number of pulses and transition to surge (pre-surge dynamics) in the absence of coupling. More specifically, uncoupled S_1 and S_2, with the parameters $a_2^{(1)} = 0.792075, a_2^{(2)} = 0.784$, yield $(8,4)$-type and $(7,5)$-type limit cycles, respectively. As Figure 2.13 illustrates, the difference in the post-surge dynamics causes time shifts the resumption of the relaxation cycles, hence, introduces a phase difference between the pulses. Also, while S_1 departs for surge via a folded-saddle canard, S_2 does not. Regardless of the distinct pre-surge dynamics, the surge is triggered at the same time in both secretors.

The very first effect of coupling is visible on the lower fold passages of S_1 (Fig. 2.14). Slight changes in the coupling strength distort the pre-surge canard solutions of S_1 by shortening the time spent on the unstable branch and forcing the trajectory to jump to the right branch. S_1 undergoes this fast transition for a wide range of $\alpha_1 = \alpha_2 > 0.001$. We will see later on how it comes back to the convex region before surge.

The next effect of increasing coupling strength is observed on the upper fold dynamics of S_2. Initially, S_1 and S_2 exhibit different number of SAOs on the upper fold of the

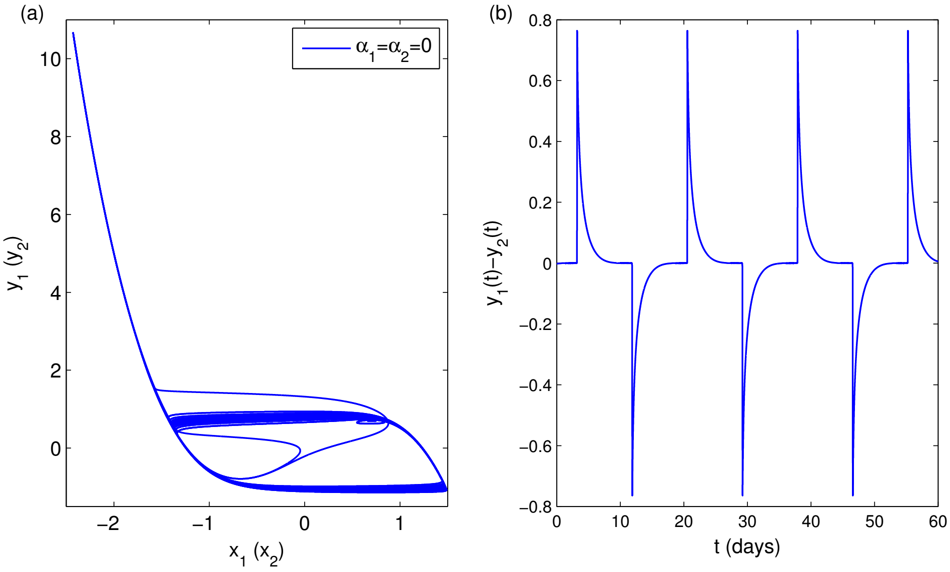

Figure 2.11: Uncoupled identical secretors S_1 and S_2. (a) Projections on (x_i, y_i) planes. (b) Difference in the secretor outputs. Identical systems starting from different initial conditions pass through different canard sectors at each departure to surge, and, consequently, produce ripples in the $(y_1(t) - y_2(t))$ occurring before surge.

critical manifold. The one extra SAO of S_2's post-surge pause causes an obvious phase difference (almost an half-cycle (π) lag) in the pulsatile regime because S_2 resumes its relaxation cycle later than S_1. This difference remains for $0 \leq \alpha_1 = \alpha_2 < 0.005$ and once the coupling strength exceeds a threshold, $(p, s) \to (p+1, s-1)$ transition occurs in S_2 which equalizes the number of SAOs, reduces the phase difference and, eventually, the oscillators cycle with a phase lag less than π (Fig. 2.15). On the other hand, this upper fold transition introduces an explicit difference in the surge departure by giving birth to an additional pulse in S_2. Due to the fact that S_2 departs for surge by following the left branch of $f(x_2)$ whereas S_1 follows the right branch of $f(x_1)$, the surge is triggered later in S_2 than S_1. Consequently, a pre-surge desynchronization is introduced into the collective dynamics.

Further increase in the coupling strength continues to reduce the difference in the upper fold dynamics, hence, phase differences and leads to pre-surge canard-mediated transitions in secretors. For instance, the next transition occurs near the lower fold of S_2 for $\alpha_1 = \alpha_2 \approx 0.08229$ (Fig. 2.16). This $(p, s) \to (p+1, s)$ transition changes the departure region of S_2 from the convex to non-convex one. Alternations between the convex and non-convex solutions appear for $\alpha_1 = \alpha_2 \approx 0.12278$ in S_2 and $\alpha_1 = \alpha_2 \approx 0.3417$ in S_1. The latter drives S_1 to the convex region in the phase space, consequently, both secretors undergo canards without head and reach pre-surge synchronization once more. Further increase in $\alpha_1 = \alpha_2$ does not cause any other transition but decreases the phase differences between the pulses.

Table 2.3 summarizes the impact of canard-mediated transitions driven by the coupling term on the individual and coupled dynamics. Pre-surge transitions have a

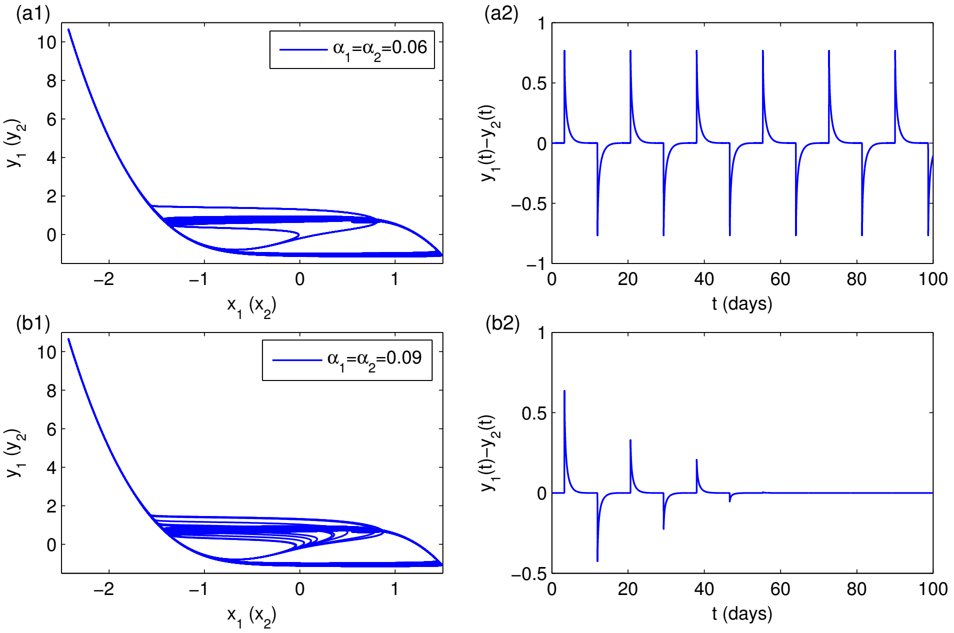

Figure 2.12: Effect of coupling on the canard solutions of identical secretors S_1 and S_2. (a1,b1) Projections on (x_i, y_i) planes. (a2, b2) Difference in the secretors' outputs. Identical secretors starting from different initial conditions preserve the opposite sequential behavior for $0 \leq \alpha_1 = \alpha_2 < 0.0675$, in other words, they desynchronize just before the surge ((a1, a2) $\alpha_1 = \alpha_2 = 0.06$). For strong enough coupling, they synchronize and start to follow the same sequence after a transient response ((b1, b2) $\alpha_1 = \alpha_2 = 0.09$).

local effect on the collective dynamics by changing the surge departure region. We observe that if the secretors are driven to the same family of folded-saddle canards, they reach pre-surge synchronization by departing to surge almost simultaneously. The global effect of the post-surge canards comes from the fact that they both change the phase difference between the pulses and the type of the pre-surge solutions. If the folded-node solutions lie on different rotation sectors, the post-surge transition can change the numbers of SAOs, which affects the pulsatility resumption, hence, the phase difference between the pulses. The impact on the pre-surge solutions is similar to the folded-saddle canards. These observations can be generalized to other combinations of an O(1) or less nonidentical secretors. Further more the transitions can arise simultaneously both in individual level and collective level.

2.3.3 Remark on synchronization studies using the phase resetting curve

Synchronization has been studied extensively in the context of weakly coupled oscillators [51, 76, 65, 77, 50, 48, 60, 52, 72, 49] using the so-called phase resetting curve (PRC) which measures how a change of the phase of one oscillator resets the phase of another one. The derivation of the PRC relies on the linearization of the system along

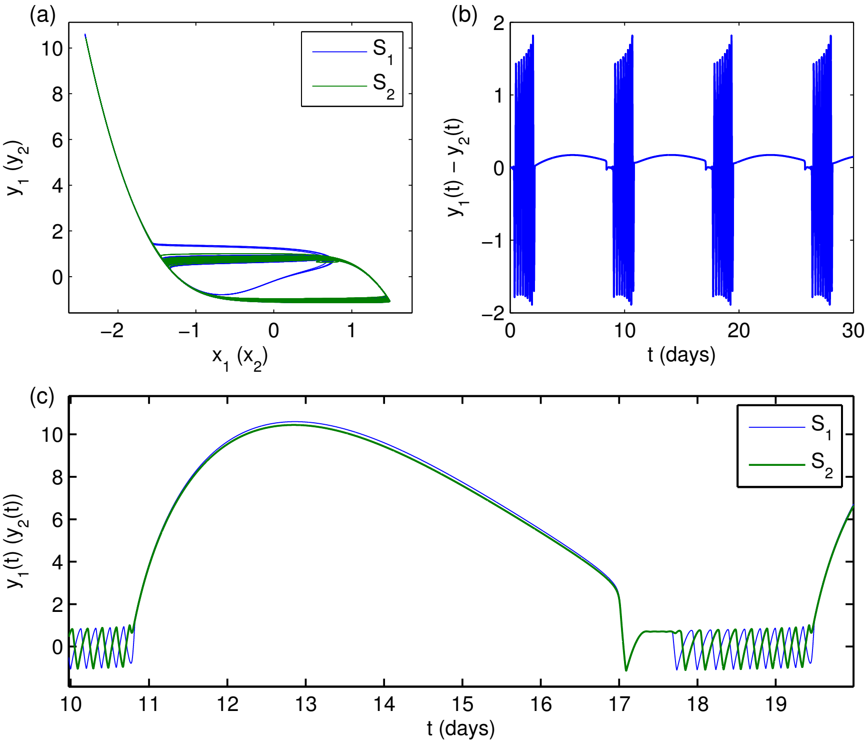

Figure 2.13: Uncoupled nonidentical secretors S_1 and S_2. (a) Phase planes of S_1 (blue line) and S_2 (green line); S_1 remains in the convex region before surge and S_2 moves to the non-convex region. (b) Large amplitude ripples in output difference. (c) S_1 and S_2 resume relaxation cycles at different times and oscillate with and almost π-lag. Anti-phase oscillation compensates for the difference in the surge timing.

Table 2.3: Effects of canard-mediated transitions in (2.3.1) on secretor's individual and collective dynamics.

	Effect on the individual dynamics	Effect on the collective dynamics
Pre-surge canard transitions:	$(p, s) \to (p \pm 1, s)$ transition, surge timing	Pre-surge synchronization/ desynchronization
Post-surge canard transitions:	$(p, s) \to (p \pm 1, s \mp 1)$ transition, pulsatile resumption, surge timing	Change in the phase difference in pulsatile regime, pre-surge synchronization/ desynchronization

the unperturbed (uncoupled) oscillation and makes use of the adjoint equation. In [48, 60] this approach was linked to the work of Malkin [58, 59]. In [60], this approach has been extended to relaxation oscillators and synchronization conditions under the weak coupling, leading to a criterion for the existence of synchronous solutions. The

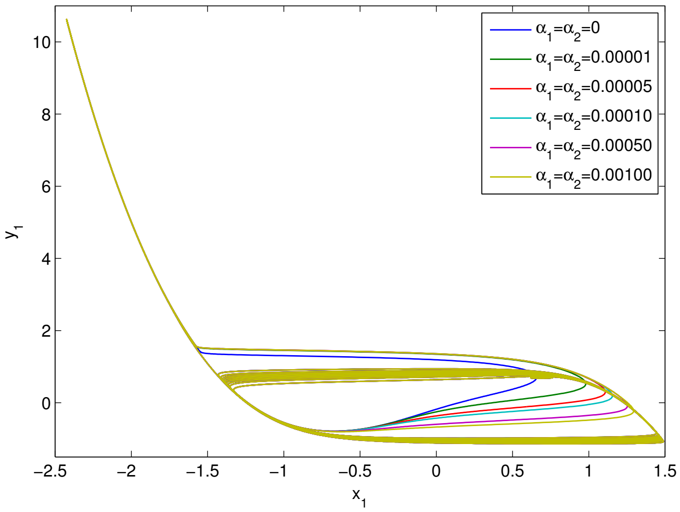

Figure 2.14: Effect of coupling on the canard solutions of S_1 near its lower fold. Slight changes in the coupling strength alter the meeting point between (x_1, y_1) and the y_1-nullcline and force S_1 to undergo, first, canards with head, and then, to jump to the right branch of $y_1 = f(x_1)$.

analysis in [60] relies on the fact that the slow nullcline does not intersect the fast nullcline near fold regions. In the context of weakly coupled FitzHugh-Nagumo oscillators this approach leads to a proof of the existence of a stable synchronous state under the assumption of a fixed slow manifold away from the folds, thus, canard regions. On the contrary, moving the slow nullcline from one fold region to another in (2.3.1) distinguishes our problem on the collective dynamics from that in [60] by several features. Firstly, the passage of the slow nullcline through the singular points of the critical manifold introduces canard solutions. Since the adjoint equation involves a term that vanishes in the canard case, the construction of the solution to the adjoint equation needs to be adapted. Secondly, shifting the slow nullcline increases the cycling frequency, so that a unique cycling period is not definable. Finally, the periodic transition between the surge and pulsatile regime can be considered as a “reset” to phase dynamics of the relaxation cycle in the pulsatile regime, whose duration might be too short to reach a synchronous state. Therefore, it is not possible to comment on the evolution of the synchronization in the coupled secretors (2.3.1) by using classical approaches.

2.4 Discussion

In this chapter, we have studied the effects of canard-mediated transitions in a 6D system, which consists of two fast and one slow FitzHugh-Nagumo oscillators. Our system is an extension of the four-dimensional (4D) model from [1] accounting for the alternating pulse and surge generation in GnRH secretion pattern where the fast subsystems, secretors (the sub-populations of secreting neurons), are modulated by

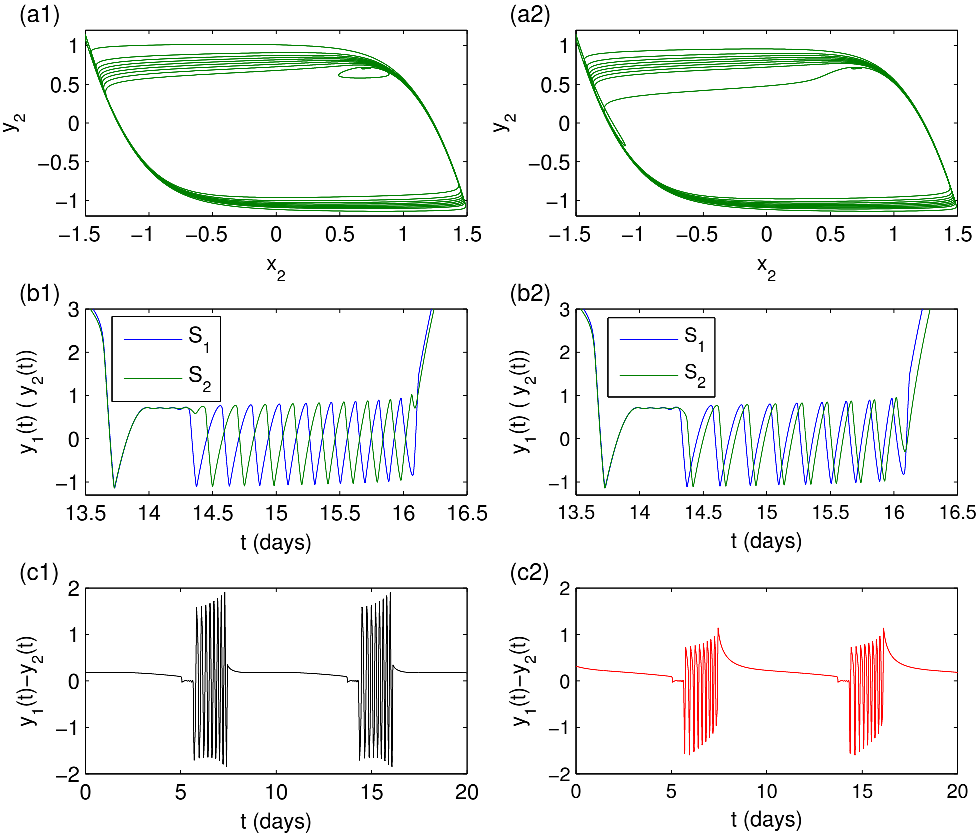

Figure 2.15: Effect of coupling on the canard solutions of S_2 near its upper fold. (a1, a2) Phase plane of S_2 for $\alpha_1 = \alpha_2 = 0.004$ and $\alpha_1 = \alpha_2 = 0.005$, respectively. S_2 loses one small oscillation near the upper fold for $0.004 < \alpha_1 = \alpha_2 < 0.005$. The last SAO of S_2 disappears via a canard trajectory (Panels (a1, a2)) and the number of post-surge SAO of the two secretors are equalized. Both the phase difference and amplitude of the output difference diminish immediately when the SAO is lost (Panels (b1, b2)). On the contrary, pre-surge peaks appear as a result of the different surge timings (Panels (c1, c2)).

the slow subsystem, regulator (the population of regulating neurons). Each secretor-regulator combination can be classified as a phantom burster, hence, the 6D system is interpreted as two coupled phantom bursters sharing the same forcing. The linear interaction between the secretors controls the canard-mediated transitions occurring during different dynamical phases of the GnRH secretion.

We have identified two types of canard-mediated transition in a 4D phantom burster: post-surge transition and pre-surge transition. The former causes a conversion between a SAOs and a pulse whereas the latter affects the last pulse before the surge. In a small range of a control parameter, post and pre-surge transitions occurring sequentially add one more SAO to the post-surge pause. Then, we have proven the

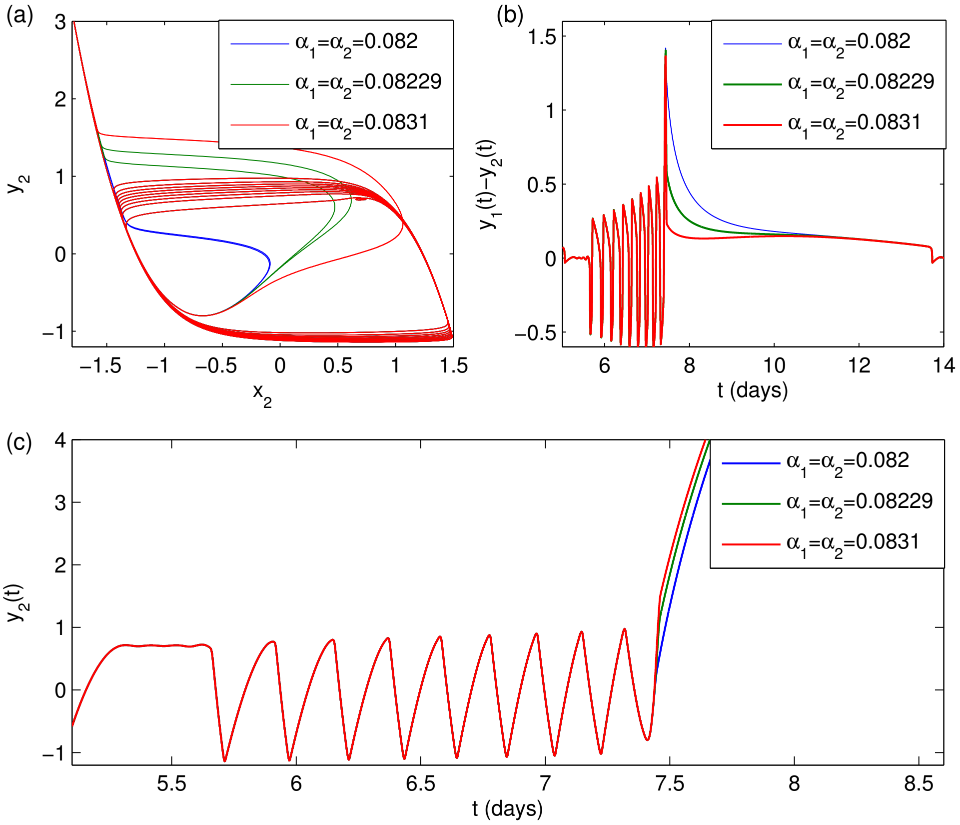

Figure 2.16: Effect of coupling on the canard solutions S_2 near its lower fold. (a) Phase plane of S_2. (b) Difference in the secretors' outputs. (c) Output of S_2 for various coupling strengths. When the number of SAOs is equalized (Fig. 2.15), the increase in the coupling strength make S_2 get closer to the lower fold canard sectors and reduces the phase difference in the pulsatile regime. For $\alpha_1 = \alpha_2 \approx 0.08229$, S_2 undergoes a maximal canard and passes to the non-convex region where S_1 also goes by before surge. This change reduces the pre-surge difference in timing and amplitude.

presence of canard solutions in such coupled slow-fast systems by using a 5D minimal model, which approximates the dynamics in the neighborhood of folds of the critical manifold. We have obtained the existence of canard solutions in a 5D minimal model with non-zero coupling, by using a transversality argument. Then, we have used numerical continuation to show that the coupling drives trajectories of identical systems to different sides of the maximal canard in the folded-saddle case; similar techniques can be used to provide numerical evidence that maximal canards near a folded node also separate nearby trajectories in this 5D minimal model. Extension of our conclusion on the minimal model to the coupled nonidentical systems of folded singularities relies on the transversality argument.

Next, we have investigated numerically the effects of canard-mediated transitions controlled by the coupling term on the collective dynamics of both identical and nonidentical systems. Pre-surge canard transitions introduce or compensate for a separation of the trajectories passing through the lower fold during the transition from pulsatile to surge by changing the departure region. Separation of the departure regions results in pre-surge desynchronization. Post-surge canard transitions tend to decrease the difference in the dynamics of the upper fold by changing the number of SAOs and, consequently, affect both the phase difference in the pulsatile regimes and pre-surge solutions simultaneously. Our observations on the canard-mediated transitions can be generalized to other combinations of at most $O(1)$ nonidentical secretors.

Phase models and their extension to weakly coupled oscillators provide powerful tools to study synchronization. Yet, the slow modulation of the fast variables by the slow ones and the singularity of the adjoint equation introduced by canard solutions remain as open questions. In this context, including higher order terms to the phase models and extending PRC approach to canard case is an interesting question for future work.

In this chapter, we have coupled two sub-populations of GnRH neurons, which do satisfy only the qualitative behavior of the GnRH secretion (as explained earlier, for the sake of numerical continuation, the duration of the pulsatile regime has been shorten), via fast to slow connections. The sub-populations are defined on the macroscopic level that corresponds to the network-emergent character of GnRH secretion encoding on a time horizon of several days. Other models have been interested in the electrical activity of individual GnRH neurons, on the microscopic level (see e.g. [78], on a time horizon of several minutes), or in the coordinated ionic (calcic) activity in tens of neurons, on the mesoscopic scale (see [79] on a time horizon of several hours). We have reported here that small (local) differences in trajectories lying on different sides of a maximal canard can apply $O(1)$ differences in the output, e.g. one secretor produces one more pulse than the other. This could potentially happen where more populations of neurons (GnRH or other types) are coupled in the way we have considered here. In the GnRH framework, repeated events of this type could be at the source of a partial desynchronization before the surge, which has been observed experimentally in time series of portal blood GnRH [80] (and corroborated by the silencing observed in MUA (Multi-Unit Activity) recording as the surge approaches [81]). It is worth noting that the pulses do not really disappear (they are not replaced by a baseline or constant level), so that one might speculate that partial synchronization may persist within distinct subsets of GnRH neurons, which may be formed by underlying canard solutions. In the model we have considered, the number of pulses can vary from one secretor to the other according to possible passages through canard solutions; in another neuronal context, that could be the number of spikes during a burst that could vary from one population to the other, and this discrepancy may carry some level of “information”. As it induces trajectory separations, alternation in the number of MMOs and phase differences, canard-mediated variability gives promising results to address issues on synchronization, desynchronization and clustering dynamics of neural networks.

Chapter 3

Coupled multiple timescale dynamics in populations of endocrine neurons: Pulsatile and surge patterns of GnRH secretion

Elif Köksal Ersöz [1], Alexandre Vidal [2] and Frédérique Clément [1]

Submitted to a peer-reviewed journal

Abstract

The gonadotropin releasing hormone (GnRH) is secreted by hypothalamic neurons into the pituitary portal blood in a pulsatile manner. The alternation between a frequency-modulated pulsatile regime and the ovulatory surge is the hallmark of the GnRH secretion pattern in ovarian cycles of female mammals. In this work, we aim at modeling additional features of the GnRH secretion pattern: the possible occurrence of a two-bump surge ("camel surge") and an episode of partial desynchronization before the surge. We propose a six-dimensional extension of a former four-dimensional model with three timescale and introduce two mutually-coupled, slightly heterogenous GnRH subpopulations (secretors) regulated by the same slow oscillator (regulator). We consider two types of coupling functions between the secretors, including dynamic state-dependent coupling, and we use numerical and analytic tools to characterize the coupling parameter values leading to the generation of a two-bump surge in both coupling cases. We reveal the impact of the slowly varying control exerted by the regulator onto the pulsatile dynamics of the secretors, which leads to dynamic bifurcations and gives rise to desynchronization. To assess the occurrence time of desynchronization during the pulsatile phase, we introduce asymptotic tools based on quasi-static and geometric approaches, as well as analytic tools based on the H-function derived from

---

[1] INRIA Paris Research Centre, MYCENAE Project-Team, 2 Rue Simone Iff, CS 42112, 75589 Paris cedex 12, France.

[2] Laboratoire de Mathématiques et Modélisation d' Évry (LaMME), CNRS UMR 8071, Universit́e d'Évry-Val-d'Essonne, 23 boulevard de France, 91037 Évry, France.

phase equation and numerical tracking of period-doubling bifurcations. We discuss the role of coupling parameters in the two-bump surge generation and the speed of desynchronization.

Keywords

multiple timescale systems, dynamic coupling, GnRH secretion pattern, heterogeneity, synchronization, quasi-stationary approximations, period doubling, interaction function

3.1 Biological and modeling motivation

Endocrine neurons have the uncommon ability of secreting hormones into the blood stream. Neuroendocrine networks are characterized by the emergence of very slow secretion rhythms with remarkable dynamics. The hypothalamic neurohormone GnRH (gonadotropin-releasing hormone) is the master hormone in the hypothalamo-pituitary gonadal axis controlling the reproductive function. GnRH is secreted in a pulsatile manner and the pulsatility has a fundamental role in the differential control of the secretion of both gonadotropins by the pituitary gland: LH (luteinizing hormone) and FSH (follicle stimulating hormone). In females, the pulsatile pattern is tremendously altered once per ovarian cycle into a massive and prolonged release, the GnRH surge, which triggers in turn the LH surge leading to ovulation.

In previous works, we have introduced and studied both qualitatively and quantitatively a compact (four-dimensional (4D)) model with three timescales accounting for the alternating pulse and surge regime as well as for the varying frequency of GnRH pulses [1, 3, 4, 5]. The outputs of this phantom-burster model reproduce the proper sequence of secretory events and meet species-dependent quantitative specifications dealing with the frequency, duration and amplitude of these events.

The modeling motivation underlying the current work comes from additional features observed experimentally in the secretion pattern of GnRH. When looking finely at GnRH time series sampled from the pituitary portal blood (the most, not to say unique, reliable marker of the neurosecretory activity of the GnRH network), one can see that, on the one hand, the surge may in some cases be composed of two main bumps (instead of a single) [82, 83, 84, 85, 86], and on the other hand, the increase in GnRH pulse frequency at the end of the follicular phase, that is inseparable from the ability of the network to mount a GnRH surge, is accompanied at the very end of the follicular phase by a degradation in pulsatility and appearance of noise that blurs the GnRH pulses [80]. Another witness of desynchronization within the GnRH network as the surge approaches is the silencing observed in recordings of MUA (Multi-Unit Activity), a macroscopic marker of electric activity at the level of the median eminence that is otherwise well correlated with GnRH-induced LH pulses [87]. Interestingly, in case of a 2-bump surge (which we will refer as “camel surge” from now on), the first bump coincides with the LH ovulatory surge, while the second bump corresponds to the part of the surge that extends much beyond the duration of the LH surge [88, 89] and whose biological signification is unclear, even if it seems to be involved in estrous behavior in some species [90, 91].

In Chapter 2, we have proposed a 6-dimensional (6D) extension of the original 4D system, by adding a second secretory system interacting with the first one, and subject to the same forcing from the regulating system. We have thus introduced a first level of heterogeneity within the GnRH population, by considering two distinct subpopulations. We tackled the question of synchronization between the secretory systems from the dynamical viewpoint, to study the impact of coupling on the slow-fast transitions arising in the fast subsystems. Yet, we considered a simple coupling function and departed from the quantitative properties of the model, even if its qualitative sequential behavior was preserved. In contrast, in the current study, we intend to adapt such an extended 6D model to manage to reproduce the additional GnRH secretion features without altering any of the quantitative features of the model output. As a consequence, we focus our attention on the proper formulation of the coupling function with respect to the desired outputs, which results in a complicated model with both asymmetric and dynamic coupling terms. We also investigate how to control quantitatively the newly added features: timing, ordering and amplitude of the surge bumps, as well as time occurrence of desynchronization.

The collective dynamics of slow-fast oscillators coupled on different timescales have a great importance in the context of physiology when microscopic and macroscopic levels can be represented with similar dynamics, especially in excitable systems for neuronal activity [33, 49]. Such dynamics result naturally from the mass modeling approach, that consists in focusing on the average behavior of neuron assemblies considered to behave jointly. Using this paradigm, the specific features of the individual cells' activities, and the microscopic dynamic interactions are no longer taken into account. Yet, a large panel of dynamic behaviors can be generated by such models, even if they are designed to reproduce activities at the mesoscopic scale. Therefore, the identification of the main mechanisms involved in the synchronization of complex oscillations (for instance bursting oscillations [34, 35, 36, 37, 38]) and the robustness of the synchronization features are key points for the analysis of neural population activities.

Extensive efforts have been dedicated to the understanding of synchronization in slow-fast systems in the context of neuroscience and have led to the development of theoretical and numerical tools, such as the fast threshold modulation theory [43], singular perturbation methods [44, 45, 46, 47], theory of weakly coupled oscillators and phase response curves (PRC) [72, 50, 51, 52, 54, 33, 48, 49]. The weakly coupled oscillator theory has been extended to relaxation cycles in [60]. The questions mainly tackled in the framework of synchronization in neural systems are the effects of intrinsic properties, slowly varying terms, heterogeneity [53, 57, 61, 55, 56, 92, 93] and the derivation of analytic expressions for PRCs [62, 63, 64].

This chapter is organized as follows: In Section 2, we consider a biologically relevant secretion pattern generated by the 4D GnRH secretion model (1.1.1) and we reformulate the 6D extended model introduced in Chapter 2. We introduce more elaborate coupling functions. In Section 3, we perform quantitative studies based on numerical simulations and analytic expressions to derive information on the parameter set compatible with a camel surge. In Section 4, we introduce asymptotic approaches to investigate the occurrence of a desynchronization episode in the pulsatile regime and assess the chronology of desynchronization. In Section 5, we apply our results to mimic specific experimental instances of a camel surge. In Section 6, using numerical continuation, we discuss the possible mechanisms underlying desynchronization in the framework of weakly coupled oscillators theory. A final conclusion and discussion are provided in Section 7.

3.2 GnRH secretion model and subpopulation

3.2.1 Review of the 4D GnRH secretion model

In Chapter 2, we have reviewed the general pattern of the 4D model (1.1.1) with a parameter set respecting only the qualitative features of the GnRH secretion. In [3], constraints on the parameters were obtained from dynamical principles to guarantee not only the proper qualitative sequence of secretory events, but also quantitative features subject to biological specifications and dealing with the duration, amplitude and frequency of the GnRH signal. Since, in this chapter, we rather focus quantitative features needed to meet biological specifications, we prefer to consider the model output as following:

$$y^{out}(t) = y(t)\chi_{\{y(t)>y_{TH}\}}, \tag{3.2.1}$$

χ_A being the indicator function ($\chi = 1$ on A, 0 elsewhere). This thresholded solution component $y^{out}(t)$ corresponds to the amount of secreted GnRH. Figure 3.1 shows the output (3.2.1) profile of (1.1.1) obtained by using a parameter set given in [3] respecting the secretion pattern in the ovine species, whereas Figure 1.1 shows the qualitative profile.

One of the salient features of system (1.1.1), which plays a critical role in the current framework, is the frequency increase occurring during the pulsatile regime. This increase ensues from the changing location of the unstable stationary point lying on the middle branch of $f(x)$. At the beginning of the pulsatile regime, this point is close to the upper fold of $f(x)$. As a consequence, the current point (x, y) running on the limit cycle is slowed down in the vicinity of the stationary point, hence the period of the cycle is rather long (this low frequency pattern corresponds to the so-called luteal phase of the ovarian cycle). As X increases, the y-nullcline moves leftwards, so that the stationary point moves away from the right fold; the current point escapes from the influence of the stationary point and the period gets smaller and smaller, up to the surge triggering (this high frequency pattern corresponds to the so-called follicular phase of the ovarian cycle).

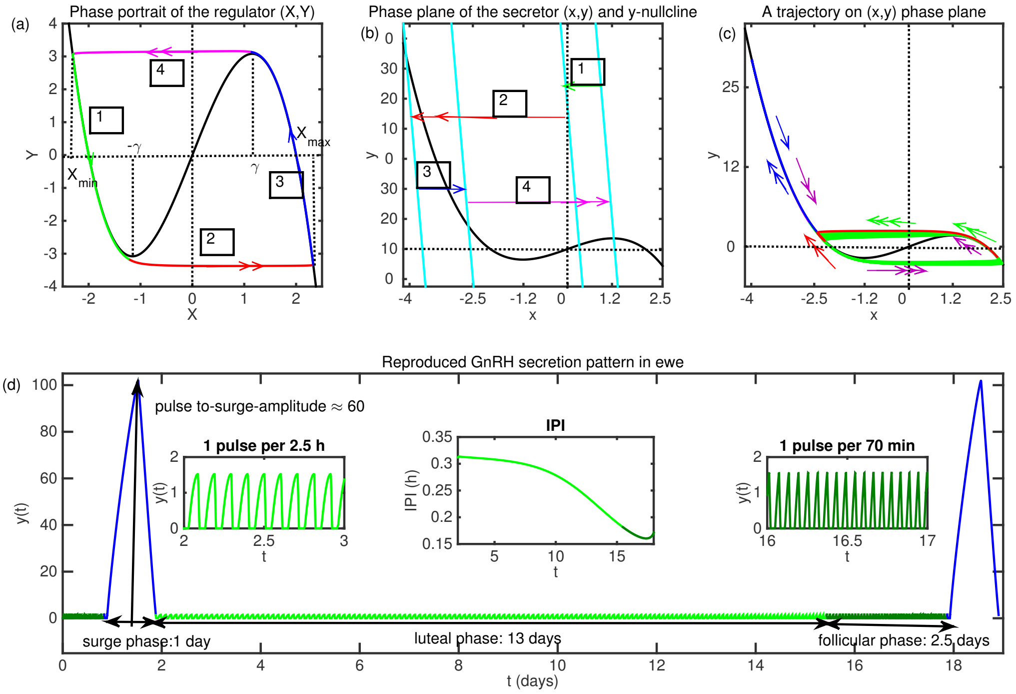

Figure 3.1: Phase-dependent dynamic behavior and reproduction of the GnRH secretion pattern. Panel (a): attracting relaxation cycle followed by the regulator in the (X, Y) phase plane. The abscissas of the upper and lower fold points of the cubic nullcline are labeled as γ and $-\gamma$, respectively. Each number represents a different phase of the periodic behavior. 2-headed arrows: $O(\varepsilon)$ speed, 1-headed arrows: $O(1)$ speed. Panel (b): position of the nullclines of the secretor on the (x, y) phase plane with respect to the 4 phases in the (X, Y) limit cycle. Green arrow: direction of the y-nullcline during the pulsatile phase. Red arrows: transition from pulsatility to surge. Blue arrow: surge phase. Pink arrows: transition from surge to pulsatility. The leftwards motion of the y-nullcline during the pulsatile phase results in an increasing pulse frequency. The increase in the pulse frequency is emphasized by the decrease in the interpulse interval (IPI), as seen on the middle inset of Panel (d). Panel (c): projection of a trajectory onto the (x, y) plane. The phases are colored as in Panel (a). 3-headed arrows: $O(\varepsilon\delta)$-speed motion. Panel (d): GnRH pattern along the ovarian cycle using the same color code to highlight the different phases (the fastest transitions are embedded within the surge phase). The quantitative specifications were derived for the ovine species. Whole cycle duration: 16.5 days. Luteal phase duration: 13 days. Follicular phase duration (surge excluded): 2.5 days. Surge duration: 1 day. Pulse to surge amplitude ratio: 1/60. Frequency increase ratio: 1/4.

3.2.2 Introduction of a generic 6D model

To be more generic, we prefer to re-write the 6D model given in (1.4.1) in a more general form as follows:

$$\varepsilon\delta\dot{x}_1 = -y_1 + f(x_1), \tag{3.2.2a}$$

$$\delta\dot{y}_1 = a_0^{(1)}x_1 + a_1^{(1)}y_1 + V^{(1)}(x_1, x_2, y_1, y_2, X, Y), \tag{3.2.2b}$$

$$\varepsilon\delta\dot{x}_2 = -y_2 + f(x_2), \tag{3.2.2c}$$

$$\delta\dot{y}_2 = a_0^{(2)}x_2 + a_1^{(2)}y_2 + V^{(2)}(x_1, x_2, y_1, y_2, X, Y), \tag{3.2.2d}$$

$$\delta\dot{X} = -Y + g(X), \tag{3.2.2e}$$

$$\dot{Y} = b_0X + b_1Y + b_2, \tag{3.2.2f}$$

and

$$y_1^{out}(t) = y_1(t)\chi_{\{y_1(t)>y_{TH}\}}, \tag{3.2.3a}$$

$$y_2^{out}(t) = y_2(t)\chi_{\{y_2(t)>y_{TH}\}}, \tag{3.2.3b}$$

$$z(t) = y_1^{out}(t) + y_2^{out}(t). \tag{3.2.3c}$$

We will refer to subsystems (3.2.2a)-(3.2.2b) and (3.2.2c)-(3.2.2d) as Secretor 1 and 2 (S_1 and S_2), respectively. The global output of the model is $z(t)$ given by (3.2.3c) as the sum of thresholded $y_1(t)$ and $y_2(t)$ signals in (3.2.3a) and (3.2.3b), respectively. The coupling in (3.2.2b) and (3.2.2d) can be considered as a modulation of the secretor sensitivity to the control exerted by the regulator. The nonidentical $V^{(i)}$ functions read:

$$V^{(1)}(x_1, x_2, y_1, y_2, X, Y) = a_2^{(1)} + c^{(1)}X + I^{(1)}(x_1, x_2, y_1, y_2, X)$$
$$V^{(2)}(x_1, x_2, y_1, y_2, X, Y) = a_2^{(2)} + c^{(2)}X + I^{(2)}(x_1, x_2, y_1, y_2, X)$$

where the mutual interaction between the secretors is provided via the coupling functions $I^{(1)}$ and $I^{(2)}$.

Table 3.1: Nominal parameter values of the 6D GnRH secretion model (3.2.2) used for the numerical simulations. In this study, we consider $a_0^{(1)} = a_0^{(2)} = a_0$, $a_1^{(1)} = a_1^{(2)} = a_1$ and $y_{TH} = 1.4$.

$a_0 = 0.52$	$a_1 = 0.011$
$a_2^{(1)} = 0.7$	$a_2^{(2)} = 1.14$
$c^{(1)} = 0.5113$	$c^{(2)} = 0.70012$
$b_1 = 0.246$	$b_2 = 1.5103$
$\lambda_3 = -1$	$\lambda_1 = 2.5$
$\mu_3 = -1$	$\mu_1 = 4$
$\delta = 0.02$	$\varepsilon = 0.0125$

Figure 3.2 shows signals $y_1(t)$ and $y_2(t)$ with the parameter set in Table 3.1, in the absence of mutual interaction between the secretors, i.e. $I^{(1)} \equiv I^{(2)} \equiv 0$. Since both

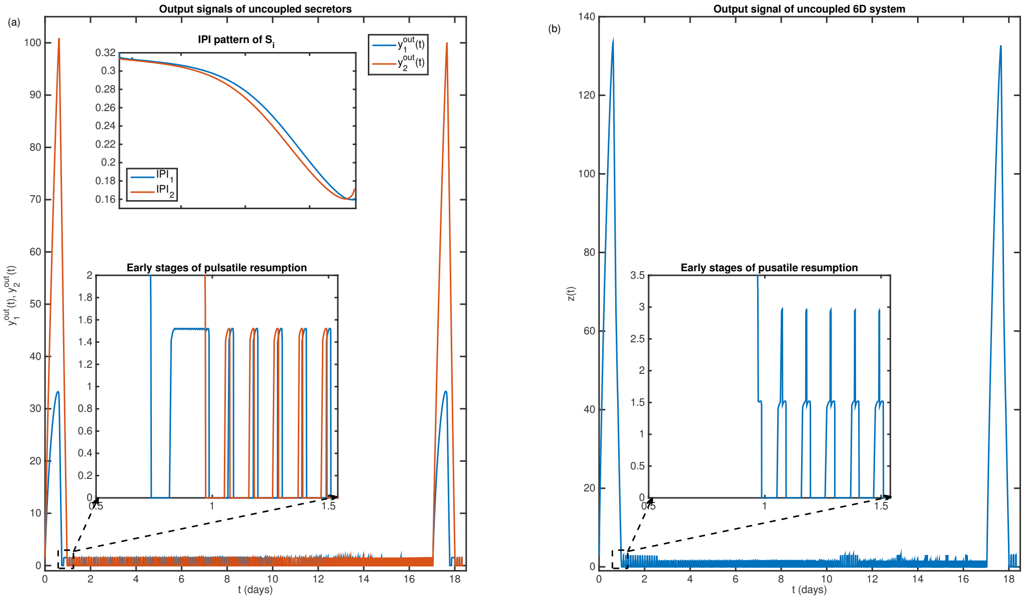

Figure 3.2: Panel (a): signals $y_1^{out}(t)$ (blue) and $y_2^{out}(t)$ (red) in the absence of coupling. The differences in the IPI_i patterns (upper inner panel), surge amplitudes and the presence of a pause before pulsatility resumption in S_1 (lower inner panel) are visible. Panel (b): global output $z(t)$ of the uncoupled system. The pause in S_1 is embedded within the whole duration of the surge in S_2 and contributes to the global surge (inner panel).

secretors are controlled by the same regulatory signal, $X(t)$, they share the same duration for the pulsatile and surge regimes, yet, due to the heterogeneity in the parameter values, there exist differences in (i) the pulse frequency, (ii) the surge amplitude and (iii) the way to resume pulses after the surge, with S_1 exhibiting a pause while S_2 does not. The pause in S_1 contributes to the global surge pattern visible in the right panel of Figure 3.2, yet it does not interfere with neither the global features of the coupled system behavior nor our analysis. In contrast, the difference in frequency is essential for the blurring of pulses while the difference in surge amplitude is needed to obtain a camel surge.

Difference in the pulsatile regime The shift in the location of the unstable nodes on the middle branches of the x_i-nullclines ($i \in \{1,2\}$) results in different pulse frequencies hence, IPI_i patterns. Such a difference, together with the formulation of $z(t)$ in (3.2.3c), leads to a variation in the pulse amplitudes.

In the uncoupled situation, the times of pulse onset, $t_i^{(n)}$ (where n stands for the n-th pulse occurring since the latest surge in $z(t)$), are given by $y_i(t_i^{(n)}) = y_{TH}$, $x_i(t_i^{(n)}) > 0$, while the times of pulse ending, $t_i^{(*n)}$, are such that $y_i(t_i^{(*n)}) = y_{TH}$, $x_i(t_i^{(*n)}) < 0$. The pulse width is obtained from the delay between the onset and ending times, $t_{pulse,i}^n = t_i^{(*n)} - t_i^{(n)}$. The series of IPI_i is the sequence of consecutive times of pulse

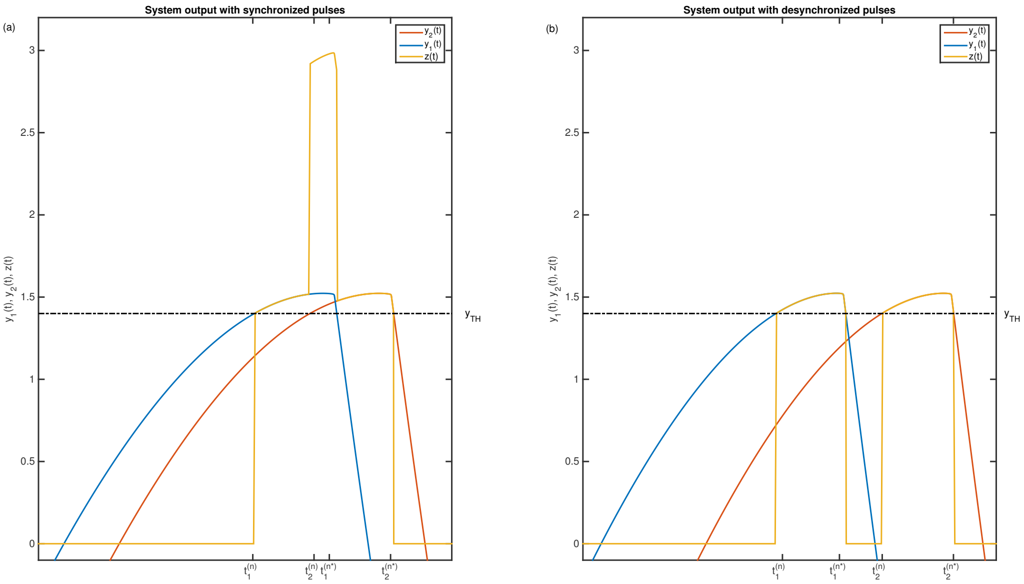

Figure 3.3: Output signals generated by the 6D model : $y_1(t)$ (blue curve), $y_2(t)$ (red curve), global output $z(t)$ (yellow curve), compared to y_{TH} (black dashed line). Panel (a): overlapping pulses in $y_1(t)$ and $y_2(t)$ leading to a synchronized pulse $z(t)$, with $z(t) > 2y_{TH}$ ($t_2^{(n)} \in [t_1^{(n)}, t_1^{(*n)}]$). Panel (b): separated pulses in $y_1(t)$ and $y_2(t)$ leading to desynchronized pulses in $z(t)$, with $z(t) < 2y_{TH}$ ($t_2^{(n)} \notin [t_1^{(n)}, t_1^{(*n)}]$).

onset $IPI_i^{(n)} = t_i^{(n+1)} - t_i^{(n)}$.

In the coupled case, the widths of the closest pulses generated by S_1 and S_2 can be more or less overlapping, and the level of overlapping can be assessed by the difference between the closest onset times in each secretor $t_j^{(n)} - t_i^{(n)}$ ($j = 3 - i$).

A shift in the onset times is compatible with a long enough overlapping episode and a $z(t)$-generated pulse as long as $z(t) > 2y_{TH}$. More precisely, let us assume that the n-th pulse of S_1 starts before the n-th pulse of S_2 so that $t_1^{(n)} < t_2^{(n)}$. If $t_2^{(n)}$ lies in the interval $[t_1^{(n)}, t_1^{(*n)}]$, there is a time window during which both signals exceed the y_{TH} threshold, so that an *overlapped pulse* appears in $z(t)$ (Figure 3.3-a). In contrast, when $t_2^{(n)}$ occurs after y_1 is back below the threshold, then a *separated pulse* appears (Figure 3.3-b).

Since the IPI$_i$ and width of pulses change during the pulsatile regime in each secretor, the occurrence of overlapped pulses results from an interplay between the mutual coupling and intrinsic properties of the secretors. We will refer to the overlapped pulses as "synchronized" pulses associated with episodes of *synchronization*

$$z_{sync}(t) = z(t)\chi_{\{(y_1^{out}+y_2^{out})>2y_{TH}\}}. \tag{3.2.5}$$

Similarly, separated pulses will be referred as "desynchronized" pulses associated with *desynchronization* in the global output

$$z_{desync}(t) = z(t)\chi_{\{(y_1^{out}+y_2^{out})<2y_{TH}\}}.$$

Difference in the surge regime: With the nominal parameter values, the location of the y_2-nullcline with respect to $f(x_2)$ is leftmost compared to the relative positions of the y_1-nullcline and $f(x_1)$. As a consequence, the surge amplitude in S_1 is lower than in S_2. In the presence of a suitable coupling, this initial difference affects the surge shaping.

In the next section we describe different appropriate forms of $V^{(i)}$ to reproduce a camel surge.

3.2.3 Choice of the coupling for reproducing a camel surge

To reproduce a camel surge, we implement functions of $V^{(i)}$ and $I^{(i)}$ in (3.2.4) as:

$$\begin{aligned} V^{(1)}(x_1,x_2,y_1,y_2,X,Y) &= a_2^{(1)} + c^{(1)}X + \alpha^{(1)}(x_1,y_1)(x_1-x_2)\psi(X_{sync},X) \\ V^{(2)}(x_1,x_2,y_1,y_2,X,Y) &= a_2^{(2)} + c^{(2)}X + \alpha^{(2)}(x_2,y_2)(x_2-x_1)\psi(X_{sync},X) \end{aligned}$$

where $\psi(X_{sync},X)$ is an *activation function* and X_{sync} a threshold parameter, such that the coupling is active if $X \leq X_{sync}$ and inactive otherwise. On a practical ground, we will use a sigmoid function with a stiff enough slope (typically $\rho = 30$), rather than a Heaviside function:

$$\psi(X - X_{sync}) = \frac{1}{1+\exp(\rho(X - X_{sync}))} \tag{3.2.7}$$

Functions $V^{(i)}$ combine coupling and heterogeneity terms. The heterogeneity in $V^{(i)}$ comes from the differences in the intrinsic parameters $a_2^{(i)}$ and $c^{(i)}$, as well as the asymmetric nonnegative coupling strengths $\alpha^{(i)}(x,y)$ in which the fast variables (x_1,x_2) act on the slow variables (y_1,y_2). In the sequel, we will consider two cases for $\alpha^{(i)}(x,y)$: constant functions (*constant coupling* case) and y_i^{out}-dependent functions (*dynamic coupling* case). Our motivation to consider different coupling functions, and especially to introduce a dynamic coupling, is to avoid the use of strong coupling strengths while managing to reproduce both the camel surge and the desynchronization at the end of the pulsatile regime.

a Constant coupling

With $\alpha^{(i)}(x,y) \equiv \alpha$, the coupling terms in $V^{(i)}$ read

$$\alpha^{(i)}(x_i,y_i)(x_i-x_j)\psi(X - X_{sync}) = \alpha(x_i-x_j)\frac{1}{1+\exp(\rho(X - X_{sync}))}. \tag{3.2.8}$$

Choosing a value of X_{sync} such that the point $(X_{sync}, g(X_{sync}))$ lies on the middle of the right branch of $g(X)$ (see Figure 3.4(a1, a2)) leads to a deactivation of the coupling function during the first part of the surge, as long as $X(t) > X_{sync}$. If the difference between the parameters of the secretors is sufficient, the 4-phased behavior of secretors interacting via (3.2.8) can be summarized in the following way:

1. *Pulsatile regime* $X(t) < 0 < X_{sync}$ The coupling is active, S_1 and S_2 stay synchronized for either the whole pulsatile regime, or a part of it, depending on the parameter values of S_1 and S_2 and the coupling strengths in (3.2.8).

2. *Surge triggering* $X(t)$ increases rapidly and overcomes X_{sync}, which deactivates the coupling. S_1 and S_2 follow their motion along the left branches of $f(x_1)$ and $f(x_2)$ independently.

3. *Surge regime* In the first part of the surge, as long as $X_{max} > X(t) > X_{sync}$, $X(t)$ decreases slowly, S_1 and S_2 move along the left branch of $f(x_1)$ and $f(x_2)$, respectively. In the second part of the surge, the coupling is activated as long as $X_{sync} > X(t) > \gamma$, the secretors get closer to each other as variable y_i decreases in the secretor with greater amplitude while it increases in the other.
   If this two-part regime generates a non-monotonic pattern in $z(t)$, with an initial increase followed by a decrease, a camel surge is obtained (see for instance, the curves corresponding to $X_{sync} = \{1.8, 1.9, 2\}$ in Figure 3.4(b), and further explanations in Section 3).

4. *Resumption of pulsatility* $X(t)$ decreases rapidly and triggers the descending parts of the surges followed by the resumption of pulses.

b Dynamic coupling

The coupling term with an alternative coupling function reads:

$$\alpha^{(i)}(x_i, y_i)(x_i - x_j)\psi(X - X_{sync}) = \hat{\alpha}_i\, y_i^{out}(x_i - x_j)\frac{1}{1 + \exp(\rho(X - X_{sync}))} \tag{3.2.9}$$

where the coupling strength $\hat{\alpha}_i$ is multiplied by the output signal $y_i^{out}(t)$. In this case, the coupling depends on the state of the system not only during the surge, but also during the pulsatile regime; it is active when both $X(t) < X_{sync}$ and $y_i(t) > y_{TH}$.

With the dynamic coupling function (3.2.9), synchronization in the pulsatile regime (which is not guaranteed) occurs in the following way: Assume that (x_1, y_1) and (x_2, y_2) are lying respectively on the right branch of $f(x_1)$ and $f(x_2)$, with and S_1 ahead of S_2. The dynamics of S_1 starts to be influenced by S_2 when $y_1(t) \geq y_{TH}$. At that time S_1 is slowed down by the coupling since $\hat{\alpha}_1\, y_1^{out}(x_1 - x_2) < 0$. Meanwhile, y_2 continues to climb up along $f(x_2)$ without being affected by S_1, until it reaches y_{TH}. If y_1 is still high enough and $y_1^{out}(t) > 0$ when $y_2(t) \geq y_{TH}$, then the pulses of S_1 and S_2 overlap, and the systems are synchronized.

During the surge phase, a similar principle as for the constant coupling operates, where the activation of the coupling with $X(t) < X_{sync}$ tends to reduce the differences between the secreting systems. As in the example in Figure 3.5, camel surge can be obtained with dynamic coupling function.

The main difference between constant and dynamic coupling lies in the values of the coupling strengths needed to obtain a camel surge. The constant coupling requires really strong coupling strengths, such that $|\alpha_i| > |y_i(t)|$, which may be questionable both from the biological and mathematical viewpoints. In the next section we investigate

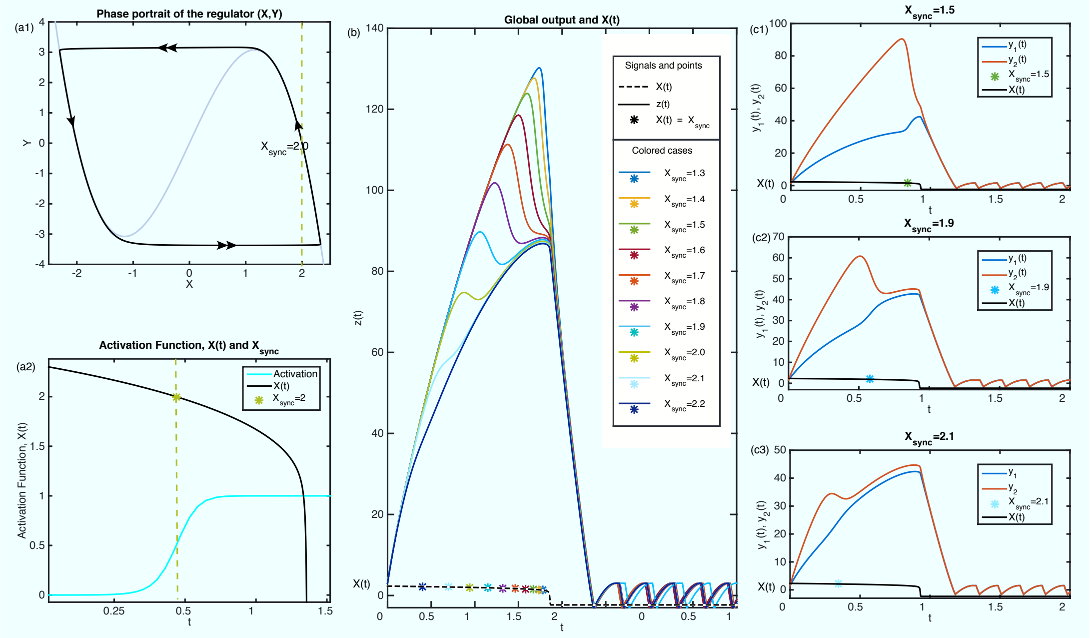

Figure 3.4: Activation function $\psi(X_{sync}, X)$ in (3.2.7) and shaping of a camel surge using constant coupling function (3.2.8) with $\alpha_1 = 2$ and $\alpha_2 = 10$. Panel (a1) Location of the activation value $X_{sync} = 2$ on the (X, Y) plane. The coordinate $(X_{sync}, g(X_{sync}))$ is located on the middle of the right branch of $g(X)$. Panel (a2) Activation signal as a function of time ($X_{sync} = 2$), with initial time chosen at the very beginning of the surge, and change in $X(t)$ starting from its maximal value $X = X_{max}$ and decreasing progressively to reach X_{sync} during the surge. Panel (b) Global output $z(t)$ during the surge according to different values of X_{sync}. Panels (c1-c3) Signals $y_i(t)$ generated with three different values of X_{sync} (1.5, 1.9, 2.1).

the efficiency of both coupling formulations in the surge regime, where $|\alpha_i| < |y_i(t)|$, to obtain a camel surge. In Sections 4 and 6, we will focus on the desynchronization time within the pulsatile regime, in either the constant or dynamic coupling case. In Section 5, we will consider jointly the issues of camel surge and desynchronization, and give instances of application of our results within an experimental context.

3.3 Quantitative analysis of the camel surge: constraints on the coupling terms

In the previous section, we have shown that the camel surge can be reproduced by means of two different X-dependent coupling functions. Here, we derive quantitative information on the sets of parameter values compatible with the appearance of a camel surge, as well as on the parameter-dependent surge shaping.

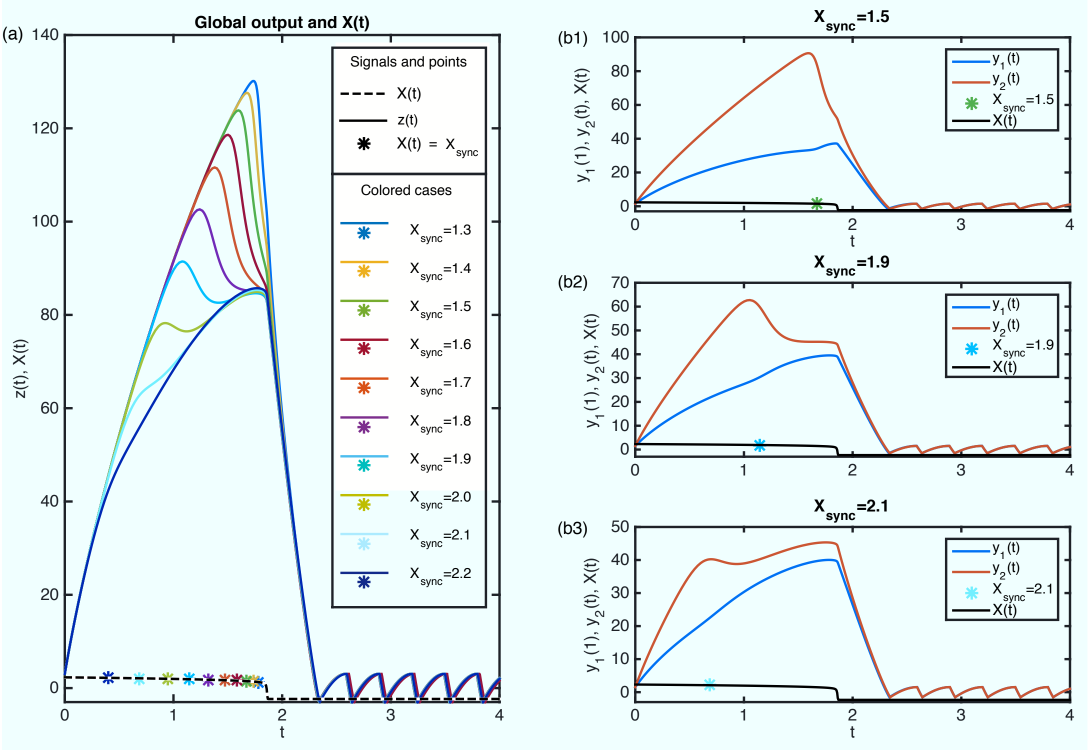

Figure 3.5: Generation of a camel surge with dynamic coupling (3.2.9) for $\hat{\alpha_1} = 0.02, \hat{\alpha_2} = 0.1$. Panel (a): the value of X_{sync} should be chosen in the correct range to let S_1 and S_2 resynchronize and climb up along $f(x_i)$ within the surge regime. Panels (b1-b3): signals $y_i(t)$ generated with three different values of X_{sync} (1.5, 1.9, 2.1).

3.3.1 Conditions to get a camel surge: appropriate choice of X_{sync} and coupling strengths

A camel surge may arise only if the value of X_{sync} lies in a proper interval, hence, if the coupling is switched on at the right time. X_{sync} should be both small enough so that a significant difference between S_1 and S_2 can occur to create the first bump, and large enough so that S_1 and S_2 can have the time to resynchronize thanks to the coupling and climb up along the left branch of $f(x_1)$ and $f(x_2)$ respectively, as the second bump is built (see Figure 3.4 where α_1 and α_2 are kept constant while X_{sync} takes different values).

In the case of constant coupling, the effect of the coupling strengths is illustrated in Figure 3.6 (left panel), from which we can see that α_1 and α_2 should be nonidentical and the condition $\alpha_1 < \alpha_2$ should be satisfied for any appropriate X_{sync} value. The latter condition is required to force $y_2(t)$ to decrease steeply (by moving down along the left branch of $f(x_2)$) and catch up S_1 within a sufficiently narrow time interval. On the contrary, if $\alpha_1 \geq \alpha_2$, S_1 increases and catches up S_2 quite rapidly, and consequently both secretors go on climbing up simultaneously along $f(x_1)$ and $f(x_2)$, which results in a single-bump surge.

In the case of dynamic coupling, in addition to the effect of X_{sync} (see Figure 3.5),

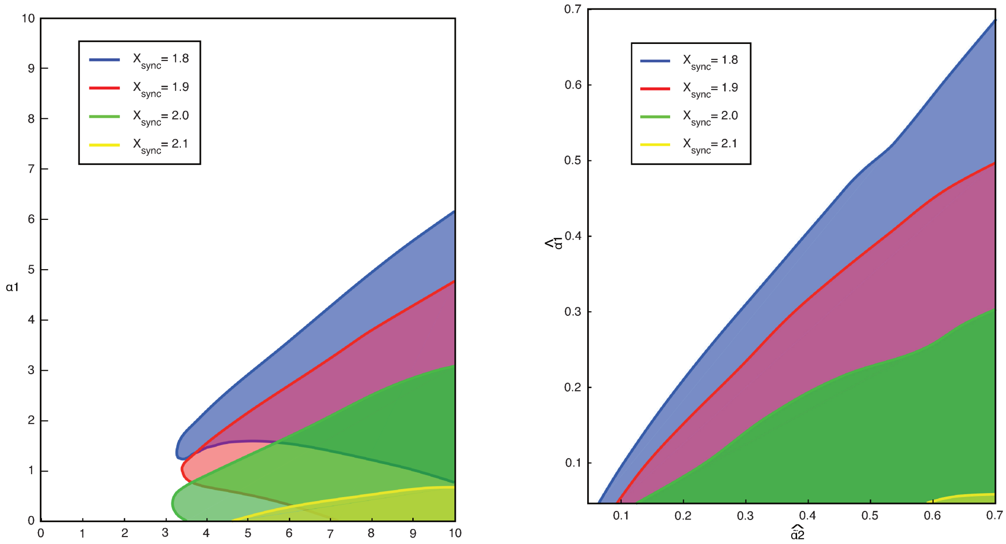

Figure 3.6: Coupling strengths compatible with a camel surge. The color-filled areas delimit the sets of coupling strengths (α_1, α_2) (left panel, constant coupling) or $(\hat{\alpha_1}, \hat{\alpha_2})$ (right panel, dynamic coupling) compatible with a camel surge for different values of $X_{sync} = \{1.8, 1.9, 2.0, 2.1\}$. The white area corresponds to parameter values leading to a single bump surge.

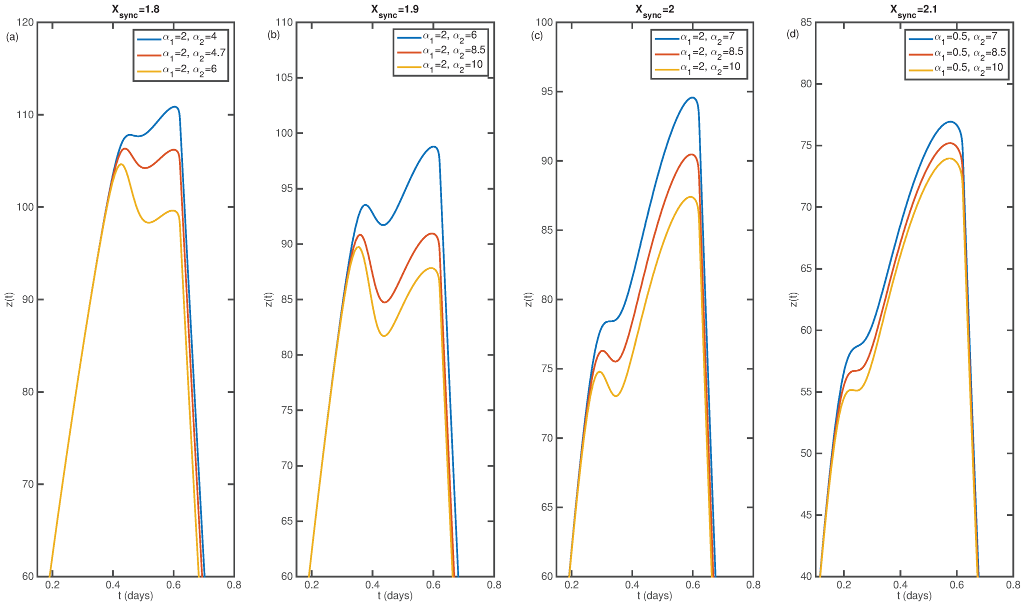

Figure 3.7: Bump ordering and surge amplitude in the case of constant coupling, for different values of $X_{sync}, \alpha_1, \alpha_2$.

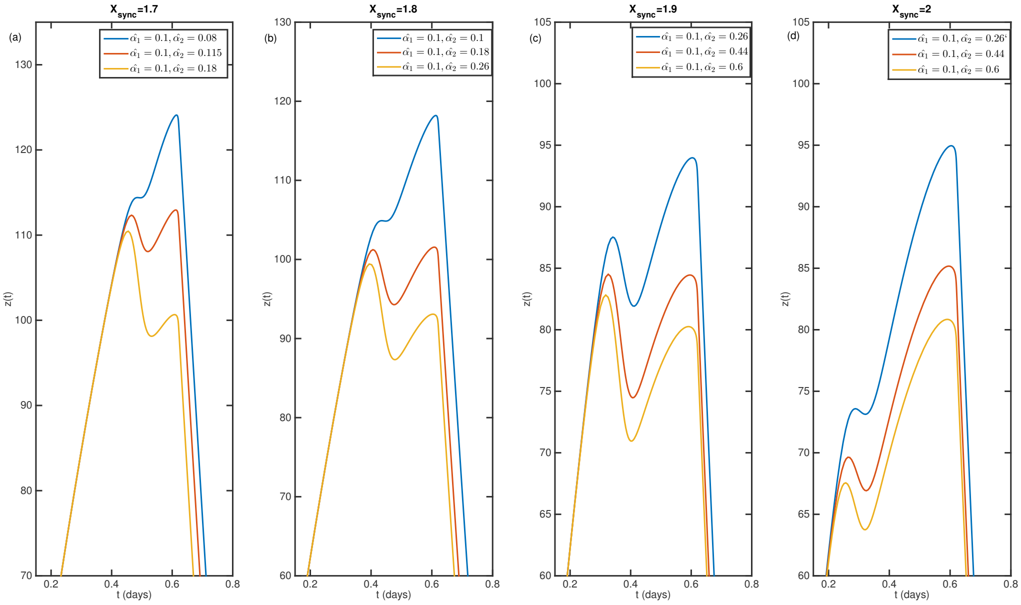

Figure 3.8: Bump ordering and surge amplitude in the case of dynamic coupling, for different values of $X_{sync}, \hat{\alpha_1}, \hat{\alpha_2}$.

the generation of a camel surge is facilitated by the dependency on the outputs $y_1^{out}(t)$ and $y_2^{out}(t)$, which makes variables y_i come closer to each other more easily, since the relation $\alpha_i < \hat{\alpha_i}\, y_i^{out}$ is preserved during the surge (in our parameter range). The range of $\hat{\alpha_1}, \hat{\alpha_2}$ and X_{sync} values suitable for a camel surge is thus larger. As can be seen in Figure 3.6 (right panel), the $\hat{\alpha_1} < \hat{\alpha_2}$ condition holds for $X_{sync} = 1.9$, 2.0, or 2.1, yet a camel surge can occur for $\hat{\alpha_1} \geq \hat{\alpha_2}$ if for instance $X_{sync} = 1.8$. Indeed, the asymmetry in the coupling, which is essential to generate a camel surge, persists even if $\hat{\alpha_1} = \hat{\alpha_2}$, due to the multiplication with y_i^{out} as long as $y_1^{out} \neq y_2^{out}$. Note that the ranges of both (α_1, α_2) and $(\hat{\alpha_1}, \hat{\alpha_2})$ values compatible with a camel surge get narrower as X_{sync} increases.

a Influence of X_{sync} and coupling strengths on the surge shaping

The shape of the surge, and especially the rank of the higher bump, can be determined according to the values of X_{sync} and coupling strengths.

In the case of constant coupling (3.2.8), the second bump is the higher if the activation occurs early in the surge, with X_{sync} values such that $X_{sync} > 1.95$. When the coupling gets activated before the difference between y_1 and y_2 has become too high, the secretors move up simultaneously along the left branch of $f(x_1)$ and $f(x_2)$ for a long enough time. If the activation occurs late in the surge, with X_{sync} values such that as $X_{sync} < 1.8$, the motions of the secretors are first independent, which generates the first bump, and then the duration of the simultaneous motions along $f(x_1)$ and $f(x_2)$ is too short for the second bump to overcome the first one. For intermediate X_{sync} values, the relation between α_1 and α_2 tunes the rank of the greater bump rather finely. For instance, we have observed numerically that an approximate ratio such as $\frac{\alpha_1}{\alpha_2} \approx 0.25$ for $X_{sync} = 1.9$ acts as a threshold to determine the order of the bumps: $\frac{\alpha_1}{\alpha_2} < 0.25$ leads to a higher first bump due to a quick and sharp decrease in y_2, whereas the ratio $\frac{\alpha_1}{\alpha_2} > 0.25$ allows S_1 to catch up S_2 and build a higher second bump.

The rank of the bump with the greater amplitude can also be reversed depending on the values X_{sync}, for a same combination of coupling strengths α_1 and α_2. In the center panels of Figure 3.7, we can see that secretors coupled with $\alpha_1 = 2$ and $\alpha_2 = 8.5$ lead to two distinct bumps with similar amplitudes for $X_{sync} = 1.9$, whereas the first bump is lower than the second for $X_{sync} = 2$. Alternatively, changing one of the coupling strengths, as in the case of the leftmost and center left panels of Figure 3.7, alters the order of the highest bump.

In the case of dynamic coupling, the order of the higher bump is also determined by the values of X_{sync} and the coupling strengths' ratio, $k = \frac{\hat{\alpha_1}}{\hat{\alpha_2}}$. Panel (b) of Figure 3.8 illustrates what happens for 3 values of $\hat{\alpha_2}$ when we keep $X_{sync} = 1.8$ and $\hat{\alpha_1} = 0.1$. Increasing the value of $\hat{\alpha_2}$ from $\hat{\alpha_2} = 0$; a camel surge is obtained with $\hat{\alpha_2} = 0.1$, the second bump is the highest until $\hat{\alpha_2} = 0.18$, for which the amplitudes of both bumps are similar, and finally the first bump becomes the highest for $\hat{\alpha_2} > 0.18$. The surge shape is also affected by the activation threshold X_{sync} and by the slope ρ of the activation function (3.2.7) (a first bump occurs more easily as the slope gets steeper). For instance, with $\hat{\alpha_1} = 0.1$ and $\hat{\alpha_2} = 0.18$, the highest bump is the first when $X_{sync} = 1.7$, while when $X_{sync} = 1.8$ both bumps have a comparable amplitude.

Due to the dimension and highly nonlinear character of the 6D model, it is very difficult to go beyond a numerical study of the surge features. In the next section, we nevertheless derive more analytical expressions to describe the time of occurrence of each surge bump with respect to the dynamics of $X(t)$.

b Timing of the first and second bumps

Besides determining the ordering of the bumps, we are also interested in assessing *a priori* the times of occurrence of each bump. There is a very simple way to assess the time of the first bump, $t_{1st\,bump}$, since it almost coincides with the time of activation of the coupling, t_{sync}, as can be checked on Figures 3.4 and 3.5. Indeed, the camel surge is shaped by a local minimum in $z(t)$ that clearly separates the bumps. This minimum is caused by the drop in $z(t)$ following the activation, which itself is due to the decrease in the output variable y_i in one of the oscillators which is ahead of the other $(y_i > y_j)$.

As a result, the value of $t_{1st\,bump}$ can be controlled by tuning the value of the activation threshold, X_{sync}, hence of t_{sync}. To do so, we look for a tractable expression of $X(t)$ during the surge regime, from (3.2.2e)-(3.2.2f). At that time, (X, Y) follows the slowest time scale and the current point (X, Y) remains in an $O(\delta)$ neighborhood of the $g(X)$ cubic. Noting $Y = h_\delta(X)$, where $(X, \delta) \mapsto h_\delta$ is an analytic function on $]-\infty, \gamma[\times\mathbb{R}_+^*$ and $h_0(X) = g(X)$, we get as a reduced system $\dot{Y} = \dot{X} h'_\delta(X)$, where $h'_\delta(X) = g'(X) + O(\delta)$:

$$\dot{X} = \frac{X + b_1(g(X) + O(\delta)) + b_2}{g'(X) + O(\delta)}.$$

In the limit $\delta = 0$, $X(t)$ is the solution of

$$\int dt = \int \frac{g'(X)}{X + b_1 g(X) + b_2} dX = \int \frac{3\mu_3 X^2 + \mu_1}{X + b_1(\mu_3 X^3 + \mu_1 X) + b_2} dX \tag{3.3.1}$$

This integral can not be computed explicitly because of the nonlinearity. In order to obtain a more tractable formula for X_{sync}, we linearize the nonlinear expression $g(X) = (\mu_3 X^3 + \mu_1 X)$ on the right branch, between the points $(X_{max}, g(X_{max}))$ and $(X_{sync}, g(X_{sync}))$, to get a linear approximation:

$$g^*(X) = PX + R,$$

where $P = (\mu_3(X_{max}^2 + X_{max}X_{sync} + X_{sync}^2) + \mu_1)$ and $R = -\mu_3 X_{max} X_{sync}(X_{max} + X_{sync})$. Substituting $g^*(X)$ to $g(x)$ in (3.3.1), we finally obtain:

$$\begin{aligned} t_{sync} &= \int_{X_{max}}^{X_{sycn}} \frac{P}{X + b_1(PX + R) + b_2} dX \\ &= \frac{P}{1 + b_1 P} \log((1 + b_1 P)X(t) + b_1 R + b_2)|_{X_{max}}^{X_{sycn}}, \\ X_{sync} &= \frac{(1 + b_1 P + b_1 R + b_2)X_{max} \exp(\frac{(1+b_1 P)}{P} t_{sync}) - (b_1 R + b_2)}{1 + b_1 P}. \end{aligned} \tag{3.3.2}$$

The occurrence of the second bump $t_{2nd\,bump}$ can also be simply assessed as the time when variable X jump leftwards (phase-4 in panel (a) of Figure 3.1), which occurs approximately for $X(t = t_\gamma) = \gamma$. A similar approximate expression as (3.3.2) for t_{sync} cannot be derived for t_γ, since extending the upper bound of integral (3.3.1) leads to too inaccurate estimations. Yet we can note that the value of t_γ only depends on the parameters entering system (3.2.2e)-(3.2.2f), and is not affected by the coupling terms.

3.3.2 Link between the camel surge and desynchronization during the pulsatile phase

The properties of the synchronous solutions depend on the differences between the intrinsic frequencies, coupling functions and coupling strengths. The difference in frequencies as well as the changes in individual frequencies is crucial in the dynamics of the 6D system. The series of IPI_i differ from oscillator S_1 to oscillator S_2, even in the uncoupled case, and in addition the shift in the IPI_i values change with $X(t)$. At the beginning of the pulsatile regime, the frequency difference is small enough to preserve synchronized pulses for a while, even with very small coupling strengths. As $X(t)$ increases, it eventually reaches a given value from which the effect of coupling is eventually overcome by the increasing frequency difference, and the secretors desynchronize. We note this critical value of X as the *desynchronization value*, $X_{desync}^{6D} = X(t_{desycn}^{6D})$, where t_{desycn}^{6D} is the *desynchronization time* (computed from the beginning of the current pulsatile regime). Figure 3.9 illustrates the effect of frequency difference on desynchronization during the pulsatile regime in the case of constant coupling ($\alpha_1 = \alpha_2 = 0.1$). After a transient regime where the order of spiking is reversed several times, one oscillator gets ahead of the other. For a while, the series of both pulse widths IPI_i in the coupled oscillators remain enveloped by their counterparts in

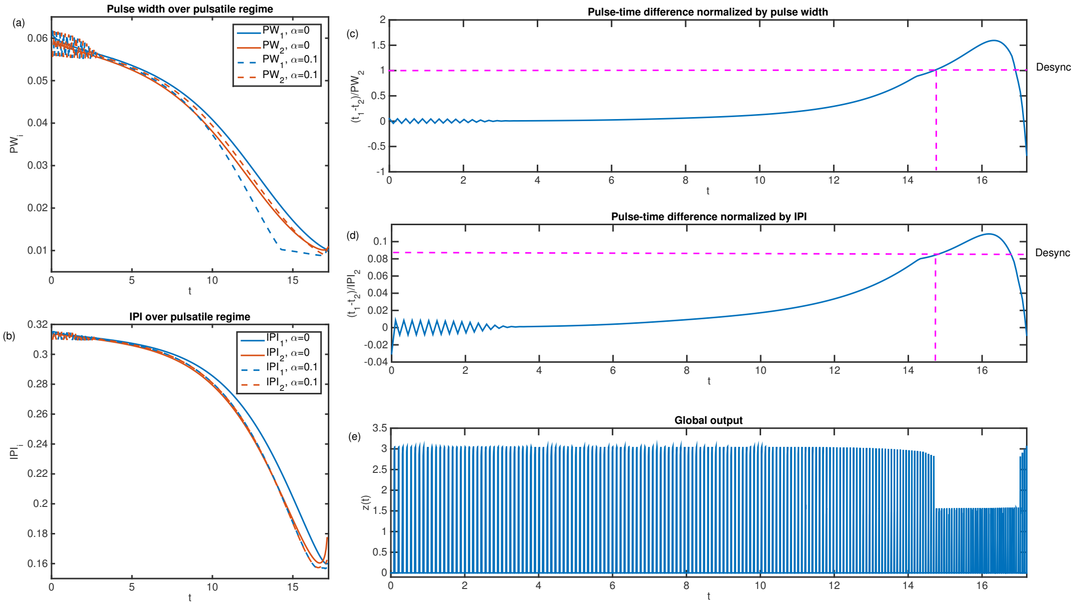

Figure 3.9: Frequency difference and desynchronization. Series of pulse widths, PW$_i$, (Panel (a)) and series of IPI$_i$ (Panel (b)) in uncoupled (solid lines) and coupled (dashed lines) secretors. Panel (c): differences in the onset times of pulses, normalized by the pulse width ($(t_1 - t_2)/PW_2$). Panel (d): differences in the onset times of pulses, normalized by the IPI ($(t_1 - t_2)/IPI_2$). Pink dashed lines help to locate the desynchronization time. Depending on the coupling strengths, the order of spiking can be transiently reversed several times, and then one the oscillators (S_2 here) gets ahead of the other. Panel (e): global output $z(t)$ for $\alpha_1 = \alpha_2 = 0.1$ during the pulsatile regime.

uncoupled oscillators, and they are almost superimposed, meaning that the frequency difference is attenuated in the coupled oscillators. Close to the desynchronization time, ($t^{6D}_{desycn} = 14.7$), the IPI$_i$s of coupled systems get out of the envelope.

The pattern followed by PW_1 during the pulsatile regime can be explained as following: after the transient response, S_2 is ahead of S_1. With the effect of the $(x_2 - x_1)$ difference, S_2 slows down, and consequently widens PW_2 compared the uncoupled case. On the other hand, the $(x_1 - x_2)$ difference accelerates S_1 and narrows PW_1. Especially when S_2 undergoes a leftward jump, the steep increase in the $(x_1 - x_2)$ difference results a sharp peak in the pulse of S_1.

For small coupling strengths, the effect of the frequency difference is similar with constant or dynamic coupling, yet the associated surge patterns are quite different, as illustrated in Figure 3.10. In the constant coupling case, systems coupled with small α_i values do not generate a camel surge, yet, they can undergo desynchronization. On the contrary, systems coupled with strong α_i values can generate a camel surge, yet they do not undergo desynchronization. In contrast, in the dynamic coupling case, the systems both generate a camel surge and undergo desynchronization.

In Section 4, we will focus on assessing the values of X^{6D}_{desync} and t^{6D}_{desync} in the case of dynamic coupling. Since this coupling involves both asymmetric and nonlinear

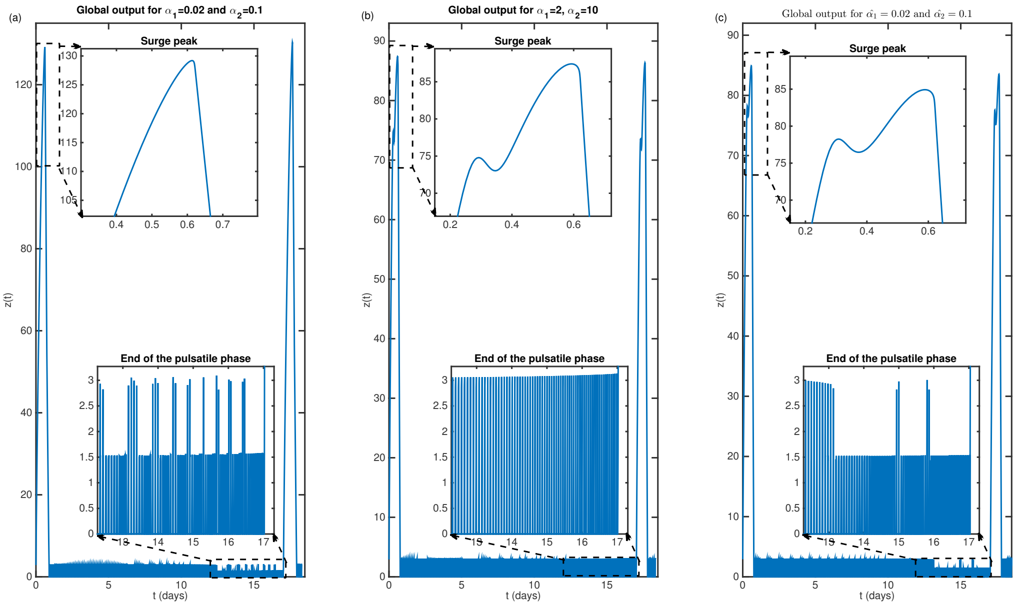

Figure 3.10: Signal $z(t)$ for $X_{sync} = 2$. Panel (a): constant coupling with small coupling strengths $\alpha_1 = 0.02$, $\alpha_2 = 1$; there is no camel surge and the oscillators get desynchronized at the end of the pulsatile regime. Panel (b): constant coupling with strong coupling strengths $\alpha_1 = 2$, $\alpha_2 = 10$: a camel surge occurs and the oscillators remain synchronized all along the pulsatile regime. Panel (c): dynamic coupling with small coupling strengths $\hat{\alpha_1} = 0.02$, $\hat{\alpha_2} = 0.1$: a camel surge occurs and the oscillators get desynchronized at the end of the pulsatile regime.

coupling terms, we cannot use standard tools and we introduce asymptotic tools in the next section.

3.4 Asymptotic tools for assessing the desynchronization time in the case of dynamic coupling

The time during which pulses remain synchronized depends on the strength of the coupling and increases as both the coupling strengths and their ratio, $k = \frac{\hat{\alpha_1}}{\hat{\alpha_2}}$, increase (Figure 3.11). In this section, we introduce two different asymptotic approaches, one based on a 4D quasi-static approximation, and the other based on geometric considerations, to assess X^{6D}_{desync} and t^{6D}_{desync} .

For the 4D quasi-static approach, we take advantage of the timescale separation of the 6D slow-fast system (3.2.2). During the pulsatile regime, $X(t) \in [X_{min}, -\gamma]$ (see phase-1 in Figure 3.1) and (X, Y) follows the left branch of $g(X)$ with the slowest timescale, $O(1)$, while $x_i(t)$ and $y_i(t)$ change at speeds $O(\varepsilon\delta)$ and $O(\delta)$, respectively. Since the change in $X(t)$ is very slow compared to the motion of (x_i, y_i), we can freeze

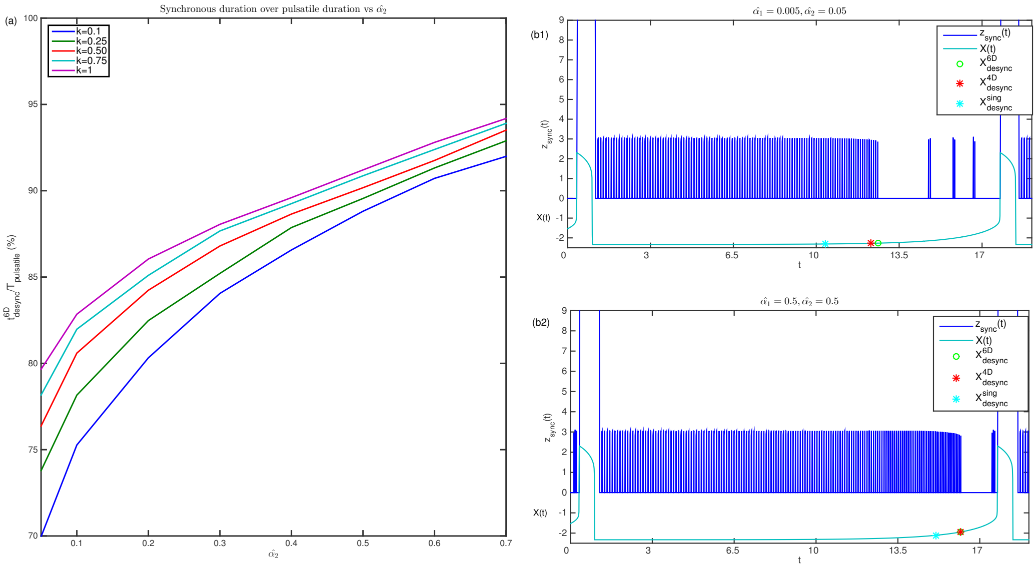

Figure 3.11: Assessment of the desynchronization time. Panel (a) Relative duration of synchronization in the pulsatile regime ($t^{6D}_{desync}/T_{pulsatile}$) as a function of coupling strength $\hat{\alpha_2}$, for different ratios $k = \hat{\alpha_1}/\hat{\alpha_2}$. Panels(b1-b2) $z_{sync}(t)$ (3.2.5) along the pulsatile regime together with the values of X^{6D}_{desync} (green circle), X^{4D}_{desync} (red asterisk) and X^{sing}_{desync} (cyan asterisk), superimposed on $X(t)$ for $\hat{\alpha_1} = 0.005$, $\hat{\alpha_2} = 0.05$ (b1) or $\hat{\alpha_1} = 0.5$, $\hat{\alpha_2} = 0.5$ (b2).

$X(t)$ as a constant and consider it as a parameter in the following system:

$$\begin{aligned} \varepsilon \dot{x_1} &= -y_1 + f(x_1), \\ \dot{y_1} &= a_0 x_1 + a_1 y_1 + a_2^{(1)} + c^{(1)} X + \hat{\alpha_1}\, y_1^{out}(x_1 - x_2), \\ \varepsilon \dot{x_2} &= -y_2 + f(x_2), \\ \dot{y_2} &= a_0 x_2 + a_1 y_2 + a_2^{(2)} + c^{(2)} X + \hat{\alpha_2}\, y_2^{out}(x_2 - x_1) \end{aligned} \tag{3.4.1}$$

For fixed values of $\hat{\alpha_1}$,and $\hat{\alpha_2}$, we first simulate system (3.4.1) with X in the range $[X_{min}, -\gamma]$ with a $|0.00125|$ resolution in X to find for which value, denoted by X^{4D}_{desync}, the synchronized pulses disappear. We then deduce the desynchronization time t^{4D}_{desync}, such that $X^{4D}_{desync} = X(t^{4D}_{desync})$, from the simulation of (3.2.2e)-(3.2.2f).

The geometric approach is based on our definition of synchronization. The secretors interact via variables y_i, so that the coupling terms directly affect the locations of the y_i-nullclines. Assume that both S_1 and S_2 are on the right branch of the x_i-nullclines and S_2 is ahead ($x_2 < x_1$, $y_2 > y_1$). The coupling may lead to a recurrent bifurcation in S_2 according to the following scenario: when the coupling is switched on, the unstable equilibrium point (x_2^*, y_2^*) lying on the middle branch of $f(x_2)$ moves rightwards and crosses the upper fold. Then, a quasi-stationary equilibrium point appears on the right branch of $f(x_2)$ and slows down the motion of $(x_2(t), y_2(t))$, since

$$(a_0 x_2 + a_1 y_2 + a_2^{(2)} + c^{(2)} X) > (a_0 x_2 + a_1 y_2 + a_2^{(2)} + c^{(2)} X + \hat{\alpha_2}\, y_2^{out}(x_2 - x_1))$$

with $\hat{\alpha_2}\, y_2^{out}(x_2 - x_1) < 0$. Once the $(x_2 - x_1)$ difference starts to decrease, the quasi-equilibrium (x_2^*, y_2^*) moves leftwards, crosses the upper fold again and goes back to the middle branch, so that a relaxation limit cycle reappears. This sequence occurs under the condition that a quasi-equilibrium point, (x_2^*, y_2^*), appears on the right branch when the coupling is switched on, which slows down the motion of S_2 and delays the time when it reaches the upper fold and undergoes the leftwards jump. A synchronized pulse can thus occur if y_1 reaches y_{TH} before the leftwards jump of S_2. Such a condition can be guaranteed if the quasi-stationary point (x_2^*, y_2^*) has not yet crossed the upper fold of the x_2-nullcline, $(x_{f+}, f(x_{f+}))$, at the time when $(x_1, y_1) = (x_{TH}, y_{TH})$ with $y_{TH} = f(x_{TH})$, $x_{TH} > 0$. This assumption can be expressed from identifying (x_2^*, y_2^*) with $(x_{f+}, f(x_{f+}))$, from which we get the maximal X value compatible with synchronized pulses:

$$X_{desync}^{sing} = \frac{-f(x_{f+})(a_1 + \hat{\alpha_2}(x_{f+} - x_{TH})) - a_0 x_{f+} - a_2^{(2)}}{c^{(2)}}. \tag{3.4.2}$$

Note that X_{desync}^{sing} only depends on $\hat{\alpha_2}$. As in the 4D approach, the corresponding desynchronization time t_{desync}^{sing}, such that $X_{desync}^{sing} = X(t_{desync}^{sing})$ is computed from the simulation of (3.2.2e)-(3.2.2f).

Figure 3.12 allows one to compare the desynchronization values and corresponding desynchronization times obtained with different approaches, for several pairs of $\hat{\alpha_1}$ and $\hat{\alpha_2}$. The values obtained with the 4D approach match well those obtained from the simulation of (3.2.2) and the accuracy of the approximation increases with $\hat{\alpha_2}$ and k. The geometric approach leads to poorer results, since the assessed values of both X_{desync}^{sing} and t_{desync}^{sing} clearly underestimate the proper values. The effect of $\hat{\alpha_2}$ in the geometric approach is contrasted: the error in t_{desync}^{sing} values diminishes as $\hat{\alpha_2}$ increases, whereas the error in X_{desync}^{sing} increases. This difference is due to the fact that the change in $X(t)$ becomes faster as $X(t)$ approaches $-\gamma$, so that a small time step results in a greater change in $X(t)$ than when $X(t)$ is far from the left fold.

Even if there is some discrepancy with the simulation of the 6D model, the values assessed by these approaches, especially with the 4D quasi-static approach, can be used as an initial guess to select the parameter values given a priori specifications on the time of desynchronization, as we will comment further on in the next session.

3.5 Gathering information on camel surge and desynchronization

From the previous sections, we know that we need to make use of a nonlinear and asymmetric coupling to guarantee the proper qualitative sequence in the 6D secretion model (3.2.2). We also have means of finding appropriate parameter values subject to quantitative specifications, such as the rank of the higher bump, the bump occurrence times, and the desynchronization time. In this section, we combine these information with the results exposed in [3] dealing with the quantitative study of the 4D model (1.1.1) and allowing one to set other features such as the relative duration and amplitude of the surge with respect to the pulsatile regime, and the pulse frequency increase.

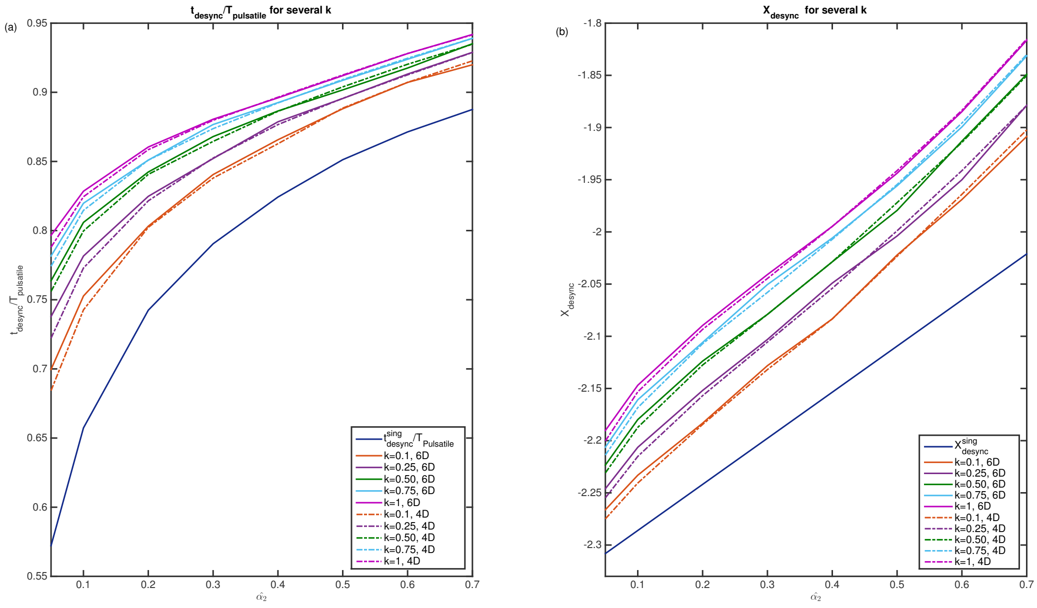

Figure 3.12: Assessment of the desynchronization time. Relative duration of synchronization in the pulsatile regime ($t^{6D}_{desync}/T_{pulsatile}$, Panel(a)) and associated values of X_{desync} (Panel (b)) observed by numerical simulations (solid lines) or assessed by the 4D approximation (dotted-dashed lines) or nullcline-based approximation (solid blue lines), as a function of coupling strength $\hat{\alpha_2}$ and for different ratios $k = \hat{\alpha_1}/\hat{\alpha_2}$. Orange lines: $k = 0.1$, purple lines: $k = 0.25$, green lines: $k = 0.50$, cyan lines: $k = 0.75$, magenta lines: $k = 1$.

More specifically, we describe how to select proper parameter values so as to mimic specific experimental data sets.

The shape of the GnRH surge can be examined from time series of GnRH levels assessed through direct sampling into the pituitary portal blood, thanks to a surgical technique which has been settled in the ovine species. Several instances of camel surges are documented in the literature, either on individual time series [82, 83, 86] or on average time series pooling data sets obtained from several ewes [84, 85]. In most cases, the first bump (which coincides with the LH surge on the pituitary level) is higher or almost equal to the second one. We have picked up two specific instances of individual camel surges.

The first instance corresponds to the bottommost left panel of Figure 4 in [82] (see the schematic drawing in panel (a) of Figure 3.13). After normalizing the surge duration (≈ 12 h) to one time unit, we can read from the data the bump occurrence times: $t_{1st\,bump} \approx 0.3$ and $t_{2nd\,bump} \approx 0.66$, and the ratio of amplitude in the second bump with respect to the first bump: 0.4. Since the experimental time series is focused on the surge period and does not encompass a large enough part of the pulsatile regime to assess the desynchronization time accurately, we just intend to reproduce the camel surge, and we can do so using either the constant or dynamic coupling function.

We first choose S_2 as the secretor that will generates the highest bump, whose

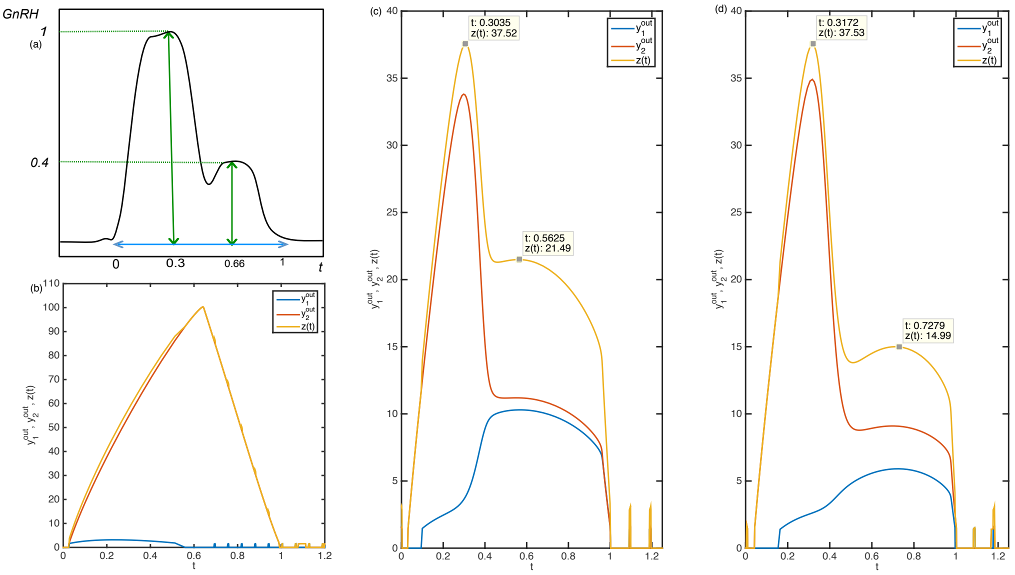

Figure 3.13: Mimicking an experimental camel surge. Panel (a) Schematic drawing of the experimental data, inspired from Figure 4 in [82]. Panel (b) Surge shape obtained from uncoupled secretors with $c^{(1)} = 0.29, a_2^{(1)} = 0.4$. Panel (b) Surge shape obtained from constant coupling, with $\alpha_1 = 5$, $\alpha_2 = 25$, $X_{sync} = 2.07, \rho = 40$. Panel (d) Surge shape obtained from dynamic coupling with $\hat{\alpha_1} = 0.15$, $\hat{\alpha_2} = 0.6$, $X_{sync} = 2.07, \rho = 40$. The time unit on the horizontal axis is rescaled with respect to the whole surge duration. In panels (b) to (d), both the global output variable $z(t)$ (yellow curve) and the individual outputs y_1^{out} (blue curve) and y_2^{out} (red curve) are displayed.

amplitude is set by the nominal parameter values in Table 3.1. Since there is a great contrast in the magnitude of the bumps, we select $c^{(1)} = 0.29, a_2^{(1)} = 0.4$ to get a significantly lower intrinsic surge amplitude in S_1. From the constraints imposed on the bump ranking and amplitude, we get $\hat{\alpha_1} < \hat{\alpha_2}$ and $\alpha_1 < \alpha_2$. To match the sharp increase in the first bump, we set ρ (the slope of the activation function in (3.2.7)) to a high value ($\rho = 40$). Finally, we compute the activation value from (3.3.2), which results in $X_{sync} = 2.07$.

Figure 3.13 shows the resulting surge patterns in the case of constant coupling (Panel (c), with $\alpha_1 = 5.0$ and $\alpha_2 = 25.0$) and dynamic coupling (Panel (d) with $\hat{\alpha_1} = 0.15$, $\hat{\alpha_2} = 0.6$). The dynamic coupling approach leads to a much better quantitative match between the experimental and simulated values, with estimated values $t_{1st\,bump} = 0.3$, $t_{2nd\,bump} = 0.72$ and an amplitude ratio close to 0.405.

The second instance corresponds to the left panel of Figure 2 in [83] (see the schematic drawing in panel (a) of Figure 3.14). In addition to the surge period, from which we can see a reverse pattern with a higher second bump, the time series encompasses an almost 30h long pre-surge period, from which we can infer a desynchronization duration of 16h (the complete time window amounting to as long as 48h). After normalizing again the surge duration (≈ 18h) to one time unit, we can read from the data the bump occurrence times: $t_{1st\,bump} \approx 0.44$ and $t_{2nd\,bump} \approx 0.66$, and the amplitude ratio : ≈ 1.15 (greater than 1 since the second bump is higher), and, following [3] and [4] to set the ratio of the duration of the pulsatile regime with respect to the surge (15.5), we can also get the normalized desynchronization time (0.94).

We derive the corresponding parameter set in the framework of dynamic coupling, since we cope here with both the camel surge and desynchronization issues. The long synchronized duration added to the amplitude ratio require slightly different, yet quite strong coupling strengths (as can be seen on Figure 3.12). We thus set as initial guess $\hat{\alpha_1} = 0.5$, $\hat{\alpha_2} = 0.7$, compute $X_{sync} = 1.92$ from (3.3.2), keep a steep slope $\rho = 40$ and combine these values with the nominal values of the other parameters (Table 3.1). The resulting $z(t)$ output is displayed on Panel (c) of Figure 3.14. The bump occurrence times are met properly ($t_{1st\,bump} = 0.44$, $t_{2nd\,bump} = 0.67$), but there remains some discrepancy between the simulated and raw data as far as the desynchronization time ($t_{desync} = 0.67$) and amplitude of the surge are concerned. The maximal amplitude overcomes 100, which it is twice greater than the experimental maximum. In addition, the contrast between the amplitudes of the bumps is not pronounced enough. To improve the fit, we cannot just tune separately the surge amplitude since this would alter too much the duration of the pulsatile regime with respect to the surge duration. As a consequence, in addition to decreasing the surge amplitudes by taking $c^{(1)} = 0.35$, $a_2^{(1)} = 0.325$, $c^{(2)} = 0.502$, $a_2^{(2)} = 0.6805$, we have to alter the nominal parameter values of the regulator in order to preserve the balance between the durations of the pulsatile regime and surge. This amounts to controlling the time during which $X(t) < 0$ along the relaxation cycle, as described in [3], and to lengthening it with a slightly decreased b_2 value ($b_2 = 1.503$).

The effect of the duty cycle (the proportion of a cycle period in which the oscillators remains active), as well as of frequency and synaptic decay, has been studied extensively in the literature dealing with synaptically coupled relaxation oscillators (see for instance [94, 95, 43]). We can make an analogy between our dynamic coupling function and the synaptic coupling functions since in both cases the cycles interact during their active phase. We have already discussed the effect of the intrinsic frequencies of the secretors on synchronization. It is worth noting here that the threshold parameter y_{TH} tunes the duty cycle (the higher y_{TH}, the lower the duty cycle) and it affects the synchronized duration. Hence, to get closer to the experimental desynchronization time, we also modify slightly the value of y_{TH} and set it to $y_{TH} = 1.392$.

Endowed with these modified values of b_2 and y_{TH}, we can further take advantage of the asymptotic approaches exposed in the former section to select the corresponding coupling strengths, by going through the following steps:

1. Determine $X^{6D}_{desync} = X(t_{desync})$ by simulating the 6D model with the current parameter values;

2. Specify the leading oscillator, S_i, for X^{6D}_{desync} and compute an initial guess for $\hat{\alpha_i}$ from the geometric approach (3.4.2);

3. Simulate the 4D model with $X = X^{6D}_{desync}$ and the guessed $\hat{\alpha_i}$, and determine $\hat{\alpha_i}$ and $\hat{\alpha_j}$ more precisely;

4. Update $\hat{\alpha_i}$ and $\hat{\alpha_j}$ with respect to the surge specifications.

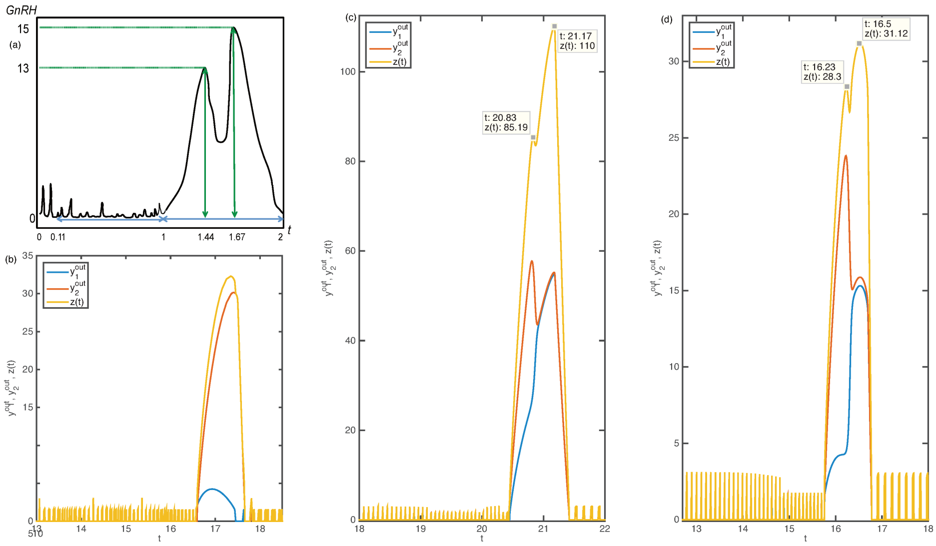

Figure 3.14: Mimicking an experimental camel surge. Panel (a) Schematic drawing of the experimental data, inspired from Figure 2 in [83]. (b) Surge shape obtained from uncoupled secretors with the alternative parameter values $c^{(1)} = 0.35$, $a_2^{(1)} = 0.325$, $c^{(2)} = 0.502$, $a_2^{(2)} = 0.6805$, $b_2 = 1.503$. Panel (c) Surge shape obtained from dynamic coupling with the nominal parameter values of Table 3.1, and $X_{sync} = 1.92$, $\hat{\alpha}_1, = 0.5, \hat{\alpha}_2 = 0.7$, $\rho = 40$. (d) Surge shape obtained from dynamic coupling with the alternative values of $a^{(i)}$, $c^{(i)}$, b_2, $y_{TH} = 1.392$ and $X_{sync} = 1.92$, $\hat{\alpha}_1 = 0.5$, $\hat{\alpha}_2 = 1.0$. The time unit on the horizontal axis is rescaled with respect to the whole surge duration. In panels (b) to (d), both the global output variable $z(t)$ (yellow curve) and the individual outputs y_1^{out} (blue curve) and y_2^{out} (red curve) are displayed.

From these steps we get $\hat{\alpha}_1 = 1.0$, $\hat{\alpha}_2 = 0.5$. The resulting $z(t)$ output is displayed on Panel (d) of Figure 3.14, from which we can see that not only the bump occurrence times, but also their relative amplitudes and the desynchronization time meet the experimental specifications. Moreover, the pulse frequency increases during the pulsatile with a fourfold ratio (from 7 pulses/day to 22 pulses/day), which appears to be consistent with the physiological specifications [3], but requires to include very narrow pulses in the inventory of all pulses. One can notice that the absolute simulated amplitudes of the bumps are still different from the experimental ones. We do not intend to improve this feature, since further decreasing the intrinsic surge amplitudes of the individual secretors would attenuate too much the amplitude differences between the secretors (hence the local minimum in $z(t)$ during the surge). Moreover the surge amplitude is subject to a great experimental variability (it depends on the anatomical level of the surgical section on the hypothalamic-pituitary stalk), and, compared to other available data sets, the maximal surge amplitude appears to be particularly low in this specific instance.

3.6 Analytic tools for assessing desynchronization time in the case of constant coupling

As we have discussed in the previous sections, both types of coupling function promote synchronization in the pulsatile regime, as the secretors follow a relaxation cycle. The ability of the coupling to synchronize the oscillator activities depends on the coupling strength, intrinsic properties and pulse frequency. In this section, we consider the constant coupling function and make use of results from the weakly coupled oscillators theory to investigate systematically the basic mechanisms leading to desynchronization. We apply the constant coupling in a parameter configuration which is compatible with desynchronization but not a camel surge (as in Panel (a) of Figure 3.10, see also the secretion pattern along a whole ovarian cycle in Figure 3.15). Then, we establish a link between period doubling bifurcations occurring in the presence of both weak (constant) coupling and weak heterogeneity, and the desynchronization time in the original 6D model. It appears that both weakly coupled oscillator theory and bifurcation analysis using numerical continuation provide reasonable estimations of X^{6D}_{desync} values of constantly coupled systems yielding outputs with a single surge (Figure 3.15). Note that the use of the weakly coupled oscillator theory and bifurcation analysis are quite restricted in the dynamic coupling framework due to the asymmetric and nonlinear characteristic of this setting (see Section 7 for a detailed discussion).

3.6.1 Application of weakly coupled oscillators theory to symmetric constant coupling

Phase equations and the interaction function have been studied extensively in the framework of weakly coupled oscillator theory [49, 48]. The change in the phase difference ϕ along one period, under the assumption of weak coupling and weak heterogeneity, can be expressed as:

$$\frac{d\phi}{dt} = \Delta\omega + \alpha G(\phi) \tag{3.6.1}$$

where $\Delta\omega$ is the weak heterogeneity in the intrinsic frequencies, α is the weak coupling strength and $G(\phi)$ is the "cell pair coupling function" or more generally *G-function*. Briefly, a stationary phase difference ϕ^* defined by $-\Delta\omega = \alpha G(\phi^*)$ is stable if $G'(\phi^*) < 0$ (See Appendix 3.8 for the G-function).

In order to derive phase equations in the pulsatile regime, we use the 4D reduction of the 6D model (similarly as in Section 4 to derive system (3.4.1)) with constant coupling:

$$\begin{aligned}
\varepsilon \dot{x_1} &= -y_1 + f(x_1), \\
\dot{y_1} &= a_0 x_1 + a_1 y_1 + a_2^{(1)} + c^{(1)} X + \alpha_1 (x_1 - x_2), \\
\varepsilon \dot{x_2} &= -y_2 + f(x_2), \\
\dot{y_2} &= a_0 x_2 + a_1 y_2 + a_2^{(2)} + c^{(2)} X + \alpha_2 (x_2 - x_1).
\end{aligned} \tag{3.6.2}$$

If $t_{pulse,i} = t_i^* - t_i$ is the constant pulse width (since X is a parameter) generated by the i-th oscillator in system (3.6.2) and $T_i (= IPI_i)$ is the period, then $\phi_{pulse,i} = \frac{t_{pulse,i}}{T_i}$

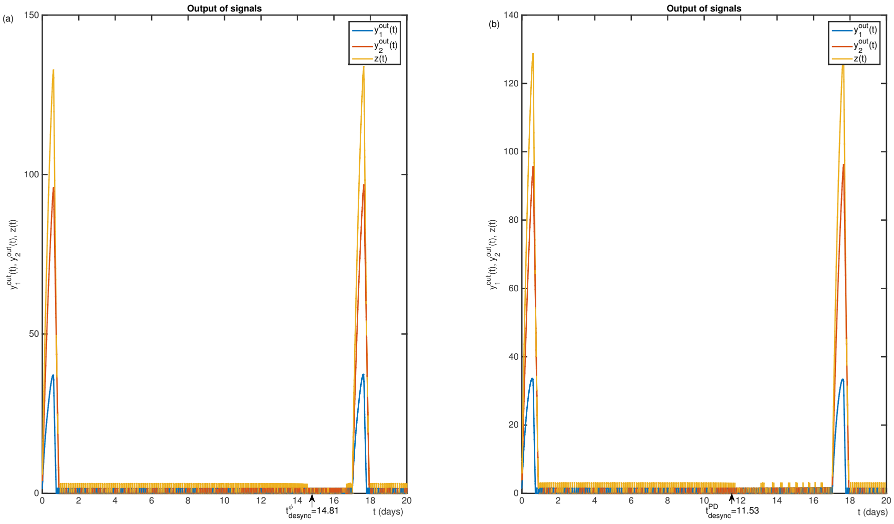

Figure 3.15: Signals $y_1^{out}(t)$ (blue), $y_2^{out}(t)$ (red) and $z(t)$ in the case of constant coupling (1.4.1) for $X_{sync} = 2$. Panel (a) $\alpha_1 = 0.1, \alpha_2 = 0.1$. Desynchronization occurs at $X^{6D}_{desync} = -2.11$ ($t^{6D}_{desync} = 14.53$). Disappearance of overlapping estimated by the weakly coupled oscillator theory occurs at $X = -2.07$ ($t^{\phi}_{desync} = 14.81$). Panel (b) $\alpha_1 = 0.01, \alpha_2 = 0.1$. Desynchronization occurs at $X^{6D}_{desync} = -2.2787$ ($t^{6D}_{desync} = 11.7$). PD bifurcation occurs at $X = -2.2826$ ($t^{PD}_{desync} = 11.53$).

refers to the phase window in which the pulse appears (duty cycle). Phase $\phi_{pulse,i}$ can be approximated with an $O(\varepsilon)$ error by $\phi^{\#}_{pulse,i}$ computed in the limit $\varepsilon = 0$.

Let us assume that (3.6.1) has a synchronous solution with phase difference $\phi = \phi^* > 0$. To obtain synchronized (i.e. overlapped) pulses we need

$$\phi^* < \phi^{\#}_{pulse}, \tag{3.6.3}$$

meaning that the steady phase difference ϕ^* is less than the maximum pulse width

$$\phi^{\#}_{pulse} = max(\phi^{\#}_{pulse,i}, \phi^{\#}_{pulse,j}).$$

Since $\phi^{\#}_{pulse}$ is the upper limit of the phase differences suitable for a synchronized pulse, $\Delta\omega^{\#}_{pulse} = -\alpha G(\phi^{\#}_{pulse})$ is the limiting frequency difference giving $\phi^{\#}_{pulse}$ phase-locked solutions. We can link condition (3.6.3) with the intrinsic frequency difference as follows:

$$|\Delta\omega^{\#}_{pulse}| > |\Delta\omega^*|$$

given that $\alpha G(\phi^*) = -\Delta\omega^*$. Since the intrinsic frequency and pulse width of (3.6.2) depend on parameter X, conditions above can be re-expressed as:

$$\begin{aligned} &\phi^*(X) < \phi^{\#}_{pulse}(X), \\ &|\Delta\omega^{\#}_{pulse}(X)| > |\Delta\omega^*(X)|. \end{aligned}$$

To compute the heterogeneity term $\Delta\omega$ explicitly by following [56] and [49] (see Appendix 3.8), equation (3.6.2) is rewritten as:

$$S_1 : \begin{bmatrix} \varepsilon\dot{x_1} \\ \dot{y_1} \end{bmatrix} = \begin{bmatrix} -y_1 + f(x_1) \\ a_0x_1 + a_1y_1 \end{bmatrix} + \begin{bmatrix} 0 \\ \frac{a_2^{(1)}+a_2^{(2)}}{2} + \frac{a_2^{(1)}-a_2^{(2)}}{2} + \frac{c^{(1)}+c^{(2)}}{2}X + \frac{c^{(1)}-c^{(2)}}{2}X \end{bmatrix} + \begin{bmatrix} 0 \\ \alpha(x_1 - x_2) \end{bmatrix},$$

$$S_2 : \begin{bmatrix} \varepsilon\dot{x_2} \\ \dot{y_2} \end{bmatrix} = \begin{bmatrix} -y_2 + f(x_2) \\ a_0x_2 + a_1y_2 \end{bmatrix} + \begin{bmatrix} 0 \\ \frac{a_2^{(1)}+a_2^{(2)}}{2} - \frac{a_2^{(1)}-a_2^{(2)}}{2} + \frac{c^{(1)}+c^{(2)}}{2}X - \frac{c^{(1)}-c^{(2)}}{2}X \end{bmatrix} + \begin{bmatrix} 0 \\ \alpha(x_2 - x_1) \end{bmatrix}.$$

Noting

$$F(x,y) = \begin{bmatrix} -y_1 + f(x_1) \\ a_0x_1 + a_1y_1 \end{bmatrix} + \begin{bmatrix} 0 \\ \frac{a_2^{(1)}+a_2^{(2)}}{2} + \frac{c^{(1)}+c^{(2)}}{2}X \end{bmatrix},$$

$$\Delta(x,y) = \begin{bmatrix} 0 \\ (a_2^{(1)} - a_2^{(2)}) + (c^{(1)} - c^{(2)})X \end{bmatrix},$$

symmetrically coupled S_1 and S_2 dynamics reads:

$$\begin{aligned} \dot{S_1} &= F(x,y) + \frac{\Delta(x,y)}{2} + \alpha \begin{bmatrix} 0 \\ (x_1 - x_2) \end{bmatrix}, \\ \dot{S_2} &= F(x,y) - \frac{\Delta(x,y)}{2} + \alpha \begin{bmatrix} 0 \\ (x_2 - x_1) \end{bmatrix}. \end{aligned} \tag{3.6.4}$$

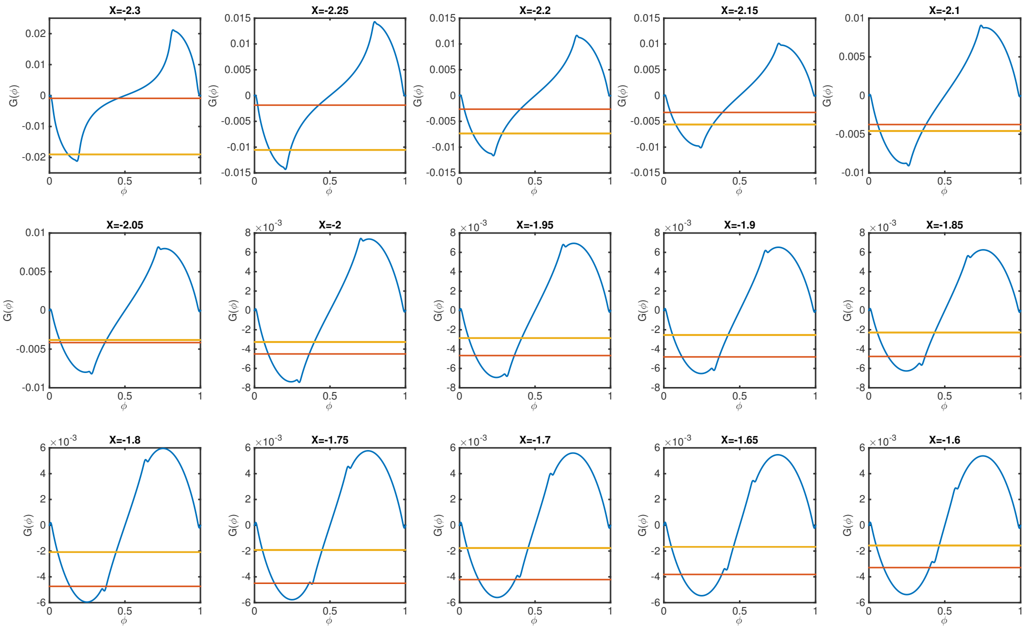

Figure 3.16: G-function (3.6.1) for $\alpha_1 = \alpha_2 = \alpha = 0.1$. Red line: $G(\Delta\omega^*)$. Yellow line: $G(\Delta\omega^{\#}_{pulse})$.

Noting that the adjoint solution is given by $Z(t)$, the phase difference dynamics read:

$$\frac{d\phi}{dt} = \Delta\omega + \alpha G(\phi) = \Delta(x, y)\frac{1}{T}\int_0^T Z(\tilde{t})d\tilde{t} + \alpha G(\phi).$$

Figure 3.16 shows how the level of heterogeneity, which increases with X, alters the phase-locking properties of the subsystems (3.6.4) and results in the loss of synchronized pulses defined in (3.2.5). For instance, while (x_1, y_1) and (x_2, y_2) oscillate with a phase difference $\phi^* = 0.18$ for $X = -2.05$, synchronized pulses are not visible in the global output of system (3.6.2) (Figure 3.17 top right panel).

The weakly coupled oscillator theory applied to the quasi-static 4D approximation in the case of constant coupling provides us with a reasonable approximation of the desynchronization value for symmetrically coupled secretors, in a parameter configuration generating a single bump surge (Figure 3.15-a).

In our original framework, we need nonidentical oscillators and asymmetric coupling strengths to reproduce a camel surge. In such a framework the G-function is not expected to be valid any more. Yet, in [57] and [61], the authors have shown that heterogeneity combined with stronger coupling can lead to period doubling (PD) bifurcations. Similar bifurcations have also been studied in e. g. [96, 97] in relaxation cycles subject to periodic perturbation. Hence, we find it worth investigating the possible bifurcations affecting the phase difference as a function of X, which may affect in turn the global output of the 4D and 6D systems.

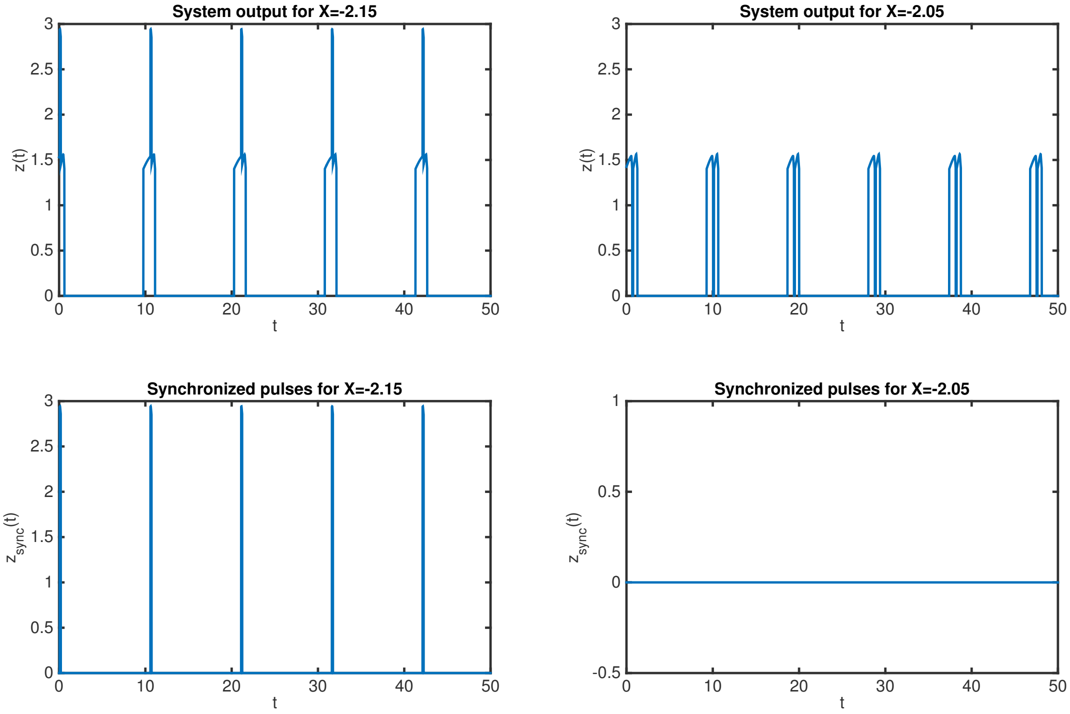

Figure 3.17: Outputs (upper panels) of (3.6.2) and synchronized pulses (3.2.5) (lower panels) for $X = -2.15$ (left panels) and $X = -2.05$ (right panels).

3.6.2 Effect of heterogeneity in asymmetric constant coupling

According to standard results, the analysis of the G-function reveals that out-of-phase synchronization (i.e. $\phi \neq \{0, \pi\}$) arises in weakly heterogeneous networks. To give an insight of a possible bifurcation structure in ϕ, we re-parameterize some parameters in system (3.6.2) for the sake of numerical continuation with AUTO:

$$a_2^{(1)} = a_2^{(2)} = a_2, \quad c^{(2)} = hc^{(1)}, \quad \alpha_1 = k\alpha_2.$$

We keep $h \leq 1$ to ensure the existence of a relaxation cycle in each uncoupled oscillator and $k < 1$ to satisfy the general requirement for obtaining a camel surge, even though we restrict ourselves to the pulsatile regime and cannot obtain a camel surge with such weak coupling strengths. The left panel of Figure 3.18 shows PD bifurcations depending on h in an asymmetrically coupled oscillators and Table 3.2 summarizes the bifurcation values with some k and α_2. We see that increasing heterogeneity (decreasing h) generates a cascade of PD bifurcations in the coupled system.

We can take the value of X instead of h as the bifurcation parameter ; we fix different values to h, α_2 and k and perform the numerical continuation with respect to X. The bifurcation values corresponding to the first two or three period doublings are gathered in Table 3.3. The corresponding bifurcation cascade is illustrated on the right panel of Figure 3.18. The PD bifurcations occur when the X-induced increase in the phase difference gets high enough, for instance at $\phi_{2T} = 0.235$ in Figure 3.18. It appears that X_{PD}, the value X for which the first PD bifurcation occurs in system

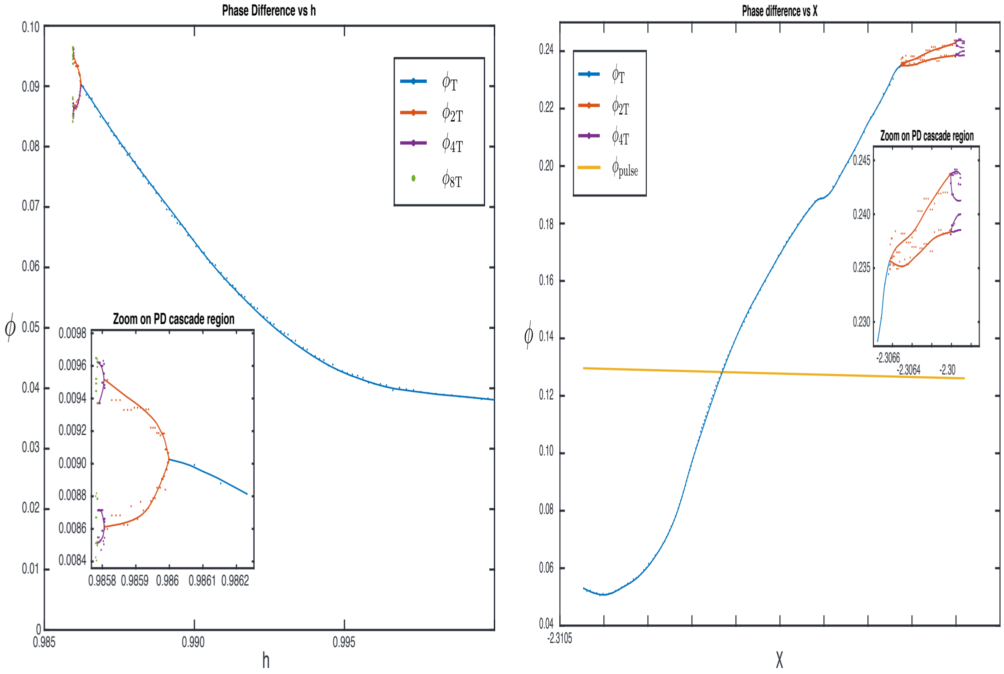

Figure 3.18: Left panel: Phase difference as a function of h for $X = -2.32948, k = 0.1, \alpha_2 = 0.1$. Right panel: Phase difference increases a function of X. $k = 0.1, \alpha_2 = 0.05, h = 0.995$. Yellow line: $\phi^{\#}_{pulse}(X)$.

Table 3.2: Values of the bifurcation parameter h corresponding to the first three period doublings observed in asymmetrically coupled nonidentical oscillators, with fixed X and coupling strengths. The corresponding bifurcation diagram (ϕ vs h) is plotted on the left panel of Figure 3.18.

Bifurcation	X	α_2	h-bifurcation	k
2T-per bifurcation	-2.3294839376	0.1	0.98599842068	0.1
4T-per bifurcation	-2.3294839376	0.1	0.98580725151	0.1
8T-per bifurcation	-2.3294839376	0.1	0.98578593371	0.1

(3.6.2), is fairly close to X^{6D}_{desync} (Table 3.3), the desynchronization time assessed from numerical simulations.

We can further increase the heterogeneity level by coming back to the nominal parameter set of Table 3.1, in which $a_2^{(1)}$ and $a_2^{(2)}$ take different values, and perform a new continuation study of the PD cascades with X as the bifurcation parameter. The results are gathered in Table 3.4 and a specific instance is illustrated in Figure 3.19, with $\alpha_1 = 0.01$ and $\alpha_2 = 0.1$. The PD cascade starts when the phase difference of the stable solution has become high enough ; in particular, the transition from stable T-periodic solutions to 2T-periodic solutions occurs at $\phi_{2T}(X_{PD}) = 0.183$.

In both Figure 3.19 and the right panel of Figure 3.18, the change in $\phi^{\#}_{pulse}(X)$ is superimposed on the bifurcation diagram. We can observe that $\phi^{\#}_{pulse}(X_{PD}) < \phi_{2T}(X_{PD})$, so that the condition to get synchronized pulses is violated at the first PD

Table 3.3: Values of the bifurcation parameter X corresponding to period doublings observed in asymmetrically coupled nonidentical oscillators, for different values of with h and α_2 and $k = 0.1$. X^{6D}_{desync} values are obtained from the numerical simulations of the 6D model within the same parameter setting. An example of bifurcation diagram (ϕ vs X) is given in the right panel of Figure 3.18

Bifurcation	X-PD	α_2	h	X^{6D}_{desync}
2T-per bifurcation	-2.3267594383	0.05	0.9915	-2.324864
4T-per bifurcation	-2.3257944812	0.05	0.9915	
8T-per bifurcation	-2.3256662786	0.05	0.9915	
2T-per bifurcation	-2.3066259724	0.05	0.995	-2.308406
4T-per bifurcation	-2.3060085116	0.05	0.995	
8T-per bifurcation	-2.3059060617	0.05	0.995	
2T-per bifurcation	-2.3172488467	0.07	0.99	-2.318249
4T-per bifurcation	-2.3164597243	0.07	0.99	
2T-per bifurcation	-2.2901528327	0.07	0.995	-2.288059
4T-per bifurcation	-2.2894907062	0.07	0.995	
2T-per bifurcation	-2.3004092512	0.09	0.99	-2.30804
4T-per bifurcation	-2.2997282056	0.09	0.99	
8T-per bifurcation	-2.2996274569	0.09	0.99	
2T-per bifurcation	-2.2748697231	0.09	0.995	-2.266649
4T-per bifurcation	-2.2742695134	0.09	0.995	
8T-per bifurcation	-2.2741717471	0.09	0.995	
2T-per bifurcation	-2.2925375876	0.1	0.99	-2.300774
4T-per bifurcation	-2.2918305299	0.1	0.99	
8T-per bifurcation	-2.2917254798	0.1	0.99	

Table 3.4: X-dependent PD bifurcations in (3.6.2) with the parameter set of Table 3.1, and corresponding X^{6D}_{desync} values. An example of bifurcation diagram (ϕ vs X) is plotted on the right panel of Figure 3.19.

k	α_2	X_{PD}	X^{6D}_{desync}
0.1	0.05	-2.30245	-2.2966
	0.1	-2.2826	-2.2787
	0.2	-2.23483	-2.2423
	0.3	-2.100	-2.205
0.25	0.05	-2.2956	-2.2742
	0.1	-2.26449	-2.2452
	0.2	-2.19011	-2.1926
1	0.05	-2.2461199	-2.18727

bifurcation.

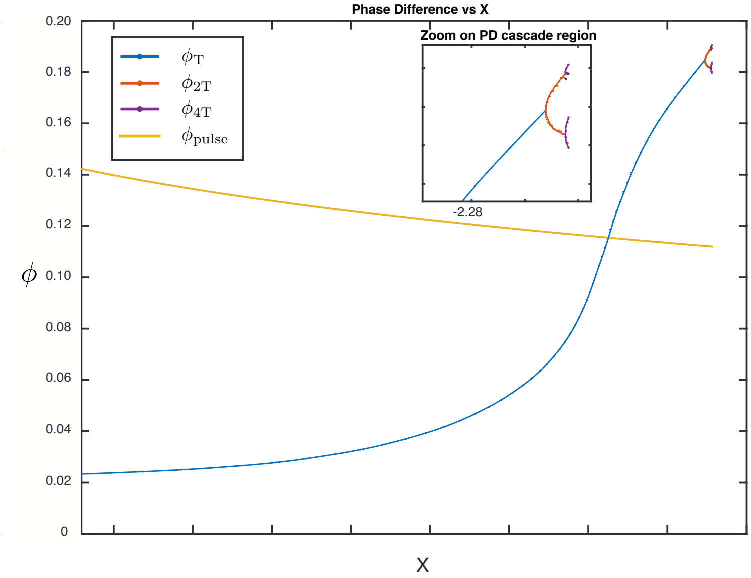

Figure 3.19: Phase difference as a function of X in (3.6.2) with the parameter set of Table 3.1, and $k = 0.1$, $\alpha_2 = 0.1$. Yellow line: $\phi^{\#}_{pulse}(X)$. See the corresponding secretion pattern along a whole ovarian cycle in Figure 3.15.

3.7 Discussion

In this chapter, we have reproduced additional features observed experimentally in the complex secretion pattern of the neurohormone GnRH, namely a two-bump surge and a desynchronization period occurring before the surge triggering. To do so, we have based ourselves on former studies dealing with (i) the quantitative analysis of a 4D, multiple timescale model capturing the main neurosecretory events in GnRH secretion (alternation between a surge and pulsatile regime, together with a time varying pulse frequency), on both the qualitative and quantitative grounds [3], and (ii) a recent work proposing an extended 6D version of this model that was intended to study canard-induced recurrent (de)synchronization in a framework where biological constraints were relaxed in Chapter 2.

We have introduced specific choices of coupling functions and performed a numerical study combined with more analytically-based approaches to assess and tune the quantitative properties of the additional features. Depending on the coupling strengths, a combination of events can be observed, as long as the coupled systems are nonidentical and the coupling terms asymmetric. With constant coupling, either the camel surge (in case of rather strong coupling strengths, see section 2) alone, or desynchronization (in case of weaker coupling strengths, see section 6) alone may occur. We have rather focused on the dynamic coupling, since both events can occur jointly for rather moderate coupling strengths.

In both cases, compared to the initial 4D or 6D models, the direct forcing exerted by the regulatory system (which represents in a compact way the multi-type regulatory neurons conveying the gonadal steroid signal to the GnRH neurons) is completed with an indirect term modulating the interaction term between the secreting systems. This

X-dependent modulation can be further subject to a time varying (state-dependent) sensitivity of the target systems in the case of dynamic coupling. Interestingly enough, such a varying sensitivity has already been used in the context of the modeling of episodic synchronization in individual GnRH neuron activities within a network [79]. Although the model timescale (on the order of the GnRH interpulse interval) in this latter study differs from that of the model considered here (on the order of an ovarian cycle), both dynamics share common features such as the excitability of the elementary systems, the multiple timescale coupling the systems with one another, and the switch induced by a global control exerted onto the secretory systems. We therefore note that the alternation between synchronized and desynchronized regimes resulting from time varying coupling is a key question in both studies.

Inspired from the approach followed in [3], we have intended to delimit proper parameter sets subject to specific quantitative specifications regarding (i) the timing and shape of the camel surge, and (ii) the relative duration of the desynchronized state along the whole ovarian cycle. We have first specified, from the notion of overlapping of individual pulses generated by each secreting system, how we can assess the level of synchronization in our neuroendocrine context, and then deployed a strategy to assess *a priori* the desynchronization time. This strategy is based on either a 4D quasi-static approach taking advantage of timescale separations in the 6D model or a geometric nullcline-based approach. The former is the more accurate, yet it requires numerical simulations. We have also proposed a simple estimation for the surge timing (and more specifically for the timing of the first bump) and exhibited numerical relations between the activation threshold parameter X_{sync} and the coupling strengths, which participate in shaping the surge (ranking of the highest bump). Putting all these pieces together, we have managed to mimic two specific experimental instances of a camel surge, one strictly limited to the surge period, the other encompassing a long pre-surge period including a desynchronization period.

In this study, the systems under study are generally beyond the scope of the weakly coupled oscillator theory. Nevertheless, the situation of constant coupling with symmetric weak coupling strengths, in which we can observe the desynchronization process (in the absence of a camel surge) does not depart much from this framework. Recent works have attempted to extend this theory to systems with slowly varying parameters [63, 64] and they might be adapted to our own system in future work. We have also explored, through numerical continuation with AUTO, the bifurcations induced by the intrinsic, or X-induced heterogeneity in the phase difference dynamics. We have observed the interesting result that the bifurcation point corresponding to the first period doubling provides us with a good approximation of the desynchronization time.

The use of the weakly coupled oscillator theory and numerical continuation are quite restricted in our dynamic coupling framework. The main requirement of this theory is the persistence of the limit cycles under coupling, which is not guaranteed for dynamically coupled secretors which can undergo recurrent bifurcations for large sets of X and coupling strengths. Yet, if the situation is favorable, the H-function analysis can predict the loss of X-dependent phase-locked solutions.

The nonlinear characteristics of the dynamic coupling function, combined with the thresholding of the outputs, restricts the applicability of the numerical continuation. If the steepness of the output signals is decreased, the loss of stability of the synchronized solutions can be detected via PD bifurcations in appropriate settings corresponding to the 4D quasi-static model. However, it remains difficult to link these bifurcation points to values of desynchronization times. Detailed investigation of these bifurcation structures can also be an interesting research track.

Finally, in this work, we have modeled camel surges and pulse desynchronization by extending both the dimension of the system (and considering subpopulations of secreting neurons, hence some level of heterogeneity in the GnRH network) and the impact of the regulatory signal, while keeping the compact modeling approach of the 4D system initially designed on the macroscopic level. Our choices of specification-oriented coupling functions have not only the advantage of enabling the model to reproduce additional features of the GnRH secretion, but they also raise interesting mathematical questions, such as the issue of dynamic bifurcations in coupled bursters, and give some insight on them.

3.8 Appendix: Weakly coupled heterogenous oscillators

Consider the following system

$$\frac{dX_i}{dt} = F(X_i) + \frac{\Delta f_i(X_i)}{2} + \alpha I(X_j, X_i)$$

involving two coupled oscillators,$i = \{1, 2\}$ and $j = 3 - i$, with weak heterogeneity $\frac{\Delta f_i(X_i)}{2}$ and weak coupling $\alpha I(X_j, X_i)$. In the absence of coupling, homogeneous systems each follow a limit cycle X_{LC} with T-period. The phase shift from X_{LC} induced by weak heterogeneity and coupling over a T period is given by

$$\frac{d\theta_j}{dt} = \frac{1}{T}\int_0^T Z(\tilde{t})\left\{\alpha\left[I(X_{LC}(\tilde{t}), X_{LC}(\tilde{t} + \theta_k - \theta_j))\right] + (-1)^j \frac{\Delta f_j(X_j(\tilde{t}))}{2}\right\} d\tilde{t} \tag{3.8.1}$$

where $Z(\tilde{t})$ corresponds to the infinitesimal phase response curve (iPRC), solution of adjoint equation:

$$\frac{dZ(t)}{dt} + A(t)^T Z(t) = 0$$

which satisfies a normalization condition $Z(t)\frac{dX_{LC}(t)}{dt} = 1$, where $A(t) = D_X F(X)|_{X_{LC}(t)}$ is the linearization of $F(X_j)$ around the limit cycle X_{LC}.

Given the phase difference between oscillators $\phi = \frac{1}{T}(\theta_k - \theta_j)$, the *interaction function* for the i-th oscillator, $H_i(\phi)$ can be extracted from (3.8.1) as

$$H_i(\phi) = \frac{1}{T}\int_0^T Z(\tilde{t})\left\{\left[I(X_{LC}(\tilde{t}), X_{LC}(\tilde{t} + \theta_k - \theta_j))\right]\right\} d\tilde{t}.$$

Finally, the phase difference dynamics reads

$$\frac{d\phi}{dt} = \alpha(H_j(-\phi) - H_i(\phi)) + \frac{1}{T}\int_0^T Z(\tilde{t})\Delta f_j(X_j(\tilde{t}))d\tilde{t} = \alpha G(\phi) + \Delta w Q.$$

where Q is the averaged iPRC over the period T and Δw is the intrinsic frequency difference.

Chapter 4

Synchronization of weakly coupled canard oscillators

Elif Köksal Ersöz [1], Mathieu Desroches [2] and Martin Krupa [2]

Submitted to a peer-reviewed journal

Abstract

Synchronization has been studied extensively in the context of weakly coupled oscillators using the so-called phase response curve (PRC) which measures how a change of the phase of an oscillator is affected a small perturbation. This approach was linked to the work of Malkin, and it has been extended to relaxation oscillators. Namely, synchronization conditions were established under the weak coupling assumption, leading to a criterion for the existence of synchronous solutions of weakly coupled relaxation oscillators. Previous analysis relies on the fact that the slow nullcline does not intersect the fast nullcline near one of its fold points, where canard solutions can arise. In the present study we use numerical continuation techniques to solve the adjoint equations and we show that synchronization properties of canard cycles are different than those of classical relaxation cycles. In particular, we show that maximal canards separates two distinct synchronization regimes: the Hopf regime and the relaxation regime. Phase plane analysis of slow-fast oscillators undergoing a canard explosion provides an explanation for this change of synchronization properties across the maximal canard.

AMS

34C15, 34C26, 34D06, 34E17, 92C20

---

[1] INRIA Paris Research Centre, MYCENAE Project-Team, 2 Rue Simone Iff, CS 42112, 75589 Paris cedex 12, France.

[2] INRIA Sophia Antipolis Méditerranée Research Centre, MathNeuro Team, 2004 route des Lucioles - BP93 06902 Sophia Antipolis cedex, France.

Keywords

Canards, phase response curves, slow-fast systems, synchronization, weak coupling

4.1 Introduction

Synchronization is a research topic of its own, which has produced a large body of knowledge in particular for so-called weakly coupled oscillators [51, 76, 65, 72, 33, 77, 50, 52, 48, 49]. A classical object of interest in this context is the *(infinitesimal) phase response curve* or *(i)PRC* which encodes how a small perturbation affects the phase of an oscillator when applied all along the associated stable limit cycle solution. The derivation of the PRC relies on the linearization of the system along the unperturbed (i.e. uncoupled) cycle and is closely related to the adjoint variational equation. Solutions to the adjoint problem and PRCs give insights on the synchronization properties of coupled oscillating systems [33, 49] when the coupling strength is small enough. Such studies are gathered under the name "weakly coupled oscillator theory" [48]. This theory has been linked with earlier studies from Malkin [58, 59] by Izhikevich and Hoppensteadt in [60, 48]; an explicit proof was given in [98] by connecting it the work of Roseau [99, 100].

Weakly coupled oscillator theory has been used in many studies, especially to investigate the effects of slowly-varying parameters, underlying bifurcations and coupling strengths on collective dynamics. In one of the pioneer papers on this topic [72], out-of-phase (OP) synchronization (intermediate modes between in-phase (IP) and anti-phase (AP) solutions) was shown to emerge from a pitchfork bifurcation in the phase difference as a function of the coupling parameter. A similar bifurcation structure has been found in type-I spiking neuron models, see e.g. [101, 102, 52]. Another recent study related to type-I membranes [103] focused on the transition from IP to OP synchronous states in chains of Wang-Buszaki models coupled by gap junctions. This transition was investigated both analytically and numerically as a function of intrinsic system properties by using phase models and interaction function. In the framework of type-II neuron models, the impact of the Hopf bifurcation on the possible synchronization patterns has been studied, e.g., in [96, 104, 105, 51, 50]. Furthermore, variations of the PRC across a Hopf bifurcation were analyzed in cortical excitatory neuron models in [55]. Qualitative changes in the behavior of the PRC were also looked at directly from experimental data in [106] and [107] where the interaction functions were analyzed during the transition from Hopf and relaxation oscillators. The existence of different synchronization modes and of bistable regions in weakly coupled slow-fast systems interacting via gap junctions has been underlined in [108, 109, 110, 111, 112, 102, 71, 46, 113, 56].

Slow-fast oscillators are an important source of complicated dynamics, in particular in relation to the canard phenomenon (detailed in Chapter I). In (weakly) coupled slow-fast systems, the effect of canard solutions has been considered in several aspects such as the formation of clusters, synchrony, phase and amplitude dynamics [39, 40, 41, 27, 42]. In Chapter 2, we have investigated canard-mediated variability in coupled phantom bursting systems addressing issues on synchronization and desynchronization.

In this chapter we extend previous results on adjoint solutions and weakly coupled slow-fast oscillators to the case of canard cycles. Analytical formulations of adjoints and interaction functions were studied in [54], which also provides a review of the behavior near bifurcation points. In the framework of relaxation cycles, an expression for the adjoints could be obtained in [60] by taking the singular limit approximation, considering the attracting branches of the critical manifold in place of the slow segments of relaxation cycles, and instantaneous jumps in place of fast segments. The consequence of using this setup is that the canard regime has not been dealt with. In the present study, we propose an alternative numerical strategy, based on numerical continuation, for the computation of solutions to the adjoint variational equation associated with planar slow-fast systems along a canard explosion.

In parameter space, canards organize the transition between the Hopf regime and the relaxation regime. Therefore we may expect to link the synchronous behavior between these two families [106, 107] by computing adjoints for canard solutions. When performing such computations, we observe a qualitative change in the sign and shape of the adjoint (or equivalently, of the iPRC) near the *maximal canard* (the cycle with the longest repelling segment). This phenomenon occurs in both canard-explosive systems that we consider here, namely the van der Pol (VDP) oscillator and a two-dimensional (2D) reduction of the Hodgkin-Huxley (HH) model. We propose an explanation to this qualitative change through the period function of the canard family which has a non-monotonic behavior across the explosion, namely, it increases during the headless-canard regime and it decreases during the canard-with-head regime. Similar dependence of the frequency upon a bifurcation parameter has been studied in [114] in the context of "escape-release" mechanisms of central patterns generators. The authors of [115] have then linked this dependency to transitions in PRCs and phase-locking properties occurring in the low-frequency region.

In the second half of this work, we explore the dependency of the phase difference between the two weakly coupled identical VDP systems on system parameters. By investigating effect of the main parameter displaying the canard explosion, we observe that the transition in synchronization properties occurring at the maximal canard of the coupled system manifests itself as the AP synchronization state loses its stability through a pitchfork bifurcation in the phase difference. Furthermore, we reveal the presence of $2nT$-periodic synchronous states in the maximal canard neighborhood due to the presence of multiple period-doubling (PD) bifurcations. Finally, we consider the effect of the coupling strength on the synchronous states in the maximal canard regime. We give numerical evidence of the presence of PD cascades not predicted by the theory of weakly coupled oscillators (which is valid for moderate coupling strengths in various systems [52, 116]) but that can be justified using phase plane analysis of the single canard oscillators under scrutiny. We also propose in an analytical formula to compute adjoints associated with limit cycles of slow-fast systems in Liénard systems, which gives satisfactory yet improvable results.

This chapter is organized as follows. In Section 4.2, we introduce the main objects required to compute adjoint solutions along a limit cycle and we present our numerical strategy to do so along families of canard cycles. In Section 4.3, we analyze numerically the effect of the main parameter c on the synchronous states of the coupled VDP system and report a qualitative change occurring near the maximal canard solution. We then explain this change by invoking the properties of the period function associated with such a canard-explosive branch of limit cycles. In Section 4.4, we focus on the effect of the coupling strength parameter α on the synchronous structure in the coupled VDP system near a maximal canard. After concluding and proposing a few perspectives to this work, we present in Appendix 4.6 an analytical formula to compute adjoint solutions for the type of systems we investigated here and test this formula numerically.

4.2 Computations of adjoint solutions along a family of cycles

Canard explosions occur in slow-fast systems in a very narrow parameter range which is exponentially small in the timescale separation parameter $0 < \varepsilon \ll 1$. Naturally, this parameter range gets narrower as ε tends to 0, and limits the usage of classical tools to compute family of canard orbits and their adjoint solutions. Thus, in addition to the existing methods, such as backward integration, we propose an alternative strategy based on numerical continuation and performed using the software package AUTO [117]. We formulate a periodic continuation problem which allows us to compute rapidly and reliably a family of cycles with associated non-trivial periodic solution of the adjoint equation. Note that a boundary-value problem (BVP) approach has been proposed in [118], outside a continuation setup given that the system was with reset. Here, for simplicity, we avoid dealing specifically with boundary conditions and opt for the most natural periodic setting of this numerical problem. An extension of the analytic approach for solving adjoint variational equations in slow-fast systems is given in Appendix 4.6.

4.2.1 Numerical continuation alternative for adjoints

The numerical continuation approach proposed in the present work allows us to compute limit cycles and associated adjoint solutions along a canard-explosive branch. One of the main advantages of the continuation is the possibility to find solutions in the limit $\varepsilon \to 0$. We extend the continuation setting of the original system (1.3.1), solved in order to find limit cycles, by including equation (1.3.2) (once written in first-order form) to find periodic solutions of the adjoint problem along these cycles. In order to compute a limit cycle γ together with a periodic solution of the associated adjoint problem along γ, one needs to solve the following system of equations

$$\begin{aligned} \dot{X} &= F(X), \\ \dot{Z} &= -D_X F(X)^T_{|\gamma} Z. \end{aligned} \tag{4.2.1}$$

Our numerical continuation strategy requires two steps: first, to find a non-trivial solution of the adjoint problem along the (initial) cycle γ, and second, to follow the extended system (4.2.1) (as a periodic continuation problem) in a bifurcation parameter in order to find a branch of such solutions. In the following section we describe these steps by considering two examples of coupled slow-fast systems in the canard regime, namely, the VDP system and and a two-dimensional reduction of the HH model for action potential generation whose slow-fast structure and associated canard dynamics were analyzed in [23].

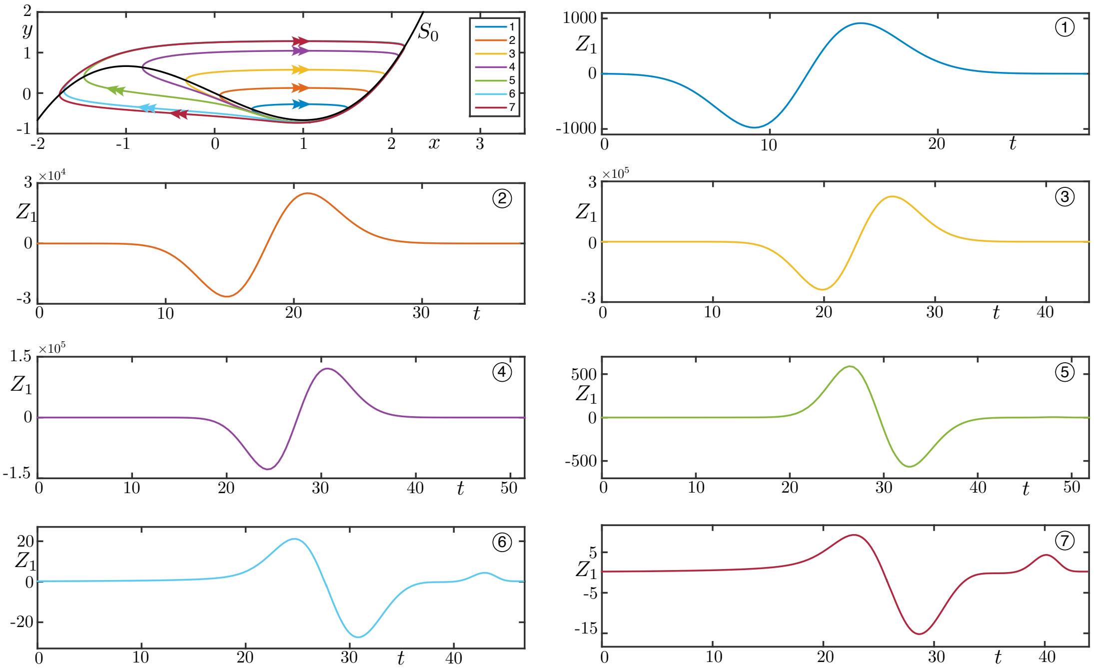

Figure 4.1: Top left panel: Canard orbits of the VDP system in the phase plane, for $\varepsilon = 0.1$. Panels 1-7: time profile of the first component of the adjoint solution associated with each canard cycle shown in the phase plane (together with the critical manifold $S_0 := \{y = f(x)\}$), keeping the same color coding with the cycles in the top left panel. A qualitative change in the adjoint solution occurs in between Orbit 4 and Orbit 5, corresponding to the passage through the maximal canard cycle.

a Adjoint solutions of the VDP system

In the case of the VDP system, the extended continuation setting (4.2.1) reads

$$\begin{aligned} x' &= y - f(x) \\ y' &= \varepsilon(c - x) \\ z_1' &= f'(\gamma_1(t))z_1 + \varepsilon z_2 \\ z_2' &= -z_1, \end{aligned} \tag{4.2.2}$$

with $f(x) = x^3/3 - x$, $0 < \varepsilon \ll 1$ and c is the bifurcation parameter displaying the canard explosion. That is, we consider the original VDP system with the adjoint equation appended to it. As hinted at above, the continuation procedure is divided into two steps.

In the first step, we initialize system (4.2.2) with the limit cycle γ for the first two equations, and the trivial solution for the remaining two (which is trivially periodic). We need to obtain a non-trivial periodic solution of the adjoint equation, and we can find this solution by continuing system (4.2.2) in an extra parameter. Indeed, given that the trivial solution to the adjoint equation exists for all values of parameters c and ε, by continuing in any of these we can only hope to find a branch point and switch at this bifurcation to the non-trivial solution branch. An alternative is to introduce a dummy parameter μ, such that system (4.2.2) becomes

$$\begin{aligned} x' &= y - f(x) \\ y' &= \varepsilon(c - x) \\ z_1' &= f'(\gamma_1(t))z_1 + \varepsilon z_2 \\ z_2' &= -z_1 + \mu, \end{aligned} \tag{4.2.3}$$

and to continue the starting solution in μ along a very small interval, as small as possible. It turns out that we can compute a branch in μ and stop at $\mu = 10^{-8}$, which is indeed very small but sufficient to find a non-trivial solution of the extended problem (4.2.3).

Given that μ is very small, we can, in the second step, impose back $\mu = 0$ and run a simple Newton iteration so as to converge to a non-trivial solution of the original extended problem (4.2.2). The advantage of using numerical continuation to compute a non-trivial solution to the adjoint equation along a canard cycle is that we can then continue the extended problem (4.2.2) in parameter c and follow both the cycle and the associated periodic solution of the adjoint equation along the entire canard explosion. Finally, the normalization condition (1.3.3) is required to close to the linear problem corresponding to the adjoint equation. Implementing this condition as part of our numerical continuation procedure can be a little delicate for small values of ε, therefore we decided to use a periodic continuation in AUTO and apply the scaling that corresponds to (1.3.3) as a post-processing step. Note that we refrain from computing the Floquet bundle to obtain the non-trivial solution of the adjoint equation for this numerical problem since we only need any non-trivial solution to the adjoint equation, which we can then normalize appropriately.

Starting from the Hopf bifurcation all the way to the relaxation regime, we can therefore follow the canard cycles by varying c together with their associated adjoint solutions. Figure 4.1 shows some of the orbits lying in the headless canard and in the canard with head regimes. We observe a qualitative change in the adjoint solution as the limit cycle γ passes through the maximal canard.

In order to see whether or not the transitions that we observe in coupled VDP oscillators are system dependent, we next compute adjoint solutions associated with canards in a planar reduction of the HH model.

b Adjoints of canard cycles in a reduced Hodgkin-Huxley model

A reduction of the classical HH model to two variables was analyzed from the viewpoint of canard dynamics in [23]; the planar system has the form

$$\begin{aligned} \dot{V} &= (I - \bar{g}_{Na}[m_\infty(V)]^3(0.8 - n)(V - V_{Na}) - \bar{g}_K n^4(V - V_K) - g_L(V - V_L))/C \\ \dot{n} &= \alpha_n(V)(1 - n) - \beta_n(V)n, \end{aligned} \tag{4.2.4}$$

where $\alpha_n(V) = (0.01(V + 55))/(1 - \exp[-(V + 55)/10])$, $\beta_n(V) = 0.125\exp[-(V + 65)/80]$, $m_\infty(V) = \alpha_m/(\alpha_m+\beta_m)$ with $\alpha_m = (0.1(V+40))/(1-\exp[-(V+40)/10])$, $\beta_m = 0.4\exp[-(V + 65)/18]$). Moehlis showed in [23] that system (4.2.4) displays a canard explosion when parameter I is varied, for the following fixed values of the other parameters: $\bar{g}_{Na} = 120$, $\bar{g}_K = 36$, $\bar{g}_L = 0.3$, $V_{Na} = 50$, $V_K = -77$, $V_L = -54.4$, $C = 1$.

Moehlis verified numerically that the dynamics of V are much faster than the dynamics of n. Given that the system plays slow-fast dynamics, a formal asymptotic analysis was performed in ε which appeared in the re-written form of the slow equation ($\dot{n} = \varepsilon(\alpha_n(V)(1-n) - \beta_n(V)n)$) in [23]. After treating ε as a small parameter in asymptotic analysis, $\varepsilon = 1$ was plugged in the final formula. In particular, an ε-expansion of the I-value at which the canard explosion occurs was obtained.

Despite the instability of part of the canard branch in system (4.2.4), the continuation strategy allows to find solutions to adjoint equations. Since we are interested in the shape of the adjoints of the canard cycles lying on different sides of the repelling slow manifold, we can ignore the stability issue. Following the same continuation procedure described above, we compute adjoints of the 2D reduced HH system. Canard cycles and corresponding adjoint solutions are visualized in Figure 4.2. As in the VDP system, the transition from headless canards to canards with head changes qualitatively the adjoint solution.

4.2.2 Consequences of a non-monotonic period function on the iPRC

As shown in Figure 4.3, the period function is non-monotonic along the canard explosion. Starting from the Hopf bifurcation point $c_{Hopf} = 1$, it increases in the headless

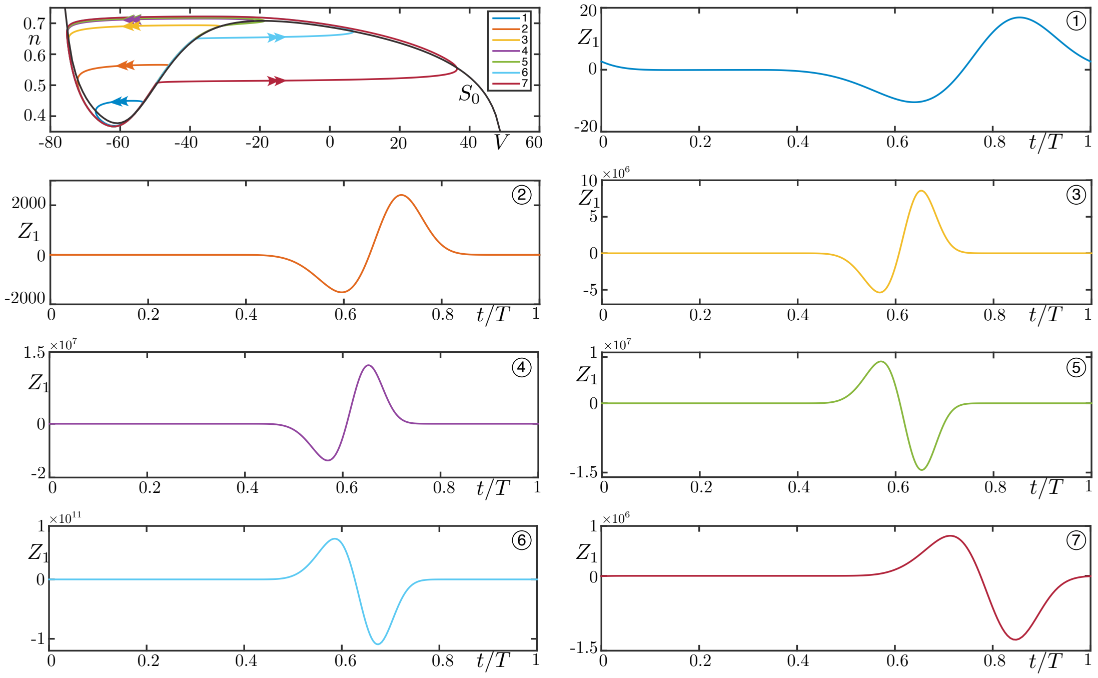

Figure 4.2: Top left panel: Canard orbits of the reduced HH system in the phase plane. Panels 1-7: time profile of the first component of the adjoint solution associated with each canard cycle shown in the phase plane (together with the critical manifold $S_0 := \{\dot{V} = 0\}$), keeping the same color coding with the cycles shown in the top left panel. A qualitative change in the adjoint solution occurs in between Orbit 4 and Orbit 5, corresponding to the passage through the maximal canard cycle.

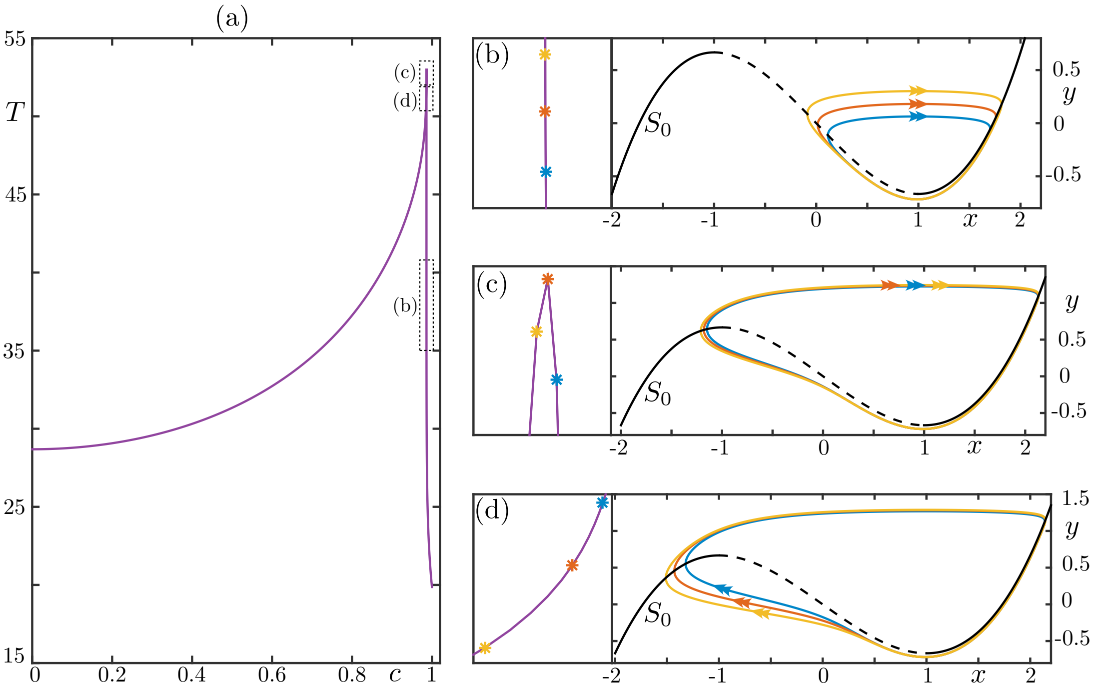

Figure 4.3: (a) Period of limit cycles along the canard explosion in the VDP system for $\varepsilon = 0.1$; the parameter that varies is c in a decreasing fashion. The period is increasing along the headless canard part of the branch, it reaches its maximum at the maximal canard and then decreases along the canard-with-head cycles. (b) Three headless canard cycles and their periods marked on the period curve. Smaller cycles have smaller periods. (c) Three cycles in the neighborhood of the maximal canard, together with their periods marked on the period curve. Canards with head and headless canards have very close periods in this vicinity. (d) Three canards with head and their periods marked on the period curve. Larger cycles have smaller periods. Also shown on panels (b) to (d) is the critical manifold S_0, on which solid (resp. dashed) parts represent stable (resp. unstable) branches.

canard regime, reaches its maximum at the maximal canard and then decreases in the canard-with-head regime as c parameter decreases. The non-monotonicity of the period function along the explosive branch of canard cycles is one key aspect of the canard phenomenon in VDP-type systems, and the maximum of the period function can be used to detect numerically the maximal canard [119]. The shape of this period function is sufficient to understand the effect of a perturbation of a canard cycle close enough to the lower fold of the critical manifold S_0. Indeed, $O(1)$ away from this fold point, a sufficiently small perturbation from the slow manifold takes the perturbed trajectory back to it very rapidly and therefore the effect of this perturbation is largely attenuated. This justifies that the solution to the adjoint equation along a canard cycle is close to zero for most of the cycle apart from the time interval corresponding to when the cycle is close to the lower fold (where the canard point is). On the other hand, near the lower fold of the critical manifold, the attraction to the slow manifold associated to the chosen canard cycle is weaker and the effect of the perturbation becomes large; see Figure 4.4(a2),(b2) for an illustration of this point. This effect can be understood by invoking the period function of the branch of canard cycles.

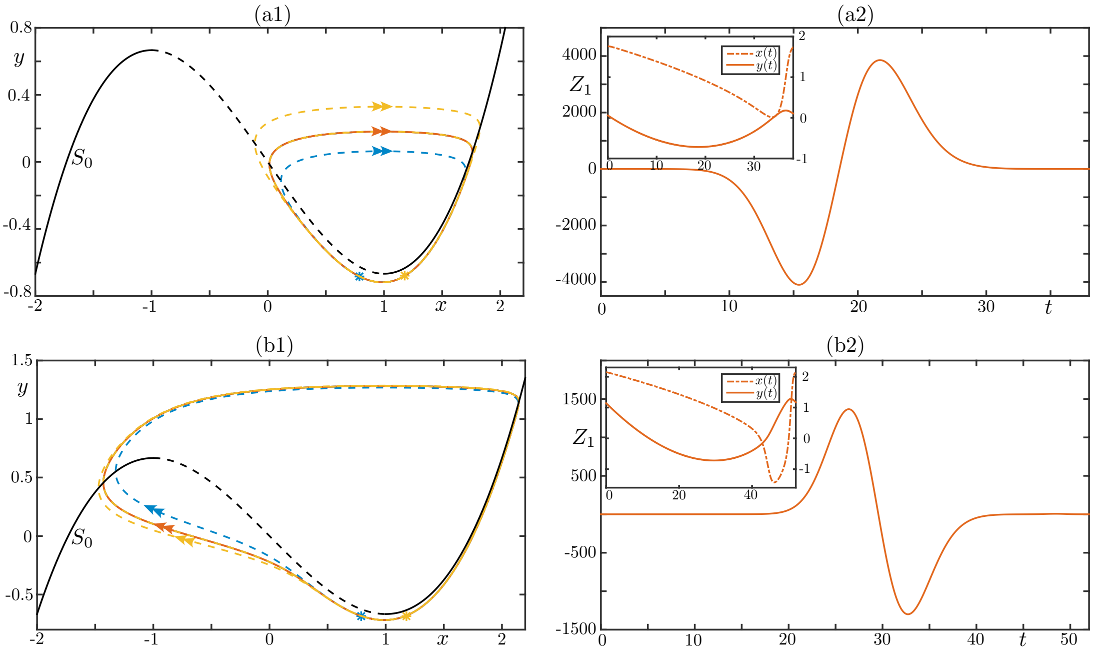

Figure 4.4: (a1, b1) Transient effect (dashed curves) of a small perturbation of the canard cycles (red solid curves) in the positive x-direction. (a2)-(b2) time profile of the first component of the adjoint solution associated with the red canard cycles and (inset) $(x(t), y(t))$ during one cycle. Perturbing a headless canard (resp. a canard with head) away from the attracting slow manifold (perturbation in the positive direction shown by the yellow asterisk) advances (resp. delays) its phase by driving it to a larger yet slower (resp. faster) yellow dashed cycle. Perturbing a headless canard (resp. a canard with head) away from the repelling slow manifold (perturbation in the positive direction shown by blue asterisk) delays (resp. advances) its phase by driving it to a smaller yet faster (resp. slower) blue dashed cycle.

First, consider headless canard cycles as represented in Figure 4.3(b). If we denote the period of the red cycle by T_{red}, then smaller canard cycles than the red one, like the blue cycle, have smaller periods whereas larger headless canard cycles, like the yellow one, have greater periods. Hence we have: $T_{blue} < T_{red} < T_{yellow}$. Therefore, an infinitesimal kick in the x direction applied on the slow attracting segment of the red headless canard cycle near the fold (yellow dot in Figure 4.4(a1)) has the effect that the perturbed trajectory follows transiently a larger headless canard cycle (like the yellow one) before converging back to the red cycle. Given that the yellow cycle has a larger period, the perturbed trajectory's phase is delayed compared to the unperturbed one. Applying such a kick on the slow repelling side of the red headless canard (blue dot in Figure 4.4(a1)) has the opposite effect given that in this case the perturbed trajectory first follows a smaller canard and, hence, has an advanced phase compared to the unperturbed one. Consequently, this qualitative argument justifies the sign of the adjoint solution along a headless canard cycle as shown in Figure 4.4(a2). As it can be followed from the $(x(t), y(t))$ flow given in the inset of Figure 4.4(a2), the negative part of the adjoint corresponds to the flow towards the fold point. The sign of the adjoint solution changes at the fold ($x = 1$), then the positive part appears as $(x(t), y(t))$ flows away from the fold. The situation for canards with head is entirely reversed: the period function is decreasing along the family of canards-with-head, hence three canards-with-head as shown in Figure 4.3(d) (blue, red, and yellow) have their periods satisfying the inequalities $T_{blue} > T_{red} > T_{yellow}$. Consequently, a similar phase plane argument as given above justifies that an infinitesimal kick on a canard with head on its slow attracting segment near the fold leads to a phase advance of the perturbed trajectory, whereas on the slow repelling segment it leads to a phase delay. This agrees with the adjoint solution computed along a canard with head and plotted in Figure 4.4(b2). Solutions $(x(t), y(t))$ given the inner panel of Figure 4.4(b2) confirms that, indeed, the solution of adjoint takes positive values along the flow towards the fold, changes its sign at ($x = 1$), then becomes negative as $(x(t), y(t))$ move away from the fold region. Note that invoking the period function to explain a change of shape and sign of the adjoint solution has been used in [115] in the context of so-called escape-release mechanism for the synchronization of half-center oscillators. Here we show that it also applies in the context of coupled canard oscillators.

4.3 Synchronization properties of weakly coupled canard oscillators

The behavior of the adjoint solutions (or equivalently, of the iPRCs) provides one with predictions on the collective behavior in the weak coupling regime via the interaction function (1.3.4). The dynamics of the phase difference are described in (1.3.5).

IP synchronization of two identical relaxation cycles (coming from oscillators with cubic-shaped fast nullclines) that are weakly coupled via fast to fast (FF) connections has been shown in [43, 71, 60, 46, 47, 111], outside the canard regime. In addition to FF coupling —which is the coupling function generally considered since it acts as a prototype for the electrical interaction between neuronal systems— we consider fast to slow (FS) coupling, which is not physiologically realistic but provides insight into understanding the interactions between perturbation and canards. The FF-coupled VDP oscillators read:

$$\begin{aligned} \varepsilon \dot{x}_i &= y_i + x_i - \frac{x_i^3}{3} + \alpha(x_j - x_i), \\ \dot{y}_i &= (c - x_i), \end{aligned} \tag{4.3.1}$$

and the FS-coupled system is given by

$$\begin{aligned} \varepsilon \dot{x}_i &= y_i + x_i - \frac{x_i^3}{3}, \\ \dot{y}_i &= c - x_i + \alpha(x_i - x_j). \end{aligned} \tag{4.3.2}$$

The effect of a small perturbation on the canard cycles in the neighborhood of the lower fold of the critical manifold S_0, is different for canards with head than for headless canard cycles, as revealed by the corresponding adjoint solutions; see Figure 4.1. This

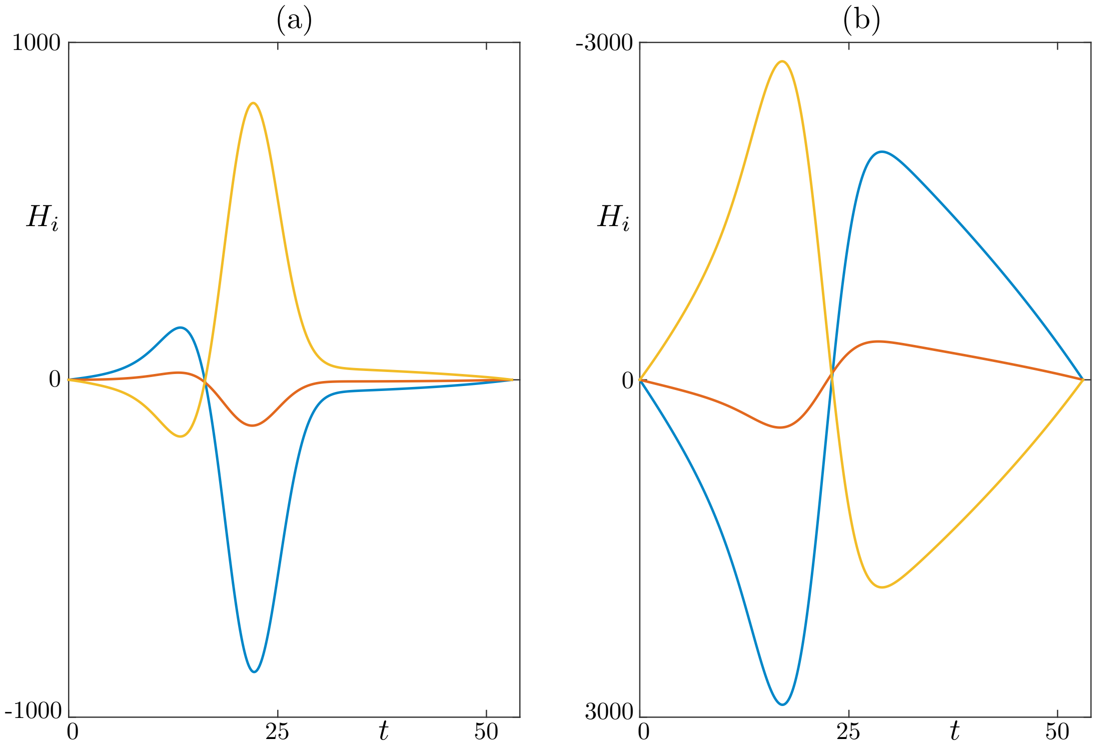

Figure 4.5: Time profile of the functions H_i in the maximal canard neighborhood given in Figure 4.3 (c) for FF (panel (a)) and FS (panel (b)) coupling functions. The properties of H_i reflect what is found for the solutions of the adjoint equation, i.e. the transition occurs in the neighborhood of the maximal canard.

qualitative change occurs at the maximal canard. Figure 4.5 shows the interaction functions H_i (depending on $t \in [0, T]$ with $\phi = t/T$) associated with the cycles in the neighborhood of the maximal canard (shown in Figure 4.3 (c)) interacting via FF (panel (a)) and FS (panel (b)) connections. Given that a headless canard cycle resembles more the maximal canard (the maximal canard being a maximal headless canard), the amplitude of the corresponding function H_i decreases while the number of zeros, t^*, and the sign of $H_i'(t^*)$ remain the same. The sign of $H_i'(t^*)$ changes when the cycle moves to the canard-with-head regime, while the number of zeros t^* is preserved.

The function G (depending on $\phi \in [0, 1]$, see Figure 4.6) is computed for the cycles (whose adjoints are presented in Figure 4.1) interacting via FF coupling and its behavior is in consistency with the qualitative changes we observe in the solution of adjoints. The location of the zeros ϕ^* of G, and the sign of its derivative at such points, determine the type and stability of synchronized state of the coupled system. The IP synchronized solution which exists for the Hopf cycles (not shown on this figure) loses stability along the canard explosion (due to the high sensitivity to perturbation resulting from the passage near the fold of the critical manifold S^0) and a stable OP solution appears for the headless canard cycles (orbits 1-4). The phase difference of the stable OP solution increases as the cycle approaches the maximal canard (Panels 1-4, $\phi^* = 0.18$ for orbit-1 and $\phi^* = 0.32$ for orbit-4). Bistability appears for the

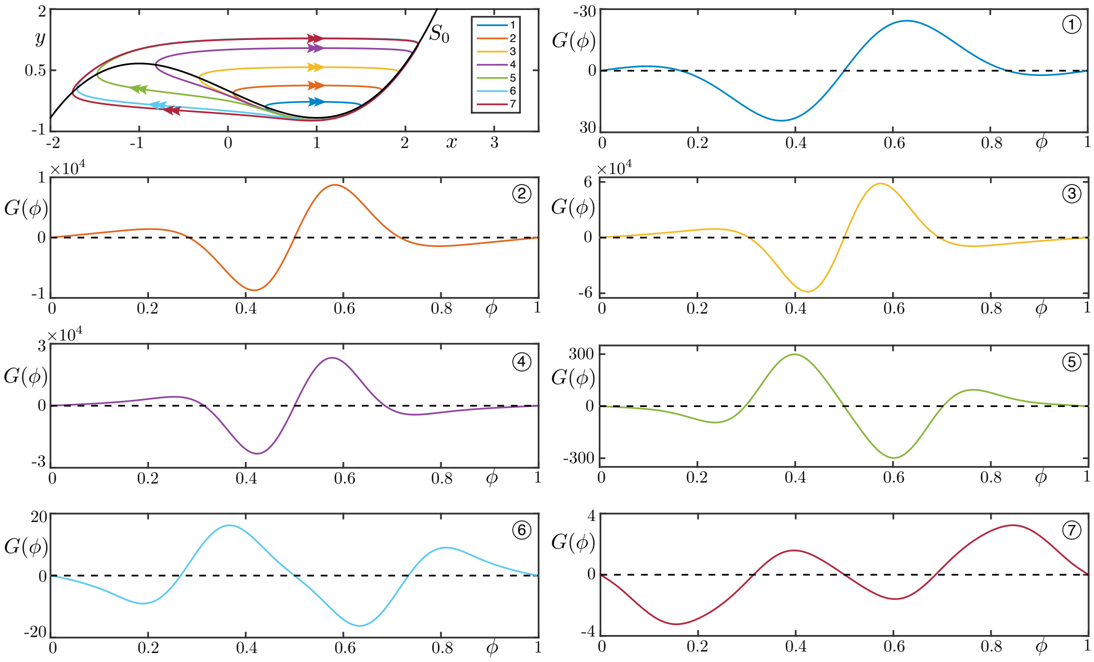

Figure 4.6: Selection of canard cycles of the VDP oscillator in the phase plane (x, y) (top left panel) together with the corresponding G functions (panels 1 to 7; the phase ϕ is rescaled to [0,1]).

canards-with-head (orbits 5-7), where IP and AP solutions are the stable synchronous solutions and the OP is the unstable solution (Panels 5-7).

The information obtained with the function G about synchronized states of the weakly coupled VDP system with FF coupling, can be confirmed by a numerical bifurcation analysis of the coupled system in question. We have performed this analysis by continuing synchronous states of system (4.3.1) (including the ones which are not visualized in Figure 4.6) in parameter c. The result is presented in Figure 4.7 where the chosen solution measure is the difference between the x-component of each oscillator at time $t = 0$, $x_2(0) - x_1(0)$, regardless of its varying amplitude as a function of c. That measure has the same interpretation as the phase difference for these simple orbits and it is often used in the analysis of weakly coupled oscillators [72]. Panels (b) to (d) are successive zooms of panel (a) in the region corresponding to maximal canards for each oscillator. The properties of the synchronized states of the FF-coupled cycles are tracked starting from the double Hopf bifurcation point at $c = c_{Hopf} = 1$ down to the relaxation regime near $c \approx 0.615$. We consider a fixed coupling strength $\alpha = 10^{-5}$ for which the weakly coupled oscillators theory is expected to be valid; a detailed discussion on the effect of α is presented in Section 4.4. One stable and two (symmetric) unstable branches, which correspond to IP and AP solutions, respectively, appear at $c{=}c_{Hopf}$. The IP solution undergoes a pitchfork bifurcation through which it loses its stability as a stable OP solution appears (Panel (b)). The OP branches become unstable at a PD bifurcation which is followed by a PD cascade corresponding to $2nT$-periodic stable synchronous solutions (Panel (d)), where the interaction function

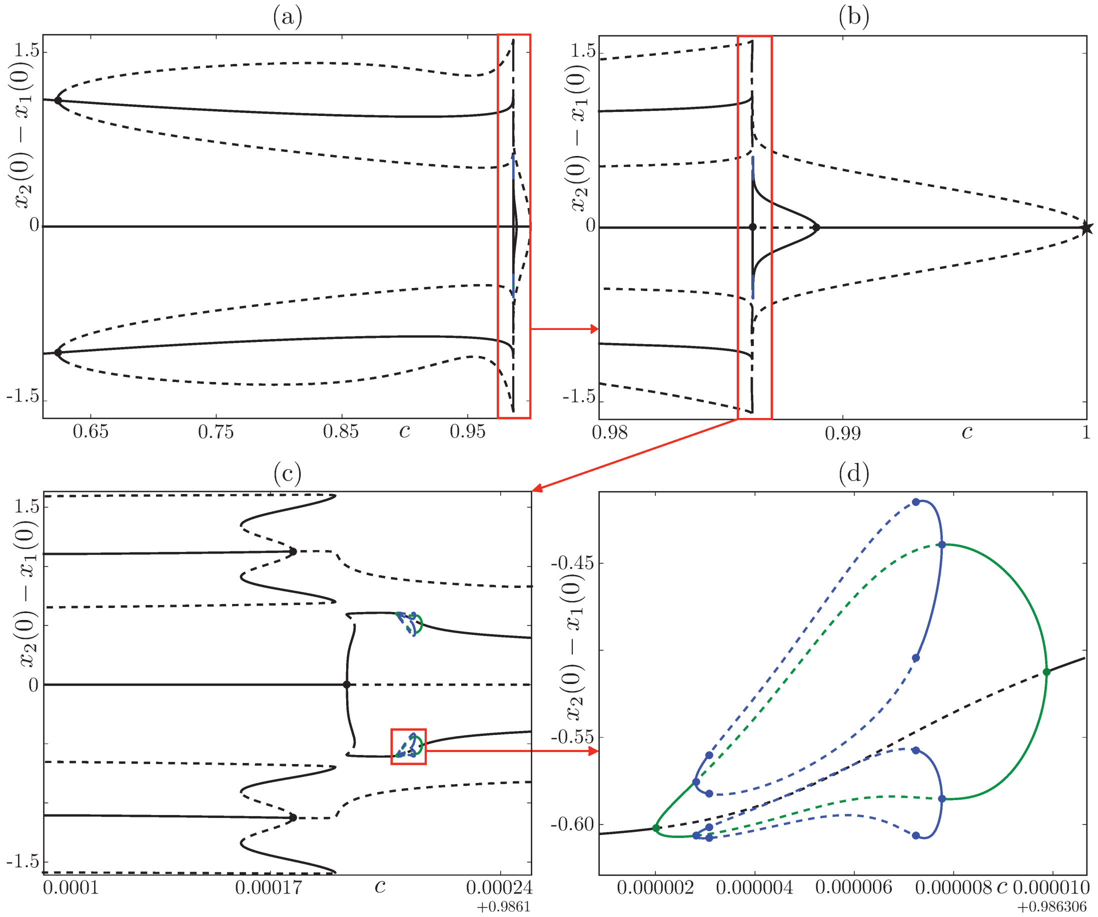

Figure 4.7: Bifurcation diagram of system (4.3.1) with respect to variations of c for $\alpha = 10^{-5}$, from the Hopf regime to the relaxation regime. The output solution measure is the difference between the first components of each oscillator at time $t = 0$. The region of the maximal canard is enlarged from left to right and top to bottom panels. Black dots in panels (a) to (c) denote pitchfork bifurcation points; the black star in panel (b) corresponds to the double Hopf point that initiate the periodic regime in this coupled system; colored dots in panel (d) denote PD bifurcation points.

analysis is not valid. The T-periodic OP branches become stable again via a second PD bifurcation. It changes its stability two times via a couple of fold bifurcations before connecting to the second pitchfork bifurcation point on the IP branch that restabilizes the IP state.
The unstable AP branch that appears at c_{Hopf} becomes stable at the maximal canard of the coupled system through a pitchfork bifurcation (Panel (c)). The stable AP and OP solution related to this pitchfork bifurcation coexist with stable IP solutions for a some range of c in the neighborhood of the maximal canard. For smaller values of c, IP and AP remain stable, while OP states are unstable.

The bistability regions (illustrated in Figure 4.8) already hinted at with the in-

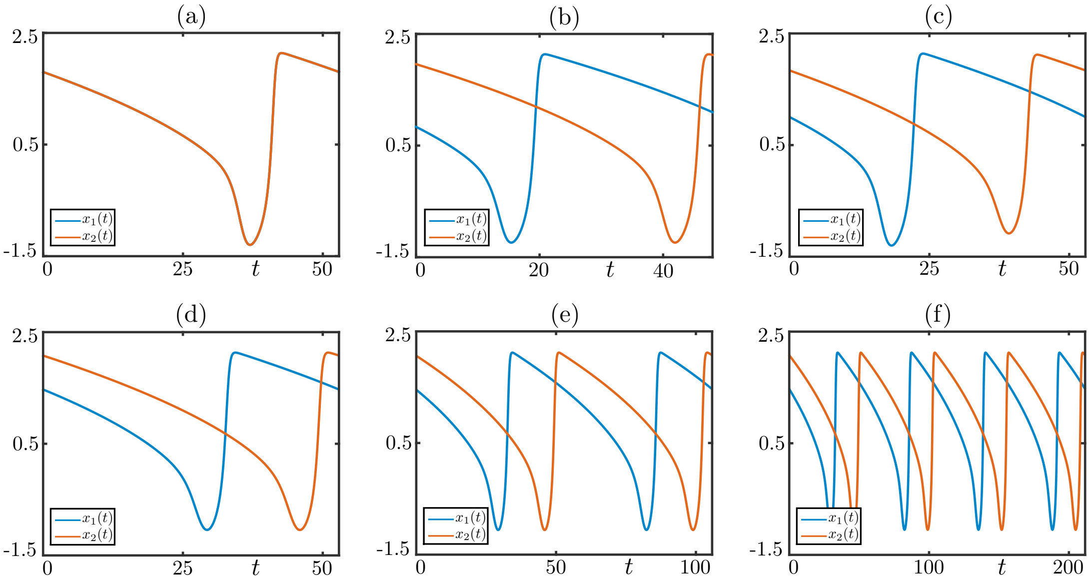

Figure 4.8: Coexisting stable IP (a), AP (b) OP (c) solutions for $c = 0.986267$ from Figure 4.7 (c). Stable T-periodic solution for $c = 0.98631587277$ (d), $2T$-periodic solution for $c = 0.9863137635$ (e), and $4T$-periodic solution for $c = 0.98631334783$ (f), from Figure 4.7 (d).

vestigation of the function G, are well identified through the continuation analysis, in particular the coexisting stable IP and stable AP states (canards with head and relaxation cycles) born near the maximal canard solutions. This intricate bifurcation structure unveils a main connection between the stable IP and the AP states through the double Hopf point at $c = c_{Hopf}$, which gives rise to both the IP stable state and a branch of unstable AP states. Decreasing c further, additional bifurcations occur, in particular pitchfork bifurcation points (black dots in Figure 4.7 (a) to (c)) which correspond to events where the synchronous state loses some symmetry. Indeed, on both the IP and the AP branches these bifurcations lead to additional solution branches along which the two canard oscillators do not follow identical cycles; in each case, the synchronous state becomes identical again through fold bifurcations. Note that these non-identical branches emanating from both the IP and the AP states come close to each other (near a second pair of fold bifurcations) forming a structure that seem to be a broken transcritical bifurcation. This perturbed bifurcation is only conjectured here; a more detailed analysis of the ε-dependence of the synchronous states goes beyond the scope of this chapter and will be a question for future work. We simply remark that this structure seems to perturb from an additional connection between the stable IP and stable AP coupled canard states. Finally we note the presence of several sequences of PD bifurcations (colored dots in Figure 4.7 (d)) which are likely to indicated small zones of chaotic dynamics in this region of parameter space.

One striking element about the bifurcation diagram described above is the fact that most of the connecting branches between the IP and the AP synchronous states are organized near solutions that correspond to maximal canards. It is therefore natural to ask about the effect of the coupling strength α on such synchronous states containing maximal canard segments; we focus on this aspect in the next section.

4.4 Effect of the coupling strength α

The interaction function analysis reveals the existence and stability of synchronous states for weakly coupled oscillators, although how “weak” the coupling should be in order that the theory applies is questionable. For instance, it was shown in [52] that for leakly integrate-and-fire type of oscillators the H function analysis is valid for moderate coupling strengths, whereas other papers (see e.g. [61, 57]) have mentioned a loss of 1:1 phase locking estimated by the interaction function analysis. In the case of coupled canard-explosive systems where the properties of the underlying oscillators vary brutally in parameter ranges that are exponentially small in time-scale parameter ε, the notion of weak coupling can be even more vague. For instance the region with cascades of PD bifurcations, highlighted in Figure 4.7 (d) and corresponding to cycles that are close to the maximal canard regime (under weak coupling of strength $\alpha = 10^{-5}$), gives a good numerical evidence that canard orbits are very sensitive to perturbations and that the validity of the interaction function analysis is limited in such cases.
In order to investigate this aspect further, we next consider the phase difference dynamics of two coupled identical headless canard cycles for a c-value in the neighborhood of the maximal canard, as a function of the coupling strength $\alpha > 0$. This numerical continuation study will focus both FF and FS interactions. The aim is to identify what range of the perturbation strength can give rise to interesting canard-mediated dynamics that are not predicted by the interaction function analysis but can still be analyzed using slow-fast arguments.

4.4.1 Fast-to-Fast (FF) coupling

The bifurcation structure in α for this case in presented in Figures 4.9 and 4.10 (zoomed views); associated solution profiles are shown in Figures 4.11 and 4.12. A stable OP synchronous state with a phase difference $\phi^* = 0.34$ is predicted by the interaction function analysis for the case of two headless canard cycles with FF-coupling, that is, for system (4.3.1); see Figure 4.5 (a) and Figure 4.6 panel 4. Using the bifurcation diagram presented in Figure 4.9, we can conclude that this OP regime persists for $\alpha \in (0, 6.63371 \times 10^{-5}]$. It loses its stability at $\alpha \approx 6.63371 \times 10^{-5}$ via a PD bifurcation where the interaction function result is violated, and consequently, not valid for greater coupling strengths. Switching branch at this PD point reveals the presence of a PD cascade, for which we compute only a few subsequent branches. Among the stable part of these branches of period-$2nT$ synchronous solutions (near which chaotic orbits surely exist too), that is, for a coupling strength $\alpha \in (6.63371 \times 10^{-5}, 0.0083195]$, there exists a family of solutions displaying what we call “spike suppression”. This scenario corresponds to when one of the oscillators spikes by following a canard with head while the other always remain in the headless canard regime. Regarding the IP solution branch, it becomes stable at $\alpha \approx 0.0085633416545$ and coexists, for $\alpha \in [0.0085633416545, 0.289498]$, with the $2nT$-periodic headless canard solution branch.

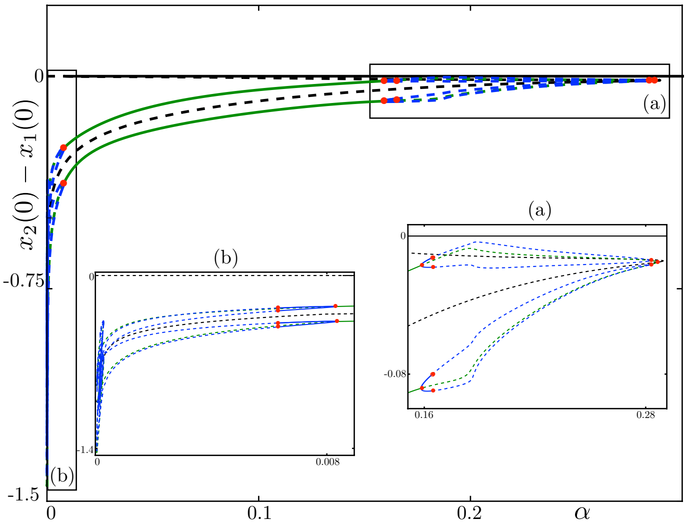

Figure 4.9: Continuation in α for the FF-coupled VDP system for a c value in the vicinity of the maximal canard (red cycle in Figure 4.3-(c)). Inset panels (a) and (b) are zoomed viewed of different parts of the main panel. Bifurcation points (mainly PD bifurcations) are indicated by red dots. T-periodic (black), $2T$-periodic (green) and $4T$-periodic (blue) branches coexist with stable (solid) and unstable (dashed) solutions.

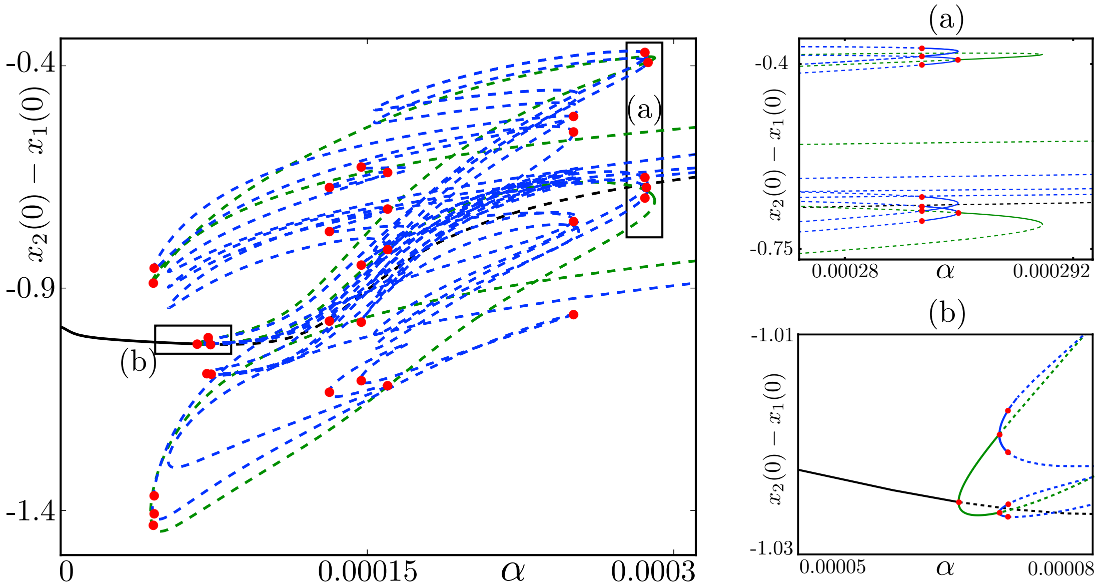

Figure 4.10: Continuation in α for the FF-coupled VDP system in the maximal canard regime (red cycle in Figure 4.3-(c)): zoomed view from Figure 4.9 in the region of PD cascades (most of the computed PD bifurcation points being highlighted by colored dots).

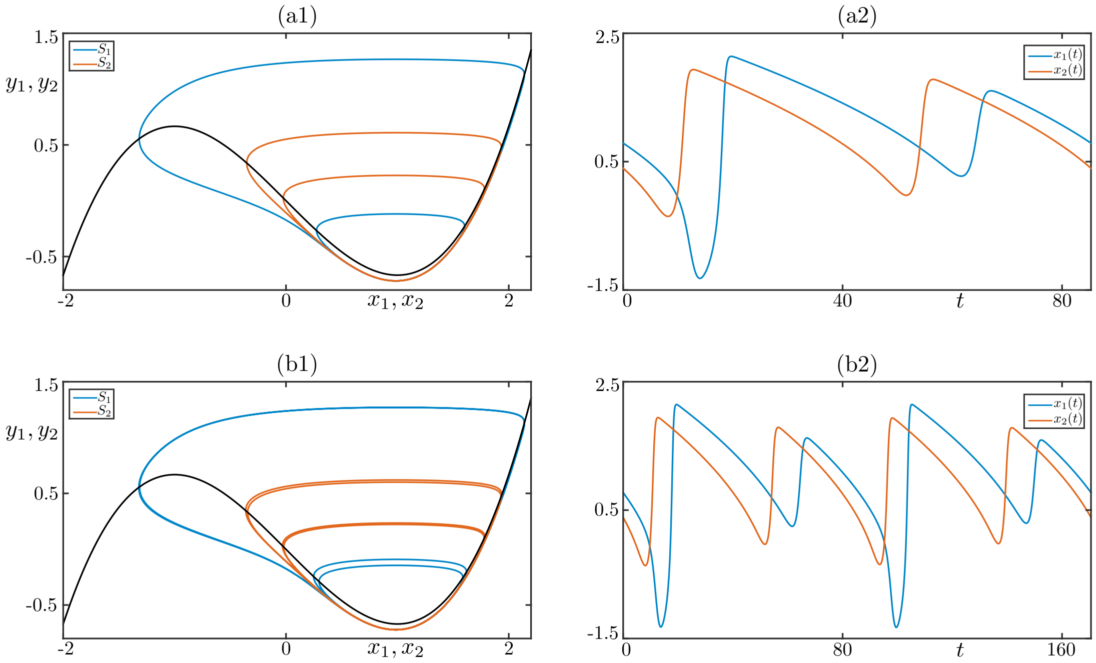

Figure 4.11: Period $2T$ (top panels) and period $4T$ (bottom panels) non-identical OP synchronous states for the FF-coupled system in the maximal canard regime, illustrating the spike suppression scenario. Values of the coupling strength α are 2.86959×10^{-4} in panels (a1)-(a2) and 2.85359×10^{-4} in panels (b1)-(b2).

4.4.2 Fast-to-Slow (FS) coupling

The bifurcation structure in α for system (4.3.2); in presented in Figure 4.13; associated solution profiles are shown in Figure 4.14. The stable IP synchronization state predicted by the interaction function analysis for the FS-coupling (Figure 4.5 (b)) becomes unstable at $\alpha \approx 0.007498445$ (Figure 4.13 (a)) via a subcritical PD bifurcation that introduces an unstable $2T$-periodic branch which becomes stable at $\alpha \approx 8.74785268 \times 10^{-5}$, where the interaction function analysis loses its validity. Continuing that branch leads to the detection of further PD bifurcations organized in a cascade, which we compute only the beginning of; see Figure 4.13 (b). These $2nT$-periodic branches correspond to families of solutions displaying what we call "spike alternation", that is, a scenario for which both oscillators of the FS-coupled system follow subsequently a headless canard segment and then a canard-with-head segment, hence performing an MMO [15]; see Figure 4.14 for an illustration on such MMO cycles with period T, $2T$ and $4T$ on (a), (b) and (c) panels, respectively. Depending on the value of the coupling strength α, the oscillators may follow the same or different canard trajectories.

The difference between the synchronization properties of headless canards and canards with head is also visible in the α continuation: bifurcation diagrams of canard with head cycles are qualitatively different than the ones of maximal canards and headless canards (close to the maximal canard). For instance, FF-coupled identical canard with head cycles (yellow cycle in Figure 4.3-(c)) do not yield any interesting bifurcation

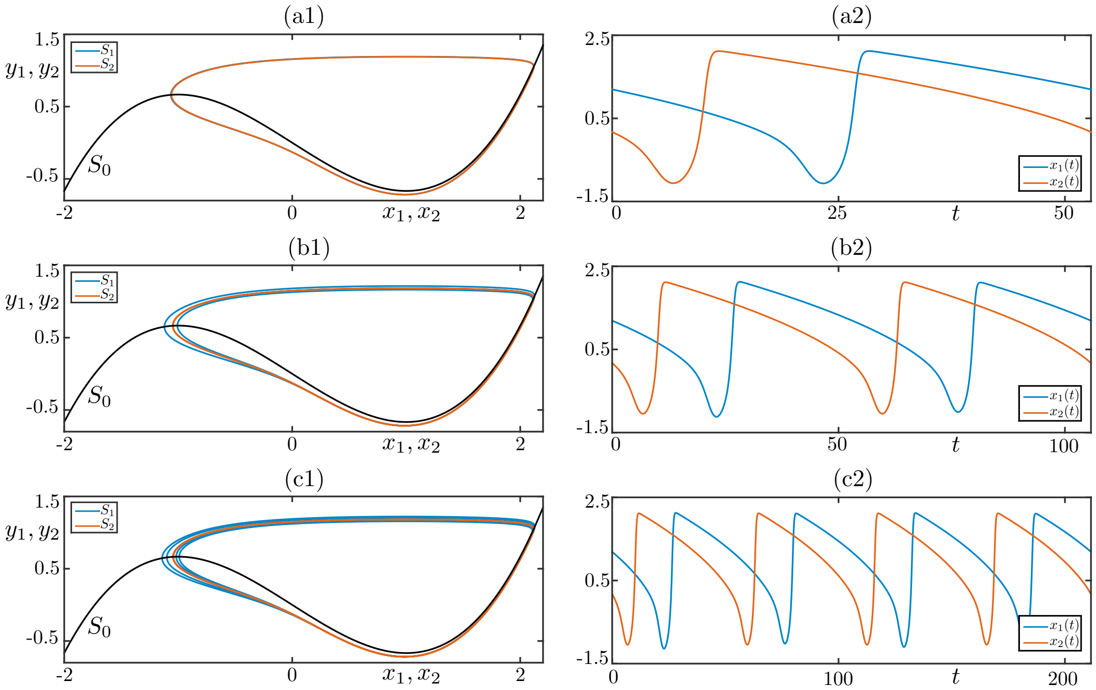

Figure 4.12: Period T (top panels, identical), period $2T$ (middle panels, non-identical) and period $4T$ (bottom panels, non-identical) stable OP synchronous states of the FF-coupled VDP system in the maximal canard regime. The phase differences for these states are coherent with the interaction function analysis. Values of the coupling strength α are 6.63371×10^{-5} in panels (a1)-(a2), 7.04717×10^{-5} in panels (b1)-(b2) and 7.13322×10^{-5} in panels (c1)-(c2). Left panels: Trajectories projected onto the (x_i, y_i) planes. Right panels: Time series of the x_i coordinates.

structure like the one in Figure 4.9 and the shape of the bifurcation diagram of FS coupled cycles in Figure 4.15 is quite different than Figure 4.13. Yet, we again obtain $2nT$-periodic branches: the (almost) IP synchronous solution predicted by the interaction function analysis becomes unstable via a PD bifurcation at $\alpha = 2.0664925081 \times 10^{-3}$. Further PD bifurcations are visible for $\alpha \in [2.0664925081 \times 10^{-3}, 2.2182827269 \times 10^{-2}]$. Figure 4.16 shows the example period T, $2T$ and $4T$ solutions.

On both FF- and FS-coupled canard systems, we have observed using a numerical bifurcation analysis the proximity of several stable solution branches with complicated oscillatory patterns mixing passages along headless canards and along canards with head. Among these complex patterns, the regions where spike-suppression and spike-alternation states exist should be underlined. In FF-coupled systems, the spike-suppression solutions are the only stable synchronous states of the system and they appear under very weak interaction, which indicates that weak interaction between non-spiking oscillators can change the spiking pattern by forcing only one oscillator to spike. Whereas in FS-coupling, the spike-alternation solutions lie in a bi-stable region with IP states. Depending on the initial conditions or presence of a noise, these MMO-type synchronous states can appear. In the context of neuronal systems, these complicated oscillatory solutions alternate subthreshold oscillations and spikes. These

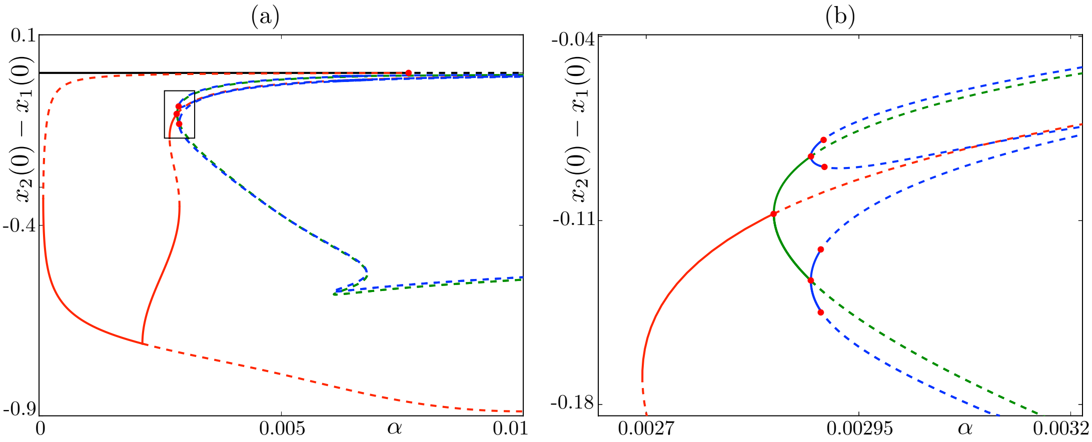

Figure 4.13: Continuation in α for the FS-coupled VDP systems near the maximal canard regime (red cycle in Figure 4.3-(c)). Bifurcation points (PD bifurcations) are indicated by red dots. Both stable (solid) and unstable (dashed) parts of T-periodic (black), $2T$-periodic (red), $4T$-periodic (green) and $8T$-periodic (blue) branches are shown.

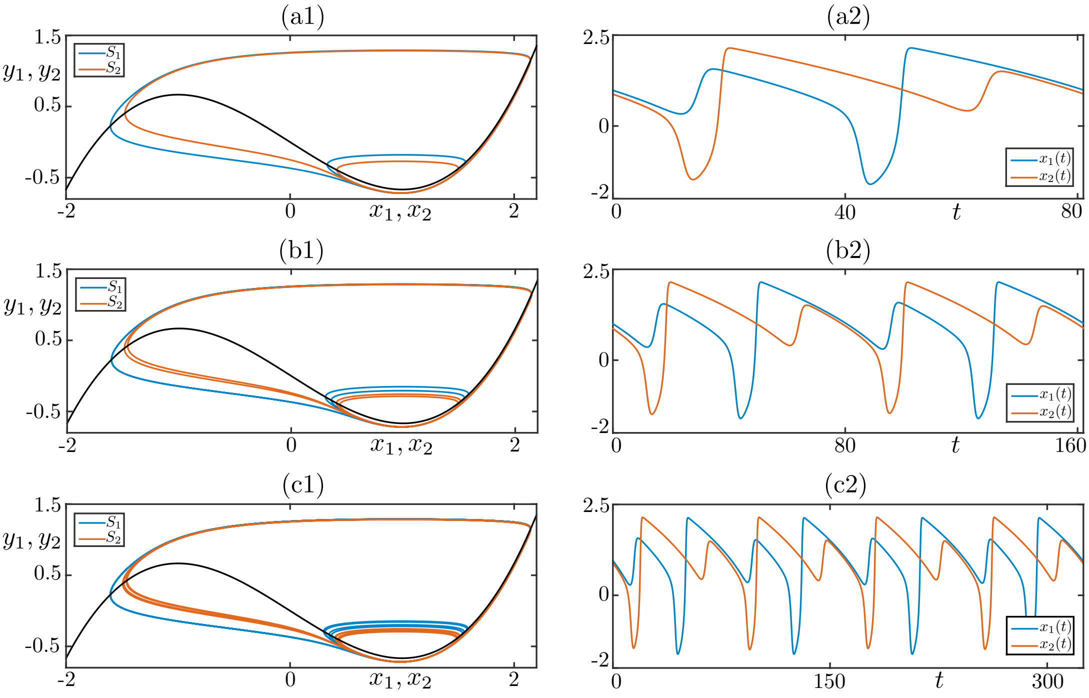

Figure 4.14: Period T (top panels), $2T$ (middle panels) and $4T$ (bottom panels) stable non-identical OP synchronous states displaying spike alternation for the FS-coupled system near the maximal canard regime. Values of the coupling strength α are $2.8502655978 \times 10^{-3}$ in panels (a1)-(a2), $2.8939484985 \times 10^{-3}$ in panels (b1)-(b2) and $2.9039987077 \times 10^{-3}$ in panels (c1)-(c2). Left panels: Trajectories projected onto the (x_i, y_i) planes. Right panels: Time series of the x_i coordinates.

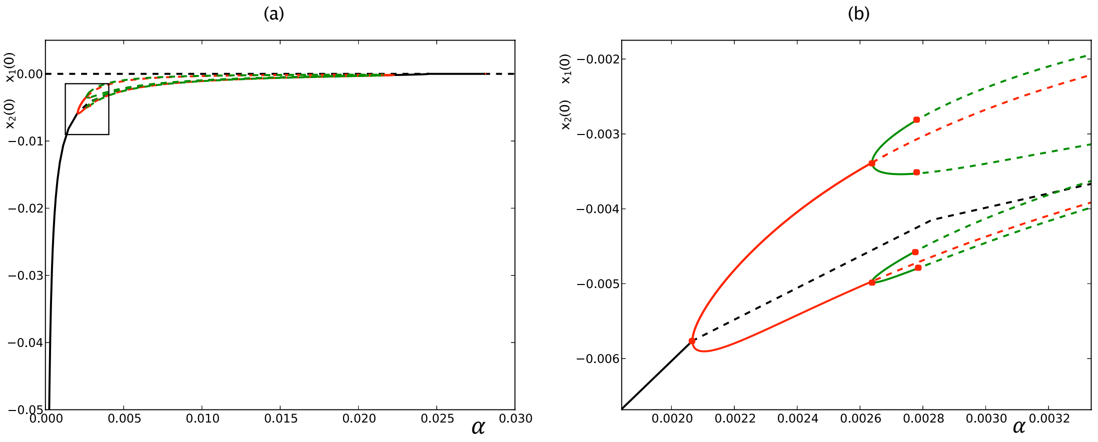

Figure 4.15: Continuation in α for the FS-coupled VDP systems in canard with head regime (yellow cycle in Figure 4.3-(c)). Bifurcation points (PD bifurcations) are indicated by red dots. Both stable (solid) and unstable (dashed) parts of T-periodic (black), $2T$-periodic (red) and $4T$-periodic (green) branches are shown. Bifurcation structure is different than the one in Figure 4.13

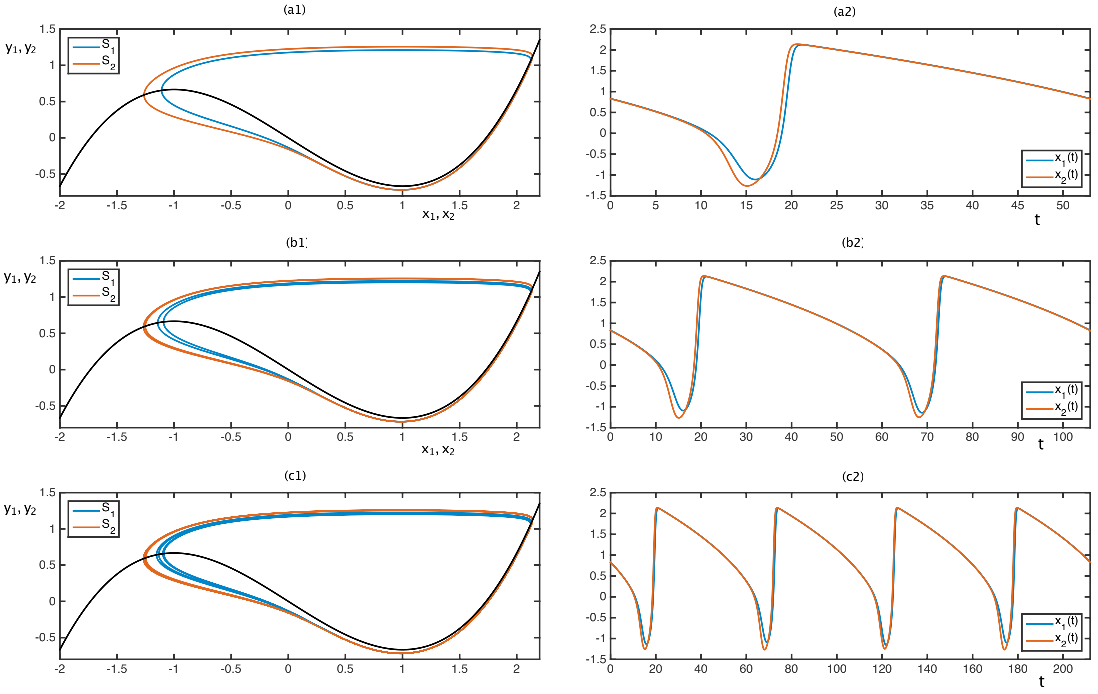

Figure 4.16: Period T (top panels), $2T$ (middle panels) and $4T$ (bottom panels) stable (almost) IP synchronous states displaying spike alternation for the FS-coupled canard with head cycles the maximal canard regime. Values of the coupling strength α are $2.0664925081 \times 10^{-3}$ in panels (a1)-(a2), $2.6385701837 \times 10^{-3}$ in panels (b1)-(b2) and $2.6388141075 \times 10^{-3}$ in panels (c1)-(c2). Left panels: Trajectories projected onto the (x_i, y_i) planes. Right panels: Time series of the x_i coordinates.

solutions are not predicted by the interaction function analysis typically employed in weakly coupled oscillator studies. However, one can justify there existence by invoking the presence in such systems of repelling (Fenichel) slow manifolds, which are known to be exponentially close to each other (in the timescale separation parameter ε). Therefore, the presence of these manifolds near the middle branch of the critical manifold S_0 of each individual slow-fast oscillator can allow to justify that, for values of the coupling strength α that are larger that such exponentially small quantities, synchronized states of the coupled system may follow these manifolds on one side (subthreshold regime) or the other (spiking regime) while staying very close to the boundary (well approximated by maximal canards).

4.5 Discussion

In this chapter, we have extended previous results on weakly coupled slow-fast oscillators to the canard regime, both from a theoretical and numerical perspective. Our main finding is that the behavior of adjoint solutions (or equivalently, of iPRCs) changes qualitatively when the canard cycle under consideration is moving (as the canard parameter is varied) along the associated explosive branch. Indeed, the sign and shape of the adjoint solutions flip as the underlying canard cycle goes from the headless canard regime to the canard-with-head regime, the transition taking place at the maximal canard cycle. This change of behavior of adjoints of canard cycles upon infinitesimal perturbations can be explained by the peculiar known property of the period function of a canard-explosive branch, which can be summarized as follows: larger headless canards are greater periods, whereas larger canards-with-head have smaller periods. As explained in Section 4.3, this argument is fully applicable when the perturbation is applied near the fold point of the critical manifold corresponding to the canard point, and its validity is weakened as the perturbation is applied further away from this fold point, where the contraction towards the unperturbed cycle rapidly annihilates the effect of the perturbation. This justifies that adjoints computed along canard cycles are very close to zero during most of the cycle except along a time interval corresponding to when the canard cycle passes near the fold (canard) point of the critical manifold S_0. Nevertheless, the explanation that we provide is valid for the most informative part of the adjoint solutions and bears consequences on the synchronized solutions of coupled canard systems.

We have shown this mechanism for a prototypical canard oscillator, namely the VDP system, but it is clearly applicable to all excitable systems of this form, in particular, to slow-fast type-II neuron models such as the reduced HH studied in [23] model. This opens the way to a renewed understanding of iPRCs in such neuron models, from the Hopf cycles (whose adjoint solutions will qualitatively look like those associated with small headless canard cycles) to the spiking cycles (whose adjoint solutions will qualitatively look like those associated with canards with head). In particular, our findings can be related to recent work on isochrones since PRC analysis originates in the study of phase models and isochrones [120]. Recently the isochrones of canard cycles were investigated numerically in [121] where evidence was given that their properties change in the vicinity of the maximal canard neighborhood; this is likely to be closely linked with the results presented here. While a full comparison of these two aspects of canard cycles' phase properties goes beyond the scope of the present work, it is certainly an interesting topic for future work.

While studying adjoint solutions along canard cycles, we have also proposed a numerical strategy based on numerical continuation to compute these objects as a system parameter is varied, that is, to reliably compute a family of limit cycles and at the same time a family periodic solutions to the associated adjoint problem. Making profit of the boundary-value solver of AUTO, we could easily identify the flip in the solution to the adjoint problem as the cycle goes through the maximal canard.

In Section 4.3, we looked at the bifurcation structure of the synchronous states of the weakly coupled identical VDP systems when varying the main system parameter, which in this case controls the position of the slow nullcline but would likely be an applied current in the neuronal context. We found an intricate structure of solution branches of IP, AP and OP states, connected through both PD and pitchfork bifurcations, which are organized around the maximal canard solution. While the synchronization properties of relaxation cycles were already known, we believe that the bifurcation structure of the weakly coupled canard regime is by-and-large novel, in particular the role of the maximal canard as an organizing center for the IP, AP and OP families.

In Section 4.4, we focused on the bifurcation structure of synchronous states of coupled identical VDP systems in the maximal canard regime, depending on α. PD bifurcations and chaotic trajectories in VDP-like systems under periodic perturbation have been studied in e.g. [122, 96, 97]. In the present study, we unveiled a complex web of period-$2nT$ branches suggestive of the presence of nearby chaotic attractors, which we chose not to investigate. Instead, we highlighted these further synchronous states, all existing close to maximal canard solutions but not all predicted by standard interaction function analysis. Being close to a maximal canard, hence to threshold, these solutions may contain both passages near headless canards and near canards-with-head, therefore an alternation between subthreshold oscillations and spikes. Even when the classical weakly coupled theory may not apply, the slow-fast phase plane structure of the underlying single canard oscillator enables to understand why such mixed-mode oscillatory synchronous states can arise for small to moderate coupling strength, owing to the geometry and proximity between families of repelling slow manifolds. As a question for future work, we plan to investigate the relevance of these complicated synchronous states in the context of neuron models, where canards-with-head may be considered as not so rare events but rather as spikes with a slow activation or in the context of *after-hyperpolarization-potential* phenomenon where neurons do not necessarily spike while overcoming the spiking threshold after hyperpolarisation.

Control of canard cycles has been studied in [123] where the authors have obtained MMOs, cascades of PD bifurcations and chaotic behavior in a FHN-type relaxation oscillator depending on the control setup. Developing control strategies for reaching desired spiking behavior in coupled canard systems can be an interesting future direction of study.

Finally, as an appendix, we also provided an analytical formula for the adjoint solutions associated with limit cycles of Liénard systems, which gives reasonable yet perfectible numerical results for canard cycles.

This work is only a first step towards extending canard studies to the realm of weakly coupled oscillators and, more generally, to weakly connected networks. It is not rigorous yet but we have identified the main geometrical structures that play a pivotal role in shaping the main family of synchronous solutions to coupled planar slow-fast systems in the canard regime. Moreover, we have highlighted the central role of the maximal canard in organizing the synchronization properties of such systems. Beyond the effect of canard-explosive dynamics on synchronization, we plan in the near future to investigate similar effects in (at least three-dimensional) systems with canards organized by folded singularities [124] as well as in systems with slowly varying quantities, such as bursting systems where spike-adding canard explosions will be likely to have a dramatic effect on the synchronization properties of coupled bursters [125, 16].

4.6 Appendix: Analytical expression for adjoints of canard cycles

Here we use classical results from the theory of linear differential equations [126] as well as unpublished results by Schecter [127] in order to derive an expression for the periodic solution of the adjoint problem associated with a limit cycle of a Liénard system. This extends the approach taken by Izhikevich in [60], who considered the case of relaxation cycles by taking the limit $\varepsilon = 0$. Izhikevich's formulation is not applicable to canard cycles due to the presence of the folds of the critical manifold S_0 which gives rise to canard dynamics and requires to have $\varepsilon \neq 0$ in the computation of the adjoints.

We consider the following VDP type slow-fast system written in Liénard form

$$\begin{aligned} x' &= y - f(x) := F(x,y) \\ y' &= \varepsilon(c - x) := \varepsilon G(x,y), \end{aligned} \tag{4.6.1}$$

where $f(x) = x^3/3 - x$ is a cubic function and the prime denotes differentiation with respect to the fast time t. We consider a canard cycle solution of system (4.6.1), that is, a periodic solution $\gamma(t) = (x(\varepsilon t), y(\varepsilon t))$.
The linearized system associated with (4.6.1) along γ is given by

$$\begin{aligned} v' &= -f'(\gamma_1(t))v + w \\ w' &= -\varepsilon v, \end{aligned} \tag{4.6.2}$$

which we can recast as a second-order linear differential equation

$$v''(t) + f'(\gamma_1(t))v'(t) + (f''(\gamma_1(t)) + \varepsilon)v(t) = 0. \tag{4.6.3}$$

An obvious solution of (4.6.3) is $(\gamma_1'(t), \gamma_2'(t))$. Recall that if one knows a particular solution y_* of the second-order linear differential

$$y''(t) + p(t)y'(t) + q(t)y(t) = 0,$$

then one can obtain another solution $y_\#$, non-proportional to the first one — hence forming a basis of the space of solutions together with the first one — using a variation of constant type formula, that is,

$$y_\#(t) = u(t)y_*(t),$$

with u given in general integral form by

$$u(t) = \int_0^t \frac{\exp\left(-\int_0^s p(\sigma)d\sigma\right)}{y^2(s)} ds. \tag{4.6.4}$$

Therefore, knowing the solution $(\gamma_1'(t), \gamma_2'(t))$ of the linearized system written as a second-order equation (4.6.3), a non-proportional solution is given by $(v(t), w(t))$ with

$$\begin{aligned} v(t) &= u(t)\gamma_1'(t) = \gamma_1'(t) \int_0^t \frac{\exp\left(-\int_0^s f'(\gamma_1(\sigma))d\sigma\right)}{{\gamma_1'}^2(s)} ds \\ w(t) &= v'(t) + f'(\gamma_1(t))v(t) \end{aligned}$$

Hence we have

$$\begin{aligned} w(t) &= u'(t)\gamma_1'(t) + u(t)(\gamma_1''(t) + f'(\gamma_1(t))\gamma_1'(t)) \\ &= \frac{\exp\left(-\int_0^t f'(\gamma_1(s))ds\right)}{\gamma_1'(t)} + u(t)\gamma_2'(t). \end{aligned}$$

The adjoint equation associated with system (4.6.1) along the limit cycle γ is given by

$$\dot{\mathrm{Z}} = -\mathrm{J}(\gamma(t))^T \mathrm{Z}, \tag{4.6.5}$$

where Z is a two-dimensional real vector and $\mathrm{J}(\gamma(t))$ is the Jacobian matrix evaluated along the solution γ. Following [127], we write the solution to equation (4.6.5) under the form

$$\mathrm{Z}^T(t) = \exp\left(\int_0^t f'(\gamma_1(s))ds\right) \begin{bmatrix} -s_2 & s_1 \end{bmatrix}, \tag{4.6.6}$$

where $s = (s_1, s_2)$ is a solution to the linearized equation (4.6.3). We apply this formula to the two solutions $(\gamma_1'(t), \gamma_2'(t))$ and $(v(t), w(t))$ of the linearized equation, which gives us two solutions of the adjoint equation. What we wish to get is a periodic solution of the adjoint; to get it, we will find a suitable linear combination of the two solutions obtained using Schecter's strategy, imposing periodicity. Namely, we will find scalars α and β such that

$$\alpha \mathrm{Z}_{\gamma'}(T) + \beta \mathrm{Z}_s(T) = \alpha \mathrm{Z}_{\gamma'}(0) + \beta \mathrm{Z}_s(0), \tag{4.6.7}$$

where α and β are reals, $\mathrm{Z}_{\gamma'}$ and Z_s being obtained using formula (4.6.6) from the linearization of the limit cycle γ and the solution $(v(t), w(t))$ described above, respectively. Therefore, focusing on the second component only, the periodicity condition (4.6.7) becomes

$$\begin{gathered} \alpha \exp\left(\int_0^T f'(\gamma_1(s))ds\right) \gamma_1'(T) + \dots \\ \beta \exp\left(\int_0^T f'(\gamma_1(s))ds\right) \gamma_1'(T) \int_0^T \frac{\exp\left(-\int_0^s f'(\gamma_1(\sigma))d\sigma\right)}{{\gamma_1'}^2(s)} ds = \alpha\gamma_1'(0). \end{gathered}$$

Given that γ' is itself periodic, we can simplify the above equality and obtain α as a function of β:

$$\alpha = \frac{-\beta \exp\left(\int_0^T f'(\gamma_1(s))ds\right) \int_0^T \frac{\exp\left(-\int_0^s f'(\gamma_1(\sigma))d\sigma\right)}{{\gamma_1'}^2(s)} ds}{\exp\left(\int_0^T p(s)ds\right) - 1}. \tag{4.6.8}$$

Condition (4.6.8) gives a one-parameter family of suitable linear combinations, one can apply a normalization to obtain a uniquely defined periodic solution to the adjoint equation.

4.6.1 Simulations of the analytical results

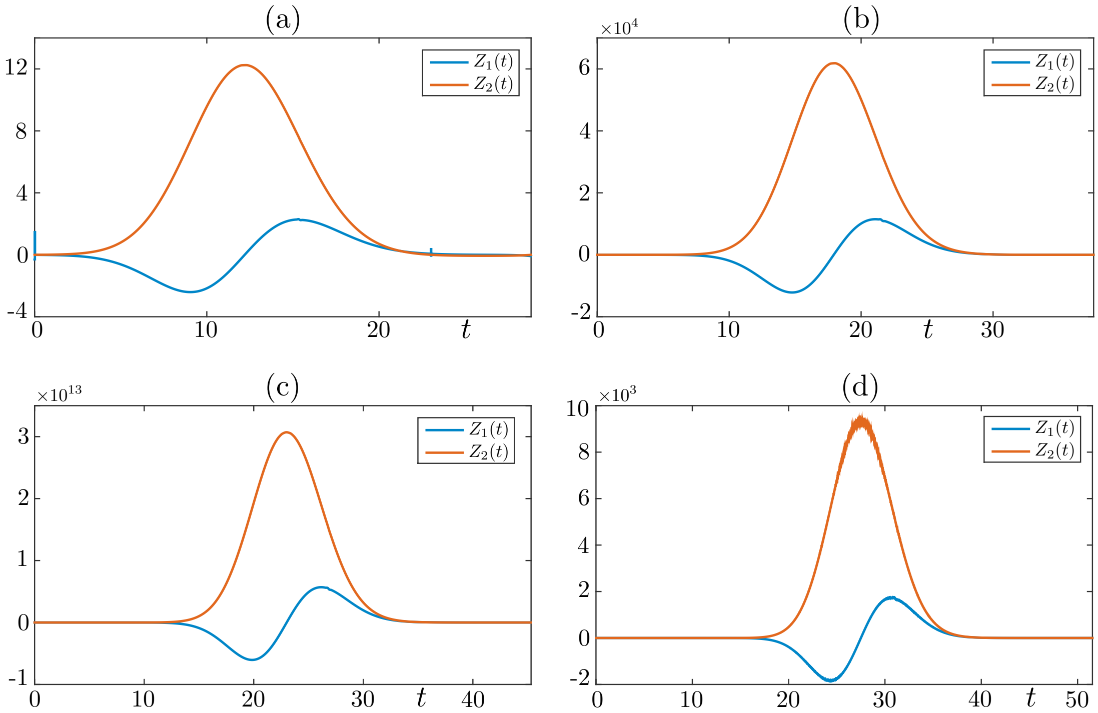

Figure 4.17: Adjoint solutions for the headless canard cycles shown in Figure 4.1 computed analytically using formula (4.6.6).

In order to compute the solutions of the adjoint equation given by (4.6.6) with the two different solutions to the linearized equation (4.6.2), namely γ' and (v, w), we need to evaluate numerically the function u given by the integral formula (4.6.4), and we also need to evaluate the prefactor

$$P_f(t) = \exp\left(\int_0^t f'(\gamma_1(s))ds\right).$$

To do so, a simple way is to write u as the solution of a second-order differential equation, and P_f as the solution of a first-order differential equation, and solve these equations numerically with, e.g., an Euler scheme. More precisely, we have

$$\begin{aligned} u'(t) &= \frac{\exp\left(-\int_0^t f'(\gamma_1(s))ds\right)}{\gamma_1'(t)^2} \;:=\; h(t) \\ h'(t) &= -\left(f'(\gamma_1(t)) + 2\frac{\gamma_1''(t)}{\gamma_1'(t)}\right) h(t). \end{aligned} \tag{4.6.9}$$

Similarly, we have

$$P_f'(t) = f'(\gamma_1(t))P_f(t).$$

Results computed for the headless canard cycles are given in Figure 4.17.

4.6.2 Limits of the formula

The strategy we proposed overcomes the singularities due to the presence of folds on the critical manifold, however it has limitations. First, the approximation of adjoint solutions of canard cycles with this formula can be considered as successful for headless canards (see Figure 4.17), yet a lot of care in the numerical simulations used is required. However, even with such care we have been unable to compute adjoints associated with large canards using this formula. The reason for this can be understood by looking the expression in (4.6.9) which is singular when $\gamma_1'(t) = 0$, that is, at extrema of γ_1. We can try to integrate these equations by splitting the solution into two branches excluding the extrema. With this strategy, our formula can be used to compute adjoints for all canard cycles and, hence, extend Izhikevich's approach. The second drawback of formula (4.6.6) is that it assumes a Liénard form for the system under consideration. Hence, it is not directly applicable to more general planar slow-fast systems, in particular, to biophysical neuron models such as the two-dimensional reduction of the Hodgkin-Huxley system that we considered in Section b.

Chapter 5

Conclusion and perspectives

In this dissertation, we have studied canard solutions and dynamic bifurcations in coupled multiple timescale systems inspired from neuronal dynamics.

We have started from a 4D system with 2 coupled FHN oscillators evolving on different timescales. This model was originally introduced to account for the dynamics of GnRH secretion and each subsystem represents the mean-field activity of different populations of neurons, which are the populations of secreting and regulating neurons. We have taken a direction from a macroscopic scale to a mesocopic scale motivated by additional features in the secretion patten of GnRH: a surge with 2 bumps (camel surge) and a partial desynchronization before the surge (pulse degradation). In Chapters 2 and 3, we have worked on the 6D extension of the model which consists of 2 mutually interacting secretors (fast FHN oscillators) receiving the same signal from the regulator (a slow FHN oscillator). In Chapter 2, we have identified (de)synchronization mechanisms arising from the relation between the canard transitions and a linear mutual coupling. In Chapter 3, we have attempted to model a camel surge and pulse degradation embedded the whole secretion pattern by considering regulatory-dependent asymmetric coupling functions. In Chapter 4, we have studied synchronization of coupled identical VDP systems in the canard regime and we have generalized previous studies on weakly coupled slow-fast systems to canard regime. We have mainly used numerical continuation to compute slow manifolds, bifurcation diagrams and solutions to adjoint equations.

In this thesis, we have shown the existence of canard transitions in slow-fast coupled systems. The element of proof that we are giving is based on the transversality argument of the classical canard theory. The 5D minimal model introduced in Chapter 2 to compute slow manifolds of coupled systems with folded-saddle singularities is quite general and can also be used to investigate the dynamics of coupled slow-fast oscillators near folded-node singularities. Using the 5D minimal model, we have showed that trajectories of identical systems with folded-saddle singularities can be driven to different sides of the maximal canards under weak coupling. This separation near a folded saddle determines the surge timing and can cause desynchronization before the surge in identical secretors of the 6D extension of the GnRH model. The separation of trajectories near a folded node of nonidentical systems impacts the number of SAOs, number of pulses and phase dynamics. In larger networks, the canard transition near a folded node can be responsible for the formation of clusters in which oscillators with similar canard trajectories are grouped; locally, exponentially small differences in trajectories can induce $O(1)$ differences in the output.

The effects of maximal canards on the separation of trajectories in coupled oscillators are studied in more detail in Chapter 4. We have shown that under (weak to moderate) coupling MMO type solutions can arise in mutually interacting identical VDP oscillators in canard regime. They are formed by the alternation between subthreshold oscillations and spikes, and they correspond to $2nT$-periodic synchronous solutions of the coupled system. In other neuronal models with a slow activation generating spikes (e.g. late spiking neocortical neurons), maximal canards can have more significant effects on synchronization dynamics by separating resting and spiking states of individual cells.

One of the open questions of Chapter 2 was generalization of the phase models and weakly coupled oscillators to coupled canard cycles. In Chapter 4 we have provided an extension of weakly coupled theory on relaxation oscillators to canard cycles. Benefiting from the BVP solvers and numerical continuation methods embedded in AUTO, we have computed limit cycle families of singularly perturbed planar systems and associated adjoint solutions, which encode the synchronization properties of weakly coupled oscillators. We have unveiled a qualitative change in the behavior of the adjoint solutions across the maximal canard. This change has been interpreted as a property of the period function of the canard explosion: the period function increases from the Hopf bifurcation to the maximal canard, then it decreases from the maximal canard to the relaxation regime. When we focus on the adjoint solutions of the canard cycles lying the neighborhood maximal canard, we observe that the adjoint solutions decreases as the canard cycle approaches to the maximal canard. In the $\varepsilon \to 0$ limit, we can expect to obtain a flat adjoint on the maximal canard. Hence, we conjecture that weakly coupled maximal canard cycles in the singular limit can synchronize at any phase-locking state.

In singularly perturbed planar systems, canard cycles are very sensitive to parameter variations and, therefore, difficult to compute by means of numerical integration. As the timescale separation parameter ε decreases, it becomes increasingly difficult (if possible at all) to use classical integration methods in the context of initial value problem, whereas the numerical continuation methods and BVP solvers give much better results regardless of stability of the cycles. The methods we have used to compute the adjoint solutions of the canard cycles can be improved in two ways. The first one can be embedding normalization condition of the adjoint equations by redefining the computation setting as a 2 point BVP problem. The second improvement can be in the way to find a starting non-trivial solution to the adjoint equation. For the methodology we have introduced, any non-trivial solution is sufficient. However, computing the Floquet bundle to find the non-trivial solution of the adjoint equation is another option. This requires more delicate techniques but can improve the performance in the singular limit.

In Chapter 4, we have developed an analytic expression for the adjoint solutions to systems with canard points. The method we have used relies on the linearization of the flow. This expression has limits on extreme points of the fast component of the flow which introduce discontinuity that can be eliminated by using delicate integration methods. The second drawback is the assumption of having a Liénard form for the system under consideration. Hence, it cannot be directly applied to more general planar slow-fast systems. As a future aspect, the asymptotic theory of the relaxation cycles displaying canard solutions can be studied for finding solutions to adjoint equations.

What “weak” means practically for coupled oscillators is particularly striking when considering the canard regime. Along the canard explosion of coupled VDP oscillators, there are period-$2nT$ branches not estimated by the standard interaction function analysis. The bifurcation structure of the phase difference depending on the coupling strengths indicates the narrowness of the range of the coupling strength available for standard analysis based on averaging. This range depends on the canard cycle under consideration and on the timescale parameter ε. The relation between the timescale parameter and the coupling strength suitable for using averaging methods is an interesting topic for future work. PD-cascades and MMOs are considered as beginning of chaotic dynamics, thus beyond the weak limit, the coupling can lead to “canard chaos”, which is worth to investigate.

Another open question emanating from Chapter 2, aside the phase dynamics of canard solutions, was to consider a biologically oriented parameter set for the 6D model, which meets quantitative features of the GnRH secretion pattern. In Chapter 3, we have focused on additional features of the GnRH secretion pattern not captured by the 4D “1 secretor/1 regulator” configuration, such as a camel surge and pulse degradation. We have interpreted the occurrence of a camel surge as a possible loss of mutual interaction between the secretors for some episodes of the surge. We have modeled this possibility by considering regulatory-dependent coupling functions. The switch mechanism in the coupling depending on the regulatory signal can produce a camel surge in asymmetrically coupled nonidentical secretors.

Defining the global output of the 6D system as the sum of the thresholded outputs of the individual secretors transformed the concept of synchronization to pulse overlapping. The pulse overlapping disappears due to two natural properties of the 6D model: slowly varying regulator signal which increases the pulse frequency, and nonidentical secretors which have different pulse frequencies. The continuous slow motion of the regulatory signal during the pulsatile regime prevents the oscillators from settling at a stable synchronous state even if such these synchronous states do not necessarily allow the pulses to overlap. The regulatory signal also changes the stability of synchronous solutions via PD bifurcations in the phase dynamics of heterogenous ensembles. This type of dynamic bifurcations was also observed in relaxation cycles in lasers under periodic perturbation. We have shown numerically that the pulse degradation can be related to the PD bifurcations in nonidentical secretors under asymmetric and constant coupling.

The problem we have faced was to obtain a camel surge and a pulse degradation with the same coupling function reasonable for both biological viewpoints and numerical studies. Hence, we needed to introduce a coupling function which remains dynamic during the pulsatile regime. With this dynamic coupling function, we were able to reproduce both a camel surge and degraded pulses in the same setting. On the other hand, the dynamic coupling function brought constraints to this study in quantifying the global output of the 6D system during the pulsatile regime. Thus, we needed to develop asymptotic tools. Even though many theoretical tools have been developed in the field of synchronization of oscillating systems, biologically realistic setups which include heterogeneity in both interacting systems and interaction modes may oblige us to rely on numerical studies.

The dynamic coupling function introduced in Chapter 3 couples the secretors in a thresholded rather than smooth manner; the secretors interact only when they are active (when they produce individual pulses). Therefore, the dynamically coupled secretors can be compared to pulse-coupled oscillators. One of the methods to analyze synchronization of pulse-coupled oscillators is constructing phase return maps describing the phase dynamics. We did not have time to go into that domain but analyzing the dynamically coupled secretors map models can be a future direction.

Following the GnRH framework in Chapter 2, we mainly considered diffusive coupling functions where the difference between the fast variables perturbs the system dynamics. In Chapter 3, which focuses on the interacting populations of endocrine neurons, the dynamic coupling function is already an application oriented extension of the diffusive formulation. In the context of coupled neurons, synaptically coupled systems have been studied where the oscillator frequencies and time constants of synaptic decay have critical roles in synchronization dynamics. The effect of oscillator frequencies we have identified for the diffusively coupled canard cycles can hold under synaptic coupling. Besides, a slow time scale introduced by the synaptic signal can impact the collective activity of the coupled canard oscillators, for instance, by causing slow-fast transitions near the fold regions like the pause mechanism examined in Chapter 2 or similar dynamic bifurcations in synchronous states identified in Chapter 3.

In this dissertation, variations in collective dynamics, such as spiking regimes, number of pulses, (de)synchronization or phase differences, essentially arose from dynamic bifurcations caused by slowly varying parameters or system variables. In another context, variations can be caused by a dynamic medium which hosts neurons. The transitions we observed give birth to different modes in a 2-oscillator network of multiple timescale systems but there can be more complex outputs in larger networks of planar systems or bursters. Another aspect can be developing control strategies over transitions between different modes of collective dynamics arising in these networks.

There is a recent effort on generalizing the theory of weakly coupled oscillators to the systems with slowly varying variables, inputs or parameters and finding explicit expressions. Slow-fast systems with folded singularities require a special focus in that direction. For instance, the formula we have introduced which overcomes the problem of folds on the critical manifolds can be taken into account.

In this study, we have kept the compact modeling approach of the 4D system designed on the macroscopic level. This compact modeling approach is not intended to have a direct biophysical meaning, yet, the combination of biological and long-term modeling motivations have encouraged us to go further in reproducing the complex patterns of the GnRH secretion. The mechanisms underlying the complex behaviors of this neuroendocrine system have raised challenging questions on the mathematical ground. Our choices of rather simple coupling functions have not only the advantage of revealing possible structures especially in the multiscale modeling framework and extending the capacity of the system to generate complex patterns, but also they bring interesting insight on mathematical questions, such as canard solutions and dynamic bifurcations.

List of Figures

List of Tables

Bibliography

[1] F. Clément et J.-P. Françoise, “Mathematical modeling of the GnRH pulse and surge generator,” SIAM J. Appl. Dyn. Syst. **6**, 441–456 (2007). 1.1, 2.1, 2.2, 2.4, 3.1

[2] R. Bertram, J. Previte, A. Sherman, T. A. Kinard, et L. S. Satin, “The phantom burster model the phantom burster model for pancreatic β-cells,” Biophys. J. **79**, 2880–2892 (2000). 1.1

[3] F. Clément et A. Vidal, “Foliation-based parameter tuning in a model of GnRH pulse and surge generator,” SIAM J. Appl. Dyn. Syst. **8**, 1591–1631 (2009). 1.1, 2.2, 2.2, 2.2.2, 2.2.3, 3.1, 3.2.1, 3.2.1, 3.5, 3.5, 3.7

[4] A. Vidal et F. Clément, “A dynamical model for the control of the gonadotrophin releasing hormone neurosecretory system,” J. Neuroendocrinol. **22**, 1251–1266 (2010). 1.1, 2.2, 3.1, 3.5

[5] M. Krupa, A. Vidal, M. Desroches, et F. Clément, “Mixed-mode oscillations in a multiple time scale phantom bursting system,” SIAM J. Appl. Dyn. Syst. **11**, 1458–1498 (2012). 1.1, 1.2.2, 2.1, 2.2, 2.2.1, 2.2.1, 2.2.2, 2.2.2, 2.2.3, 2.2, 2.2.3, 2.3.1, 3.1, 5

[6] E. Benoît, J.-L. Callot, F. Diener, et M. Diener, “Chasse au canard,” Collect. Math. **32**, 37–119 (1981). 1.2, 2.1, 2.2.2

[7] M. Krupa et P. Szmolyan, “Relaxation oscillation and canard explosion,” J. Differ. Equ. **174**, 312–368 (2001). 1.2

[8] M. Brøns, “Bifurcations and instabilities in the greitzer model for compressor system surge,” Math. Eng. Ind. **2**, 51–63 (1988). 1.2

[9] M. Diener, “The canard unchained or how fast/slow dynamical systems bifurcate,” The Mathemaical Intelligencer **6**, 38–48 (1984). 1.2

[10] W. Eckhaus, “Relaxation oscillations including a standard chase on french ducks,” Lecture Notes in Math. **985**, 449–494 (1983). 1.2

[11] F. Dumortier et R. Roussarie, “Canard cycles and center manifolds,” Mem. Amer. Math. Soc. **577** (1996). 1.2

[12] M. Krupa et P. Szmolyan, “Extending geometric singular perturbation theory to nonhyperbolic points — fold and canard points in two dimensions„” SIAM J. Math. Anal. **33**, 286–314 (2001). 1.2

[13] M. Krupa et M. Wechselberger, “Local analysis near a folded saddle-node singularity,” J. Differ. Equ. **248**, 2841–2888 (2010). 1.2

[14] J. Guckenheimer, K. Hoffman, et W. Weckesser, “Numerical computation of canards,” Int. J. Bifur and Chaos **10**, 2669–2687 (2000). 1.2, 1.2.3, 2.1

[15] M. Desroches, J. Guckenheimer, B. Krauskopf, C. Kuehn, H. M. Osinga, et M. Wechselberger, “Mixed-mode oscillations in a multiple time scale,” SIAM Rev. **54**, 211–288 (2012). 1.2, 1.2.2, 1.2.3, 2.1, 2.3.1, 4.4.2

[16] M. Desroches, T. J. Kaper, et M. Krupa, “Mixed-mode bursting oscillations: Dynamics created by a slow passage through spike-adding canard explosion in a square-wave burster,” Chaos **23**, 046106 (2013). 1.2, 4.5

[17] T. Vo, R. Bertram, et M. Wechselberger, “Multiple geometric viewpoints of mixed mode dynamics associated with pseudo-plateau bursting,” SIAM J. Appl. Dyn. Syst. **12**, 789–830 (2013). 1.2

[18] M. A. Kramer, R. D. Traub, et N. Kopell, “New dynamics in cerebellar purkinje cells: torus canards,” Phys. Rev. Lett. **101** (2008). 1.2

[19] M. Krupa, N. Popovic, N. Kopell, et H. G. Rotstein, “Mixed-mode oscillations in a three time-scale model for the dopaminergic neuron,” Chaos **18**, 015106 (2008). 1.2, 2.1

[20] J. Mitry, M. McCarthy, N. Kopell, et M. Wechselberger, “Exitable neurons, firing threshold manifolds and canards,” J. Math. Neurosci. **3** (2013). 1.2, 1.2.2

[21] H. G. Rotstein, T. Oppermann, J. A. White, et N. Kopell, “The dynamic structure underlying subthreshold oscillatory activity and the onset of spikes in a model of medial entorhinal cortex stellate cells,” J. Comput. Neurosci. **21**, 271–292 (2006). 1.2, 2.1

[22] J. Rubin et M. Wechselberger, “Giant squid-hidden canard: the 3D geometry of the Hodgkin-Huxley model,” Biol. Cybern. **97**, 5–32 (2007). 1.2, 2.1

[23] J. Moehlis, “Canards for a reduction of Hodgkin-Huxley equations,” J. Math. Biol. **52**, 141–153 (2006). 1.2, 4.2.1, b, b, 4.5

[24] M. Desroches, B. Krauskopf, et H. M. Osinga, “The geometry of mixed-mode oscillations in the Olsen model for the perioxidase-oxidase reaction,” Discr. Cont. Dyn. Sys. S **2**, 807–827 (2009). 1.2

[25] A. Milik, A. Szmolyan, H. Loeffelmann, et E. Groeller, “Geometry of mixed-mode oscillations in the 3-d autocatalator,” Int. J. Bifur and Chaos **8**, 505–519 (1998). 1.2

[26] B. Peng, V. Gaspar, et K. Showalter, “False bifurcations in chemical systems: canards,” Philos. Trans. R. Soc. Lond. A **337** (1991). 1.2

[27] H. G. Rotstein, N. Kopell, A. M. Zhabotinsky, et I. R. Epstein, “A canard mechanism for localization in systems of globally coupled oscillators,” SIAM J. Appl. Math. **63**, 1998–2019 (2003). 1.2, 1.3, 4.1

[28] E. Harvey, V. Kirk, J. Sneyd, et M. Wechselberger, “Understanding anomalous delays in a model of intracellular calcium dynamics,” Chaos **20**, 0451104 (2010). 1.2

[29] N. Fenichel, “Asymptotic stability with rate conditions II,” Indiana Univ. Math. J. **26**, 81–93 (1977). 1.2

[30] C. Lobry, Dynamic bifurcations (Springer, New York, 1991), vol. 1493 de Lecture Notes in Math., chap. Dynamic bifurcations, p. 1–13. 1.2

[31] M. Desroches, M. Krupa, et S. Rodrigues, “Inflection, canards and excitability threshold in neuronal models,” J. Math. Biol. **67**, 989–1017 (2013). 1.2.2, 2.2.2

[32] E. Koksal Ersoz, M. Desroches, M. Krupa, et F. Clément, “Canard-mediated (de)synchronization in coupled phantom bursters,” SIAM J. Appl. Dyn. Syst. **15**, 580–608 (2016). 1.2.2, 2

[33] B. Ermentrout et D. Terman, Mathematical Foundations of Neuroscience (Springer, 2010). 1.3, 1.3.1, 2.1, 2.3, 3.1, 4.1

[34] E. M. Izhikevich, “Synchronization of elliptic bursters,” SIAM Rev. **43**, 315–344 (2001). 1.3, 2.1, 2.3, 3.1

[35] M. Dhamala, V. K. Jirsa, et M. Ding, “Transitions to synchrony in coupled bursting neurons,” Phys. Rev. Lett. **92**, 028101 (2004). 1.3, 3.1

[36] A. Sherman, “Anti-phase, asymmetric and aperiodic oscillations in excitable cells–I. coupled bursters,” Bull. Math. Biol. **56**, 811–835 (1994). 1.3, 3.1

[37] G. de Vries, A. Sherman, et H.-R. Zhu, “Diffusively coupled bursters: effects of cell heterogeneity,” Bull. Math. Biol. **60**, 1167–1200 (1998). 1.3, 3.1

[38] I. Belykh, E. de Lange, et M. Hasler, “Synchronization of bursting neurons: What matters in the network topology,” Phys. Rev. Lett. **94**, 188101 (2005). 1.3, 3.1

[39] J. Drover, J. Rubin, J. Su, et B. Ermentrout, “Analysis of a canard mechanism by which excitatory synaptic coupling can synchronize neurons at low firing frequencies,” SIAM J. Appl. Dyn. Syst. **65**, 69–92 (2004). 1.3, 4.1

[40] B. Ermentrout et M. Wechselberger, “Canards, clusters and synchronization in a weakly coupled interneuron model,” SIAM J. Appl. Dyn. Syst. **8**, 253–278 (2009). 1.3, 2.1, 4.1

[41] K.-L. Roberts, J. Rubin, et M. Welchselberger, "Averaging, folded singularities, and torus canards: Explaining transitions between bursting and spiking in a coupled neuron model," SIAM J. Appl. Dyn. Syst. **14**, 1808–1844 (2015). 1.3, 4.1

[42] H. G. Rotstein et R. Kuske, "Localized and asynchronous patterns via canards in coupled calcium oscillators," Physica D **215**, 46–61 (2006). 1.3, 4.1

[43] D. Somers et N. Kopell, "Rapid synchronization through fast threshold modulation," Biol. Cybern. **68**, 393–407 (1993). 1.3, 2.1, 2.3, 3.1, 3.5, 4.3

[44] D. Terman et E. Lee, "Partial synchronization in a network of neural oscillators," SIAM J. Appl. Math. **57**, 252–293 (1997). 1.3, 3.1

[45] D. Terman, N. Kopell, et A. Bose, "Dynamics of two mutually coupled slow inhibitory neurons," Physica D **117**, 241–275 (1998). 1.3, 3.1

[46] D. Terman, E. Lee, J. Rinzel, et T. Bem, "Stability of anti-phase and in-phase locking by electrical coupling but not fast inhibition alone," SIAM J. Appl. Dyn. Syst. **10**, 1127–1153 (2011). 1.3, 3.1, 4.1, 4.3

[47] E. Lee et D. Terman, "Stable antiphase oscillations in a network of electrically coupled neurons," SIAM J. Appl. Dyn. Syst. **12**, 1–27 (2013). 1.3, 3.1, 4.3

[48] F. Hoppenteadt et E. Izhikevich, Weakly Connected Neuroal Networks (Springer, 1997). 1.3, 1.3.1, 1.3.2, 2.3.3, 3.1, 3.6.1, 4.1

[49] N. W. Schulthesis, A. A. Prinz, et R. J. Butera, eds., Phase Response Curves in Neuroscience: Theory, Experiment, and Analysis, vol. 6 de Springer series in computational neuroscience (Springer, New York, 2012). 1.3, 1.3.1, 1.3.2, 2.3.3, 3.1, 3.6.1, 3.6.1, 4.1

[50] D. Hansel, G. Mato, et C. Meunier, "Synchrony in excitatory neural networks," Neural Comp. **7**, 307–337 (1995). 1.3, 2.3, 2.3.3, 3.1, 4.1

[51] B. Ermentrout, "Type I membranes, phase resetting curves and synchrony," Neural Comp. **8**, 979–1001 (1996). 1.3, 2.3.3, 3.1, 4.1

[52] T. Lewis et J. Rinzel, "Dynamics of spiking neurons connected by both inhibitory and electrical coupling," J. Comput. Neurosci. **14**, 283–309 (2003). 1.3, 2.3.3, 3.1, 4.1, 4.4

[53] B. Pfeuty, G. Mato, D. Golomb, et D. Hansel, "Electrical synapses and synchrony: The role of intrinsic currents," J. Neurosci. **23**, 6280–6294 (2003). 1.3, 3.1

[54] E. Brown, J. Moehlis, et P. Holmes, "On the phase reduction and response dynamics od neural oscillator populations," Neural Comp. **16**, 673–715 (2003). 1.3, 3.1, 4.1

[55] B. Ermentrout, M. Pascal, et B. Gutkin, “The effects of prikie frequency adaptation and negative feedback on the synchronization of neural oscillators,” Neural Comp. **13**, 1285–1310 (2001). 1.3, 3.1, 4.1

[56] J. Mancilla, T. Lewis, D. Pinto, J. Rubin, et C. B.W., “Synchronization of electrically coupled pairs of inhibitory interneurons in neocortex,” J. Neurosci. **27**, 2058–2073 (2007). 1.3, 3.1, 3.6.1, 4.1

[57] S. K. Maran et C. C. Canavier, “Using phase resetting to predict 1:1 and 2:2 locking in two neuron networks in which firing order in not always preserved,” J. Comput. Neurosci. **24**, 37–55 (2008). 1.3, 3.1, 3.6.1, 4.4

[58] I. Malkin, Methods of Poincare and Liapunov in Theory of Non-Linear Oscillations (Gostexizdat, 1949). 1.3, 1.3.2, 2.3.3, 4.1

[59] I. G. Malkin, Some Problems in Nonlinear Oscillation Theory (Gostexizdat, 1956). 1.3, 1.3.2, 2.3.3, 4.1

[60] E. M. Izhikevich, “Phase equations for relaxation oscilators,” SIAM J. Appl. Math. **60**, 1789–1805 (2000). 1.3, 2.1, 2.3.3, 3.1, 4.1, 4.3, 4.6

[61] M. Oh et V. Matveev, “Loss of phase-locking in non-weakly coupled inhibitory networks of type-I model neurons,” J. Comput. Neurosci. **26**, 303–320 (2009). 1.3, 3.1, 3.6.1, 4.4

[62] E. M. Izhikevich et F. C. Hoppensteadt, “Slowly coupled oscillators: phase dynamics and synchronization,” SIAM J. Appl. Math. **63**, 1935–1953 (2003). 1.3, 3.1

[63] W. Kurebayashi, S. Shirasaka, et H. Nakao, “A criterion for timescale decomposition of external inputs for generalized phase reduction of limit-cycle oscillators,” Nonliear Teory and Its Aplications, IEICE **6**, 171–180 (2015). 1.3, 3.1, 3.7

[64] Y. Park et B. Ermentrout, “Weakly coupeld oscillators in a slowly varying world,” J. Comput. Neurosci. **40**, 269–281 (2016). 1.3, 3.1, 3.7

[65] B. Ermentrout et N. Kopell, “Frequency plateaus in a chain of weakly coupled oscillators,” SIMA **15**, 215–237 (1984). 1.3.1, 2.3.3, 4.1

[66] Y. Kuramoto, Chemical oscillators, waves, and turbulence (Springer-Verlag, 1984). 1.3.1, 1.3.2

[67] B. Ermentrout, Simulating, analyzing, and animating dynamical systems: a guide to XPPAUT for researchers and students (SIAM, 2002). 1.3.1

[68] J. Keener et J. Sneyd, Mathematical Physiology (Springer, 1998). 2.1

[69] P. Nan, Y. Wang, V. Kirk, et J. E. Rubin, “Understanding and distinguishing three-time-scale oscillations: Case study in a coupled Morris-Lecar system,” SIAM J. Appl. Dyn. Syst. **14**, 1518–1557 (2015). 2.1

[70] P. Szmolyan et M. Wechselberger, “Canards in $\mathbb{R}^3$,” J. Differ. Equ. **177**, 419–453 (2001). 2.2.2, 2.3.1

[71] N. Kopell et D. Somers, “Anti-phase solutions in relaxation oscillators coupled through excitatory interactions,” J. Math. Biol. **33**, 261–280 (1995). 2.3, 4.1, 4.3

[72] C. van Vreeswijk, L. Abbot, et B. Ermentrout, “When inhibition not excitation synchronizes neural firing,” J. Comput. Neurosci. **1**, 313–321 (1994). 2.3, 2.3.3, 3.1, 4.1, 4.3

[73] E. Benoît, “Canards et enlacements,” Inst. Hautes Études Sci. Publ. Math. **72**, 63–91 (1990). 2.3.1

[74] M. Wechselberger, “Existence and bifurcation of canards in $\mathbb{R}^3$ in the case of a folded node,” SIAM J. Appl. Dyn. Syst. **4**, 101–139 (2005). 2.3.1

[75] A. Pikovsly, M. Rosenblum, et J. Kurths, Synchronization: A universal concept in nonlinear sciences (Cambridge University Press, 2001). a

[76] B. Ermentrout et N. Kopell, “Multiple pulse interactions and averaging on coupled neural oscillators,” J. Math. Biol. **29**, 195–217 (1991). 2.3.3, 4.1

[77] D. Hansel, G. Mato, et C. Meunier, “Phase dynamics for weakly coupled Hodgkin-Huxley neurons,” Europhys. Lett. **25**, 367–372 (1993). 2.3.3, 4.1

[78] W. Duan, K. Lee, A. E. Herbison, et J. Sneyd, “A mathematical model of adult GnRH neurons in mouse brain and its bifurcation analysis,” J. Theor. Biol. **276**, 22–34 (2011). 2.4

[79] M. Krupa, A. Vidal, et F. Clément, “A network model of the periodic synchronization process in the dynamics of calcium concentration in GnRH neurons,” J. Math. Neurosci. **3:4** (2013). 2.4, 3.7

[80] N. P. Evans, G. E. Dahl, D. Mauger, V. Padmanabhan, L. A. Thrun, et F. J. Karsch, “Does estradiol induce the preovulatory gonadotropin-releasing hormone (GnRH) surge in the ewe by inducing a progressive change in the mode of operation of the GnRH neurosecretory system?” Endocrinology **136**, 5511–5519 (1995). 2.4, 3.1

[81] A. C. Christian et S. M. Moenter, “The neurobiology of preovulatory and estradiol-induced gonadotropin-releasing hormone surges,” Endocr. Rev. **31**, 544–577 (2010). 2.4

[82] S. Moenter, A. Caraty, et F. Karsch, “The estradiol-induced surge of gonadotropin-releasing hormone in the ewe,” Endocrinology **127**, 1375–1384 (1990). 3.1, 3.5, 3.13, 5

[83] S. Moenter, A. Caraty, A. Locatelli, et F. Karsch, “Pattern of gonadotropin-releasing hormone (GnRH) secretion leading up to ovulation in the ewe: existence of a preovulatory GnRH surge,” Endocrinology **129**, 1175–1182 (1991). 3.1, 3.5, 3.14, 5

[84] J. Z. Kasa-Vubu, G. E. Dahl, E. N. P., T. L. A., et K. F. J., "Progesterone blocks the estradiol-induced gonadotropin discharge in the ewe by inhibiting the surge og gonadotropin-releasing hormone," Endocrinology **131**, 208–212 (1992). 3.1, 3.5

[85] N. P. Evans, G. E. Dahl, V. Padmanabban, L. A. Thrun, et F. J. Karsh, "Estradiol requirements for induction and maintenance of the gonadotropin-releasing hormone surge: implications of neuroendocrine processing of the estradiol signal," Endocrinology **138**, 5408–5414 (1997). 3.1, 3.5

[86] A. Caraty, C. Fabre-Nys, B. Delaleu, A. Locatelli, G. Bruneau, F. Karsch, et A. Herbison, "Evidence that the mediobasal hypothalamus is the primary site of action of estradiol in inducing the preovulatory gonadotropin releasing hormone surge in the ewe," Endocrinology **139**, 1752–1760 (1998). 3.1, 3.5

[87] M. Nishihara, Y. Takeuchi, T. Tanaka, et Y. Mori, "Electrophysiological correlates of pulsatile and surge gonadotrophin secretion," Rev. Reprod. **4**, 110–116 (1999). 3.1

[88] N. Evans, G. Dahl, A. Caraty, V. Padmanabhan, L. Thrun, et F. Karsch, "How much of the gonadotropin-releasing hormone (GnRH) surge is required for generation of the luteinizing hormone surge in the ewe? duration of the endogenous GnRH signal," Endocrinology **137**, 4730–4737 (1996). 3.1

[89] A. Caraty et D. Skinner, "Progesterone priming is essential for the full expression of the positive feedback effect of estradiol in inducing the preovulatory gonadotropin-releasing hormone surge in the ewe," Endocrinology **140**, 165–170 (1999). 3.1

[90] A. Caraty, B. Delaleu, D. Chesneau, et C. Fabre-Nys, "Sequential role of E2 and gnrh for the expression of estrous behavior in ewe," Endocrinology **143**, 139–145 (2002). 3.1

[91] S. Ben Saïd, D. Lomet, D. Chesneau, L. Lardic, S. Canepa, D. Guillaume, C. Briant, C. Fabre-Nys, et A. Caraty, "Differential estradiol requirement for the induction of estrus behavior and the luteinizing hormone surge in two breeds of sheep," Biol. Reprod. **76**, 673–680 (2007). 3.1

[92] P. Bradley, K. Wiesenfeld, et R. J. Butera, "Effects of heterogeneity in synaptic conductance between weakly coupled identical neurons," J. Comput. Neurosci. **30**, 455–469 (2011). 3.1

[93] Y.-X. Li, Y. Wang, et R. Miura, "Clustering in small networks of excitatory neurons with heterogeous coupling strengths," J. Comput. Neurosci. **14**, 139–159 (2003). 3.1

[94] A. Bose, N. Kopell, et D. Terman, "Almost-synchronous solutions for mutually coupled excitatory neurons," Physica D **140**, 69–94 (2000). 3.5

[95] E. Lee et D. Terman, “Stability of antiphase oscillations in a network of inhibitory neurons,” SIAM J. Appl. Dyn. Syst. **14**, 448–480 (2015). 3.5

[96] M. Feingold, D. L. Gonzalez, O. Piro, et H. Vitturo, “Phase locking, period doubling, and chaotic pehomena in externally driven excitable systems,” Phys. Rev. A **37** (1988). 3.6.1, 4.1, 4.5

[97] I. B. Schwartz et T. Erneux, “Subharmonic hysteresis and period doubling bifurcations for a periodically driven laser,” SIAM J. Appl. Math. **54**, 1083–1100 (1994). 3.6.1, 4.5

[98] A. Buică, J.-P. Françoise, et J. Llibre, “Periodic solutions of nonlinear periodic differential systems with a small parameter,” Commun. Pure Appl. Math. **6** (2007). 4.1

[99] M. Roseau, Vibrations nonlinéaires et théorie de la stabilité (Springer-Verlag, Berlin, 1966). 4.1

[100] J.-P. Françoise, Oscillations en biologie: Analyse qualitative et modèles (Springer-Verlag, 2005). 4.1

[101] S. M. Crook, B. Ermentrout, et J. M. Bower, “Spike frequency affects the synchronization properties of networks of cortical oscillators,” Neural Comp. **10**, 1643–1678 (1998). 4.1

[102] C. C. Chow et N. Kopell, “Dynamics of spiking neurons with electrical coupling,” Neural Comp. **12**, 1643–1678 (2000). 4.1

[103] A. Urban et B. Ermentrout, “Formation of antiwaves in gap-junction-coupled chains of neurons,” Physical Review E **86**, 011907 (2012). 4.1

[104] D. G. Aronson, B. Ermentrout, et N. Kopell, “Amplitude response of coupled oscillators,” Physica D **41**, 403–449 (1990). 4.1

[105] B. Ermentrout et N. Kopell, “Mechanisms of phase-locking and frequency control in pairs of coupled neural oscillators,” dans “Handbook of Dynamical Systems II: Towards Applications,” , B. Fiedler, ed. (Elsevier, 2002), p. 5–54. 4.1

[106] I. Z. Kiss, Y. Zhai, et J. L. Hudson, “Predicting mutual entrainment of oscillators with experiement-based phase models,” Phys. Rev. Lett. **94**, 248301 (2005). 4.1

[107] M. Wickramasinghe et I. Z. Kiss, “Spatially organized dynamical states in chemical oscillator networks: Synchronization , dynamical differentiation, and chimera patterns,” PLoS ONE **8**, e80586 (2013). 4.1

[108] J. Belair et P. Holmes, “On linearly coupled relaxation oscillators,” Quart. Appl. Math. **42**, 193–219 (1984). 4.1

[109] T. Bem et J. Rinzel, “Short duty cycle destabilizes a half-center oscillator, but gap junctions can restabilize the anti-phase pattern,” J. Neurophysiol **91**, 693–703 (2004). 4.1

[110] T. Chakraboty et R. Rand, “The transitions from phase locking to drift in a system of two weakly coupled van der pol oscillators,” Int. J. Nonlinear Mechanics **23**, 369–376 (1988). 4.1

[111] G. Cymbalyuk, E. Nikolaev, et R. Borisyuk, “In-phase and antiphase self-oscillations in a model of two electrically coupled pacemakers,” Biol. Cybern. **71**, 153–160 (1994). 4.1, 4.3

[112] A. Sherman et J. Rinzel, “Rhythmogenic effects of weak electronic coupling in neuronal models,” Proc. Natl. Acad. Sci. USA **89**, 2471–2474 (1992). 4.1

[113] B. Pfeuty, G. Mato, D. Golomb, et D. Hansel, “The combined effects of inhibitory and electrical synapses in synchrony,” Neural Comp. **17**, 633–670 (2005). 4.1

[114] R. Curtu, A. Shpiro, N. Rubin, et J. Rinzel, “Mechanisms for frequency control in neural competition models,” SIAM J. Appl. Dyn. Syst. **7**, 609–649 (2008). 4.1

[115] C. Zhang et T. Lewis, “Phase response properties of half-center oscillators,” J. Comput. Neurosci. **35**, 55–74 (2013). 4.1, 4.2.2

[116] T. Netoff, C. Acker, J. Bettencourt, et J. A. White, “Beyond two-cell networks: experimental measurement of neuronal responses to multiple synaptic inputs,” J. Comput. Neurosci. **18**, 287–295 (2005). 4.1

[117] E. J. Doedel, A. R. Champneys, F. Dercole, T. Fairgrieve, Y. Kuznetsov, B. E. Oldeman, R. Paffenroth, B. Sandstede, et X. J. Wang, “AUTO-07P : Continuation and bifurcation software for ordinary differential equations,” (2007). Available at `http://cmvl.cs.concordia.ca/auto`. 4.2

[118] B. Ermentrout, B. Beverlin II, et T. Netoff, “Phase response curves to measure ion channel effects on neurons,” dans “Phase response curves in neuroscience,” , N. W. Schultheiss, A. A. Prinz, et R. J. Butera, eds. (Springer, 2012), p. 207–236. 4.2

[119] P. De Maesschalck et M. Desroches, “Numerical continuation techniques for planar slow-fast systems,” SIAM J. Appl. Dyn. Syst. **12**, 1159–1180 (2013). 4.2.2

[120] A. T. Winfree, The geometry of biological time, vol. 12 de Interdisciplinary Applied Mathematics (Springer, 1980). 4.5

[121] P. Langfield, B. Krauskopf, et H. M. Osinga, “Solving Winfree’s puzzle: The isochrons in the FitzHugh-Nagumo model,” Chaos **24**, 013131 (2014). 4.5

[122] G. Ermentrout, “Period doublings and possible chaos in neural models,” SIAM J. Appl. Math. **44**, 80–95 (1984). 4.5

[123] J. Durham et J. Moehlis, “Feedback control of canards,” Chaos **18**, 015110 (2008). 4.5

[124] M. Krupa, B. Ambrosio, et M. A. Aziz-Alaoui, “Weakly coupled two-slow–two-fast systems, folded singularities and mixed mode oscillations,” Nonlinearity **27**, 1555–1574 (2014). 4.5

[125] G. de Vries et A. Sherman, “Beyond synchronization: Modulatory and emergent effects of coupling in square-wave bursting,” dans “Bursting: The genesis of rhythm in the nervous system,” , S. Coombes et P. C. Bressloff, eds. (World Scientific, 2005), p. 243–272. 4.5

[126] E. A. Coddington et N. Levinson, Theory of ordinary differential equations (McGraw-Hill, 1987). 4.6

[127] S. Schecter, “Adjoint equation and Melnikov function,” Unpublished note. 4.6, 4.6

Sujet : Étude mathématique de systèmes multi-échelles en temps couplés, synchronisation de populations de neurones endocrines

Résumé : Dans cette thèse, nous étudions les propriétés de synchronisation d'oscillateurs lents-rapides inspirés de la neuroendocrinologie et des neurosciences, en se concentrant sur les effets des phénomènes de type canard et bifurcations dynamiques sur le comportement collectif.

Nous partons d'un système de dimension 4 qui représente les caractéristiques dynamiques qualitatives et quantitatives du profil de sécrétion de la neurohormone GnRH (gonadotropin releasing hormone) au cours d'un cycle ovarien. Ce modèle est constitué de deux oscillateurs de FitzHugh-Nagumo avec pour chacun des échelles de temps différentes. Le couplage unidirectionnel de l'oscillateur lent (représentant l'activité moyenne d'une population de neurones régulateurs) vers l'oscillateur rapide (représentant l'activité moyenne d'une population de neurones sécréteurs) donne une structure à trois échelles de temps. Le comportement de l'oscillateur rapide est characterisé par une alternance entre un régime de type cycle de relaxation et un régime de quasi-stationnaire qui induit des transitions de type canard dans le modèle ; ces transitions ont un fort impact sur le modèle de sécrétion du système de dimension 4. Nous proposons un premier pas supplémentaire dans la modélisation multi-échelles (en espace) du système GnRH, c'est-à-dire que nous étendons le système original à 6 dimensions en considérant deux sous-populations distinctes de neurones sécréteurs recevant le même signal des neurones de régulation. Cette étape nous permet de enrichir les motifs possibles de sécrétion de GnRH tout en gardant un cadre dynamique compact et en préservant la séquence des événements neuro-sécréteurs capturés par le modèle de dimension 4, à la fois qualitativement et quantitativement.

Une première analyse du modèle GnRH étendu à 6 dimensions est présentée dans le Chapitre 2, où nous montrons à l'aide d'un système minimal de dimension 5 l'existence de trajectoires de type canard dans des systèmes lents-rapides couplés présentant des points pseudo-stationnaires. Le couplage provoque la séparation des trajectoires correspondant à chaque sécréteur qui se retrouvent de chaque côté du canard maximal (associé soit à un point pseudo-stationnaire de type noeud soit à un pseudo-col). Nous explorons les rapports entre les canards en présence et le couplage, ainsi que leur impact sur les motifs de sécrétion collective du modèle de dimension 6. Nous identifions deux sources différentes de (dé)synchronisation due aux canards dans les événements sécrétoires, qui dépendent du type de point pseudo-stationnaire sous-jacent.

Dans le Chapitre 3, nous proposons une modélisation possible des comportements complexes de sécrétion de GnRH qui ne sont pas capturés par le modèle de dimension 4, à savoir, une décharge avec 2 "bosses" et une désynchronisation partielle avant la décharge, en utilisant le modèle de dimension 6 précédemment construit. Pour obtenir une décharge avec deux bosses, il est essentiel d'utiliser des fonctions de couplage asymétriques dépendant du régulateur ainsi que d'introduire de l'hétérogénéité dans les sous-populations de sécréteurs. Pendant le régime pulsatile, il apparaît que le signal régulateur varie lentement et, ce faisant, provoque une bifurcation dynamique qui est responsable de la perte de synchronie dans le cas de sécréteurs non identiques et asymétriquement couplés. Nous introduisons des outils analytiques et numériques pour façonner et quantifier ces caractéristiques supplémentaires et les intégrer dans le profil complet de sécrétion.

Afin d'obtenir une meilleure compréhension du rôle des canards dans les phénomènes de (dé)synchronisation, nous proposons, au Chapitre 4, une extension de la théorie de oscillateurs (du plan) faiblement couplés au cas des cycles de canard. À l'aide de techniques de continuation numérique, nous calculons des solutions aux problèmes adjoints associés à des oscillateurs singulièrement perturbés. Nous identifions le rôle pivot que joue le canard maximal dans la transition entre les différents modes de synchronisation. Nous trouvons des solutions synchrones $2nT$-périodiques pour des systèmes identiques couplés à proximité du canard maximal et nous étudions l'impact de la force de couplage et du principal paramètre qui organise l'explosion de canards (pour chaque oscillateur seul) sur l'existence de telles familles de solutions synchrones.

Les bifurcations dynamiques et transitions lentes-rapides étudiées dans cette thèse se retrouvent plus généralement en neuroscience, dans les systèmes produisant des dynamiques de type “spiking” et/ou “bursting”. Un certain nombre de pistes concernant l'extension de notre travail à ces dynamiques sont mises en évidence dans le chapitre de conclusion.

Mots clés : canards, synchronisation, systèmes lents-rapides, systèmes multi-échelles de temps, points pseudo-stationnaires, sécrétion de GnRH, oscillateurs faiblement couplés, bifurcations dynamiques

Subject : A mathematical study on coupled multiple timescale systems, synchronization of populations of endocrine neurons

Abstract: This dissertation investigates synchronization properties of slow-fast oscillators inspired from neuroendocrinology and neuronal dynamics, focusing on the effects of canard phenomena and dynamic bifurcations on the collective behavior.

We start from a 4-dimensional system which accounts for the qualitative and quantitative dynamical features of the secretion pattern of the neurohormone GnRH (gonadotropin releasing hormone) along a whole ovarian cycle. This model involves 2 FitzHugh-Nagumo oscillators with different timescales. Unidirectional coupling from the slow oscillator (representing the mean-field activity of a population of regulating neurons) to the fast oscillator (representing the mean-field activity of a population of the secreting neurons) gives a three timescale structure. The behavior of the fast oscillator is characterized by an alternation between a relaxation cycle and a quasi-stationary state which introduces canard-mediated transitions in the model; these transitions have a strong impact on the secretion pattern of the 4-dimensional system. We make a first step forward in multiscale modeling (in space) of the GnRH system, namely, we extend the original system to 6 dimensions by considering two distinct subpopulations of secreting neurons receiving the same signal from the regulating neurons. This step allows us to enrich further the GnRH secretion pattern while keeping a compact dynamic framework and preserving the sequence of neurosecretory events captured by the 4-dimensional model, both qualitatively and quantitatively.

An initial analysis of the extended 6-dimensional GnRH model is presented in Chapter 2, where we prove using a 5D minimal model the existence of canard trajectories in coupled systems with folded singularities. Coupling causes separation of trajectories corresponding to each secretor by driving them to different sides of the maximal canard (associated with either a folded-node or a folded-saddle singularity). We explore the impact of the relationship between canard structures and coupling on the collective secretion pattern of the 6-dimensional model. We identify two different sources of canard-mediated (de)synchronization in the secretory events, which depend on the type of underlying folded singularity.

In Chapter 3, we attempt to model complex behaviors of the GnRH secretion not captured by the 4-dimensional model, namely, a surge with 2 bumps and partial desynchronization before the surge, by using the 6-dimensional model previously constructed. Regulatory-dependent asymmetric coupling functions and heterogeneity in the secretor subpopulations are essential for obtaining such a 2-bump surge. During the pulsatile regime, we find that the slowly varying regulatory signal causes a dynamic bifurcation, which is responsible for loss of synchrony in asymmetrically coupled nonidentical secretors. We introduce analytic and numerical tools to shape and quantify the additional features embedded within the whole secretion pattern.

In order to get further understanding on the role of canards in (de)synchronization phenomena, in Chapter 4, we extend the theory of weakly coupled (planar) oscillators to the case of canard cycles. We find solutions of adjoint equations of singularly perturbed oscillators by using numerical continuation techniques. We identify the role of the maximal canard as a pivotal in the transition between different modes of synchronization. We find $2nT$-periodic synchronous solutions arising in coupled identical cycles near the maximal canard depending on the coupling strength and on the main canard parameter.

The dynamic bifurcations and slow-fast transitions studied in this dissertation have applications to spiking/bursting systems in neuroscience, and ideas for the extension of our work to these dynamics are highlighted in the Conclusion chapter.

Keywords : canards, synchronization, slow-fast systems, multiple timescales, folded singularity, GnRH secretion, weakly coupled oscillators, dynamic bifurcation